"DETERMINATION OF LIPID DEPOSITIONS VIA THE REALIZATION OF NONLINEAR IMAGING MEASUREMENTS AND CORRELATION OF THE DATA WITH SPECIFIC BIOLOGICAL PROCESSES OF VARIOUS SAMPLES."

GAVGIOTAKI EVANGELIA

Master Thesis
Department of Physics
University of Crete
2014

SUPERVISOR: PROF. COSTAS FOTAKIS

ADVISOR: DR. GEORGE FILIPPIDIS

«ΠΡΟΣΔΙΟΡΙΣΜΟΣ ΛΙΠΙΔΙΚΩΝ ΕΝΑΠΟΘΕΣΕΩΝ ΚΑΙ ΣΥΣΧΕΤΙΣΗ ΤΟΥΣ ΜΕ ΤΗ ΛΕΙΤΟΥΡΓΙΑ ΒΙΟΛΟΓΙΚΩΝ ΔΕΙΓΜΑΤΩΝ ΜΕΣΩ ΚΑΤΑΓΡΑΦΗΣ ΜΗ ΓΡΑΜΜΙΚΩΝ ΑΠΕΙΚΟΝΙΣΤΙΚΩΝ ΜΕΤΡΗΣΕΩΝ»

ΓΑΥΓΙΩΤΑΚΗ ΕΥΑΓΓΕΛΙΑ

ΜΕΤΑΠΤΥΧΙΑΚΗ ΕΡΓΑΣΙΑ

ΤΜΗΜΑ ΦΥΣΙΚΗΣ

ΠΑΝΕΠΙΣΤΗΜΙΟ ΚΡΗΤΗΣ

2014

ΕΠΙΒΛΕΠΩΝ ΚΑΘΗΓΗΤΗΣ: ΚΑΘ. ΚΩΣΤΑΣ ΦΩΤΑΚΗΣ

ΥΠΕΥΘΥΝΟΣ ΕΡΓΑΣΙΑΣ: ΔΡ. ΓΙΩΡΓΟΣ ΦΙΛΙΠΠΙΔΗΣ

ΤΡΙΜΕΛΗΣ ΕΠΙΤΡΟΠΗΣ ΜΕΤΑΠΤΥΧΙΑΚΟΥ

Κ.Φωτακης καθηγητης στο τμημα φυσικης πανεπιστημιου κρητης

Ε. Αθανασακη καθηγητρια στο τμημα βιολογιας πανεπιστημιου κρητης

Π. Λουκακος ερευνητης στο ινστιτουτο ηλεκτρονικης δομης και λειζερ ,Ιτε

Table of contents

Ευχαριστίες

Η παρούσα μεταπτυχιακή μελέτη εκπονήθηκε από τη φοιτήτρια Ευαγγελία Γαυγιωτάκη του Τμήματα Φυσικής Πανεπιστημίου Κρήτης στο Ίδρυμα Τεχνολογίας και Έρευνας (ΙΤΕ - FORTH) με διευθύνοντα τον Καθ. Κωνσταντίνο Φωτάκη.

Θα ήθελα αρχικά να ευχαριστήσω τον Καθ. Κωνσταντίνο Φωτάκη ο οποίος μου παρείχε τη δυνατότητα να εργαστώ σε ένα άρτιο ερευνητικό περιβάλλον και είχε τη γενικότερη επίβλεψη της εργασίας.

Ευχαριστίες επίσης θα ήθελα να απευθύνω τον επιβλέποντα ερευνητή Δρ. Γιώργο Φιλιππίδη , ο οποίος ήταν ο τυπικά υπεύθυνος της πειραματικής διαδικασίας, για τη συνεχή καθοδήγηση, επίβλεψή και υποστήριξή του όλους αυτούς τους μήνες στο πειραματικό μέρος και την ανάλυση των αποτελεσμάτων, καθώς και για την ουσιαστική συνεισφορά στη διαμόρφωση του κειμένου.

Επιπλέον, θα ήθελα ιδιαίτερα να ευχαριστήσω την Καθ. Αθανασάκη Ειρήνη του Βιολογικού τμήματος του Πανεπιστημίου Κρήτης για την συνεργασία και για την βοήθεια που μου παρείχε για την εξέλιξη της μελέτης.

Ακόμα θα ήθελα να ευχαριστήσω την υποψήφια διδάκτορα Μαρία Καλογνόμου η οποία έπαιξε καθοριστικό ρόλο στην υλοποίηση της εργασίας μου. Επιμελήθηκε την προετοιμασία των βιολογικών δειγμάτων και ταυτόχρονα μου παρείχε πολύ φιλικά βοήθεια για την επεξήγηση εννοιών και προβλημάτων της βιολογίας .

Τέλος θα ήθελα να ευχαριστήσω την οικογένεια μου και τους φίλους μου για την υποστήριξη τους και την ενθάρρυνση τους κατά τη διάρκεια της εργασίας.

Acknowledgments

This Master Thesis commissioned by the graduate student Evangelia Gavgiotaki of the Department of Physics, at the University of Crete and at the Institute of Laser and Structure of Foundation for Research and Technology (IESL - FORTH) under the supervision of Prof. Costas Fotakis.

I would firstly like to thank Prof. Costas Fotakis, who gave me the opportunity to work in a proper research environment, and additionally he had the general supervision of this work.

Moreover, I would like to express my highest appreciation to my advisor Dr. George Filippidis for his guidance, encouragement and support, during the development of my Dissertation Thesis. His feedback and advices were more than valuable for me and were leading my efforts.

Furthermore, I would like especially to express my gratitude to Prof. Athanassakis Irene of the Biology Department at The University of Crete for the cooperation and the valuable assistance she offered me during the whole the progress of the Thesis.

What is more, I also would like to thank the PhD candidate Maria Kalognomou, which played a decisive role in the implementation of my study. She edited the preparation of the biological samples and simultaneously she offered me her help concerning the explanation of concepts and problems of the biology filed.

Last but not least, I would like to appreciate, my family and my friends for their excessive support and encouragement during the past two years.

Summary

Nonlinear optical processes have found widespread application in fields ranging from fundamental physics to biomedicine. Specifically, Third Harmonic Generation (THG) seems to be a suitable imaging tool for the delineation and quantification of biological structures at the microscopic level. In an isotropic medium, THG using focused femtosecond (fs) beams as excitation sources is possible only when an inhomogeneity is present in the focal volume. This property by itself already makes THG an ideal tool, since microscopic contrast is realized from the inherent properties of the sample and does not require additional labeling. In addition, the nonlinear nature of the interaction provides THG with inherent three dimensional imaging capabilities when using focused fs laser beams.

In this thesis, we attempted to understand the activation of cancer cells by using the THG imaging microscopy as a diagnostic tool and the BV-2 microglia cell line as a representative biological model.

Firstly, Third Harmonic Generation (THG) and Two Photon Excitation Fluorescence (TPEF) measurements were simultaneously collected from stained BV-2 cells, by employing a single homemade experimental apparatus, for the exact identification of the subcellular biological structures that gives high THG signals. Three different dyes in both cases of activation (control- activated cells) were used. It was shown that high THG signals arise mostly from lipid depositions.

Furthermore, in this study we used the THG microscopy to quantify the changes of mean total area and mean THG intensity values of lipid droplets before and after activation. THG imaging measurements provide a quantitative description of internal structures (lipid droplets), without staining. Activated BV-2 cells present higher lipid concentration and THG intensity values in comparison with the control cells.

Finally, we quantified the BV-2 cell line in different feed conditions Differences of mean total area and THG values of intensity of lipid droplets were investigated. Discrimination between control and activated BV-2 cells in three different feeding conditions was achieved.

The obtained results are very encouraging for the potential employment of THG imaging modality as a non-destructive diagnostic tool for cancer research.

Περίληψη

Οι μη γραμμικές διαδικασίες εμφανίζουν ευρύ φάσμα εφαρμογών τόσο στον τομέα της Φυσικής όσο και στο τομέα της Βιοιατρικής. Συγκεκριμένα , η γένεση Τρίτης Αρμονικής φαίνεται να είναι ένα κατάλληλο απεικονιστικό εργαλείο για την περιγραφή και ποσοτικοποίηση βιολογικών δομών σε μικροσκοπικό επίπεδο. Σε ένα ισοτροπικό μέσο , η γένεση της Τρίτης Αρμονικής από μια πηγή εκπομπής είναι πιθανή, όταν υπάρχουν ανομοιογένειες στο εστιακό όγκο. Η ιδιότητα αυτή θέτει τη Τρίτη Αρμονική ως ένα κατάλληλο εργαλείο, καθώς η μικροσκοπική αντίθεση πραγματοποιείται λόγω της εγγενής ιδιότητας του δείγματος και δεν χρειάζεται να υπάρξει κάποια επιπρόσθετη χρώση . Επιπλέον, η Τρίτη Αρμονική λόγω της μη γραμμικής φύσης της παρέχει απεικόνιση τριών διαστάσεων στην περίπτωση εστιασμένης δέσμης με fs λέιζερ.

Σε αυτή τη διπλωματική εργασία, η μέθοδος της γένεσης της Τρίτης Αρμονικής χρησιμοποιήθηκε ως διαγνωστικό εργαλείο για την κατανόηση της ενεργοποίησης των καρκινικών κυττάρων, στη μικρογλοιακή κυτταρική σειρά BV-2. Αρχικά έγιναν ταυτόχρονες μετρήσεις γένεσης της Τρίτης Αρμονικής και του Διφωτονικού Φθορισμού, χρησιμοποιώντας μόνο μια δέσμη, στη πρότυπη διάταξη που κατασκευάστηκε στο εργαστήριο, ώστε να γίνει ακριβής ταυτοποίηση των υποκυταρικών βιολογικών δομών που δίνουν σήμα Τρίτης Αρμονικής. Συγκεκριμένα, για την ταυτοποίηση αυτή χρησιμοποιήθηκαν τρεις διαφορετικές χρώσεις και στις δύο καταστάσεις των κυττάρων (ενεργοποιημένα – μη-ενεργοποιημένα). Τα αποτελέσματα έδειξαν ότι το σήμα της Τρίτης Αρμονικής προέρχεται κυρίως από τις λιπιδικές εναποθέσεις των βιολογικών δειγμάτων. Επίσης, στη μελέτη αυτή η γένεση της Τρίτης Αρμονικής χρησιμοποιήθηκε για να γίνει ποσοτικοποίηση στο μέσο εμβαδό και στη μέση τιμή έντασης της Τρίτης Αρμονικής αντίστοιχα, πριν και μετά την ενεργοποίηση των κυττάρων. Οι μετρήσεις απεικόνισης της Τρίτης Αρμονικής μας παρέχουν μια ποσοτική περιγραφή των δομών (λιπίδια), χωρίς καμία χρώση. Τα αποτελέσματα των μετρήσεων έδειξαν ότι τα ενεργοποιημένα BV-2 κύτταρα παρουσιάζουν μεγαλύτερη συγκέντρωση λιπιδίων και οι τιμές έντασης της Τρίτης Αρμονικής είναι μεγαλύτερες για τα ενεργοποιημένα κύτταρα σε σχέση με τα μη-ενεργοποιημένα.

Τέλος, πραγματοποιήθηκε ποσοτικοποίηση εμβαδού και έντασης της Τρίτης Αρμονικής υπό διαφορετικές συνθήκες τροφής για τη κυτταρική σειρά BV-2. Ειδικότερα, έγινε διάκριση μεταξύ ενεργοποιημένων και μη – ενεργοποιημένων κυττάρων για τις τρεις διαφορετικές καταστάσεις τροφής. Τα αποτελέσματα που προέκυψαν φαίνονται να είναι ενθαρρυντικά

και θέτουν την Τρίτη Αρμονική ως ένα κατάλληλο διαγνωστικό εργαλείο για την έρευνα κατά του καρκίνου.

Chapter 1. Introduction

Nonlinear optics is a field of study that is concerned with the interaction of electromagnetic radiation and matter, in which the matter responds in nonlinear manner to the incident radiation fields. This nonlinearity is typically observed at very high light intensities (values of the electric field comparable to interatomic electric fields, typically 10^8 V/m), such as those provided by pulsed lasers. Nonlinear optics was remained unexplored until the discovery of Second harmonic generation shortly after the demonstration of the first laser. (Peter Franken *et al.* at University of Michigan in 1961) [1].

Nonlinear optical phenomena are nonlinear in the sense that the behavior of light in nonlinear *media*, that is, media in which the dielectric polarization **P** responds nonlinearly to the electric field **E** of the light. For example, third harmonic generation (THG) is a coherent process, in which three photons incident on a nonlinear material are transformed into a single photon at three times the energy. This process can be resonantly enhanced, when the nonlinear material has energetic states near the first, second, or third harmonic of the incident light.

In order to describe more precisely the 'nonlinearity', we will define the electric field E and the polarization and the dependence between them. In case of linear optics, the induced polarization depends linearly on the electric field strength is described by the relationship:

$$P = \varepsilon_0 \chi^{(1)} E \quad (1.1)$$

where ε_0 is the vacuum permittivity and the constant $\chi^{(1)}$ is the first-order electric susceptibility characterizing the medium .

However, in nonlinear optics, the optical response can be described through the generalization of equation (1.1), by expressing the polarization as a power series in the field strength E(t) as it is presented in the following equation:

$$P = \varepsilon_0 (\chi^{(1)} E + \chi^{(2)} E^2 + \chi^{(3)} E^3 + \ldots) \quad (1.2)$$

where the quantities $\chi^{(2)}$, $\chi^{(3)}$ are known as the second and third-order nonlinear electric susceptibilities, respectively.

In the case of a harmonic light wave of the form:

$$E = E_0 \sin \omega t \quad (1.3)$$

the equation (1.2) can be written as:

$$P = \varepsilon_0[\chi^{(1)}E_0 \sin\omega t + \frac{\chi^{(2)}E_0^2}{2}(1-\cos 2\omega t) + \frac{\chi^{(3)}E_0^3}{4}(3\sin\omega t - \sin 3\omega t) + ...] \quad (1.4)$$

after using some trigonometric identities. As we can observe, equation (1.4) is described by an infinite sum of oscillating terms with angular frequencies that are integer multiples of ω. Specifically, the first term in equation (1.4) constitutes the linear response of the medium in the applied time-varying field. The second term is consisted of two components; the first component represents a constant quantity, which depends on the square of the field amplitude and the second component presents a dependence on the cos2ωt function, which shows that the angular frequency is double than the fundamental field frequency. The double frequency as well, represents the second harmonic irradiation, which is generated. Correspondingly, the third term of equation (1.4) shows that polarization contains a component, which oscillates at an angular frequency 3ω; hence, it is responsible for the re-radiation of the incident field energy as third harmonic generation light [2][3][4].

Third-harmonic generation (THG) is one of the basic nonlinear-optical processes, which have been intensely the early days of nonlinear optics. In THG microscopy, third harmonic light is generated at the focal point of a tightly focused ultra-short pulsed laser beam. Due to the coherent nature of the THG, no net signal is obtained when focussed inside a homogeneous, normally dispersive medium. This is because of the Gouy phase shift experienced by the excitation beam near the focus [5]. However, when the nonlinear medium is not uniform, either in the refractive index or in the nonlinear susceptibility, the THG signal does not vanish, and significant THG output can be obtained. This coherent nature of the THG process renders THG microscopy highly sensitive to in-homogeneities and the efficiency of signal generation strongly depends on the relative size of the in-homogeneity and the focal volume. This specificity makes THG microscopy useful as a tool for material characterization [6].

The body of this work is a report on some nonlinear optical microscopy investigations of BV2 cells. Specifically, we studied two-photon excitation fluorescence and third harmonic generation induced in this sample, by exposure to high intensity focused irradiation with ultrafast laser pulses at selected center wavelengths in the range of 1028 nm. These processes were performed in a developed homemade system that integrates nonlinear

imaging capabilities (THG, TPEF) in a single instrument, by using a single high peak power fs laser source.

The thesis is organized as follows. **Chapter 2** focuses on building a fundamental understating of wave propagation in a nonlinear medium and the phenomena that could result. Precisely, the nonlinear Maxwell equations are described and as well as the mechanisms of the nonlinear response of the material at the quantum level. In the end, the typical values of the linear and nonlinear susceptibilities that lead to harmonic generation procedure are investigated. Next, **Chapter 3** describes the theory of single and multiphoton excitation fluorescence. Specifically, a semi-classical description is presented in case of the atomic system is treated quantum mechanically, by using the Maxwell's equations. Continuously, a brief presentation of several quantities that characterize fluorescence is reviewed. Furthermore, **Chapter 4** analyses the applications of a number of optical techniques and includes a review on each technique. Confocal microscopy is firstly described, as it is a common technique in microscopy, as well as nonlinear techniques such as SFG, CARS, STED, HHG and MPEF are discussed. Moreover, **Chapter 5** describes the homemade experimental system of our lab that was used to perform the experiments of this thesis, which provides us the capability to collect simultaneously two nonlinear signals in a single beam. Continuously presents the biological sample that used for the experiments and its preparation in Prof. Athanassakis lab in Biology Department of UOC. **Chapter 6** presents the experimental results, by using simultaneously THG and TPEF imaging modalities in the biological sample, in order to identify the subcellular structures that give high THG signal. Next, **Chapter 7** shows and discusses the results of the quantification of the recorded THG signals, for the identification of the mean total area and mean THG values of BV-2 subcellular structures (lipid depositions). **Chapter 8** performs again the quantification of the recorded THG signals of BV-2 subcellular structures for mean THG values and means total area in case of different feed conditions and analyzes the experimental results. Finally, **Chapter 9** summarizes the work contained in this thesis and investigates future aspects where this research could be applied.

Chapter 2. The nonlinear optical susceptibility

2.1 Quantum Mechanical Description of the nonlinear Susceptibility

In order to derive explicit expressions for the nonlinear optical susceptibility, we used quantum mechanics laws. The quantum theory makes accurate predictions of the non-resonant response of atomic and molecular system. However, the quantum mechanical description of the nonlinear susceptibility is based on the density matrix formalism, which is too complicated method. For this reason, we used the properties of the atomic wavefunction for the calculation of nonlinear susceptibility.

Firstly, we assume that all of the properties of the atomic system can be described of the atomic wavefunction ψ(r,t), which is the solution of Schrödinger's equation:

$$i\hbar\frac{\partial\psi}{\partial t}=\hat{H}\psi \quad (2.1.1)$$

where $\hat{H}$ is the Hamiltonian operator:

$$\hat{H}=\hat{H}_0+\hat{V}(t) \quad (2.1.2)$$

which is the sum of the Hamiltonian operator $\hat{H}_0$ for a free atom and an interaction Hamiltonian operator $\hat{V}(t)$ that describes the interaction of the atom with the applied electromagnetic field.

The interaction Hamiltonian operator is used to be of the form:

$$\hat{V}(t)=-\hat{\mu}\cdot\vec{E}(t) \quad (2.1.3)$$

where $\hat{\mu}$ is the electric dipole moment operator and is given by the expression $\hat{\mu}=e\hat{r}$ where *–e* is the charge electron.

For the case in which no external field is applied to the atom, the Hamiltonian operator $\hat{H}$ equals to $\hat{H}_0$ and Schrödinger's equation possesses solutions in the form of energy eigenstates, known as stationary states, which has the form:

$$\psi_n(r,t)=u_n(\vec{r})e^{-i\omega_n t} \quad (2.1.4)$$

The term $u_n(\vec{r})$ is the spatially varying part of the wavefunction and the term $e^{-i\omega_n t}$ describes the time evolution of these states.

By substituting equation (2.1.4) into Schrödinger's equation, (2.1.1) comes of the time-independent Schrödinger's equation:

$$\hat{H}_0 u_n(\vec{r}) = E_n u_n(\vec{r}) \quad (2.1.5)$$

where $E_n = \hbar\omega_n$ .Here, n is a label variable, which is used in order to distinguish the various solutions. These solutions $u_n(\vec{r})$ are chosen to satisfy the orthonormal condition:

$$\int u_m^*(\vec{r}) u_n(\vec{r}) d^3r = \delta_{mn} \quad . (2.1.6)$$

When the atom is exposed to an electromagnetic field, Schrödinger's equation (2.1.1) is solved through the use of perturbation theory. Firstly, we substitute the Hamiltonian (2.1.2) by:

$$\hat{H} = \hat{H}_0 + \lambda\hat{V}(t) \quad (2.1.7)$$

where λ is a continuously varying parameter and characterizes the strength of the interaction.

The solution of Schrödinger's equation in the form of power series in λ is:

$$\psi(\vec{r},t) = \psi^{(0)}(\vec{r},t) + \lambda\psi^{(1)}(\vec{r},t) + \lambda^2\psi^{(2)}(\vec{r},t) + \ldots \quad (2.1.8)$$

If we introduce the equation (2.1.8) into (2.1.1) and require that all the terms are proportional to λ^N and satisfy the equality separately, we obtain the following set of equations:

$$i\hbar\frac{\partial\psi^{(0)}}{\partial t} = \hat{H}_0\psi^{(0)} \quad (2.1.9a)$$

$$i\hbar\frac{\partial\psi^{(N)}}{\partial t} = \hat{H}_0\psi^{(N)} + \hat{V}\psi^{(N-1)}, N = 1,2,3\ldots \quad (2.1.9b) .$$

The first one (2.1.9a) describes Schrödinger's equation for the atom in the absence of its interaction with the applied field where $\psi^{(0)}$ is the solution, if we assume that for definiteness the atom is initially in ground state (g) and described as:

$$\psi^{(0)}(\vec{r},t) = u_g(\vec{r})e^{-iE_g t/\hbar}. \quad (2.1.10)$$

The other one (2.1.9b) describes the remaining equations in the perturbation expansion and is solved by making use of the energy eigenfunctions for the free atom, which constitute a complete set of basic functions, in terms of which function can be expanded.

Therefore, $\psi^{(N)}$ can be represented as an infinite sum of the free atom eigenfunctions in the form:

$$\psi^{(N)}(\vec{r},t) = \sum_l a_l^{(N)}(t)u_l(\vec{r})e^{-\omega_l t} \quad (2.1.11)$$

where $a_l^{(N)}(t)$ gives the probability amplitude that, to N-th order in the perturbation, the atom is in energy eigenstate l at time t. By substituting (2.1.11) into (2.1.9b) we could come up that the probability amplitudes obey the system equations:

$$i\hbar\sum_l \dot{a}_l^{(N)}(t)u_l(\vec{r})e^{-i\omega_l t} = \sum_l a_l^{(N-1)}(t)\hat{V}(t)u_l(\vec{r})e^{-i\omega_l t} \quad (2.1.12)$$

where the dot denotes a total time derivative.

In order to simplify this equation, we multiply each side from the left by $u_m^*(\vec{r})$, we integrate the resulting equation over all space and we use the orthonormality condition (2.1.6). The resulting equation is:

$$\dot{a}_m^{(N)}(t) = (i\hbar)^{-1}\sum_l a_l^{(N-1)}(t)V_{ml}(t)e^{i\omega_{ml}t} \quad (2.1.13)$$

where $\omega_{ml} = \omega_m - \omega_l$ and the new introduced quantity $V_{ml}(t)$ is defined by the equation:

$$V_{ml}(t) = \langle u_m|\hat{V}|u_l\rangle = \int u_m^*(\vec{r})\hat{V}(t)u_l(\vec{r})d^3r \quad (2.1.14)$$

By straightforward time integration of (2.1.13), the probability amplitude of N-th order can be determined as:

$$a_m^{(N)}(t) = (i\hbar)^{-1} \sum_l \int_{-\infty}^{t} a_l^{(N-1)}(t') V_{ml}(t') e^{i\omega_{ml}t'} dt' \quad (2.1.15)$$

Since we are interested in the determination of the linear and third-order susceptibilities, we will calculate the probability amplitudes up to third-order in the perturbation expansion.

If the interacting optical field E(t) is a plane wave described as:

$$E(t) = E_0 e^{-i\omega t} \quad (2.1.16)$$

Through use of equations (2.1.3) , (2.1.14), (2.1.15) and (2.1.16), we find that:

$$a_m^{(1)}(t) = \frac{-\mu_{mg} E_0}{i\hbar} \int_{-\infty}^{t} e^{i(\omega_{mg}-\omega)t'} dt' \quad (2.1.17)$$

Subsequently, the second order correction to the probability amplitudes is determined by using the equation (2.1.13) but with N=2. Thereby we find that:

$$a_n^{(2)}(t) = (i\hbar)^{-1} \sum_m \int_{-\infty}^{t} a_m^{(1)}(t') V_{nm}(t') e^{i\omega_{nm}t'} dt' \quad (2.1.18)$$

and by substituting the equations (2.1.14) and (2.1.17) into (2.1.18) we have that:

$$a_n^{(2)}(t) = \frac{1}{\hbar^2} \sum_m \frac{E_0^2 \mu_{nm} \mu_{mg}}{(\omega_{ng} - 2\omega)(\omega_{mg} - \omega)} e^{i(\omega_{ng}-2\omega)t} \quad (2.1.19)$$

Similarly, the third order correction to the probability amplitude is given by:

$$a_v^{(3)}(t) = \frac{1}{\hbar^3} \sum_{mn} \frac{E_0^3 \mu_{vn} \mu_{nm} \mu_{mg}}{(\omega_{vg} - 3\omega)(\omega_{ng} - 2\omega)(\omega_{mg} - \omega)} e^{i(\omega_{vg}-3\omega)t} \quad (2.1.20)$$

Having already calculated the probability amplitude corrections up to the third-order, we can now proceed to the determination of the linear and nonlinear optical properties of a material system. According to the rules of quantum mechanics, the expectation value of the electric dipole moment is given by:

$$\langle p \rangle = \langle \psi | \hat{\mu} | \psi \rangle \quad (2.1.21)$$

where ψ is given by the perturbation expansion (2.1.8) with λ set equals to 1.

The first-order correction of the electric dipole moment is:

$$\left\langle p^{(1)} \right\rangle = \left\langle \psi^{(0)} \left| \hat{\mu} \right| \psi^{(1)} \right\rangle + \left\langle \psi^{(1)} \left| \hat{\mu} \right| \psi^{(0)} \right\rangle \quad (2.1.22)$$

which corresponds to the linear properties of the medium . The correction term $\psi^{(0)}$ is given by (2.1.10) and $\psi^{(1)}$ is calculated by equations (2.1.11) and (2.1.17). By substituting these latter expressions into equation (2.1.22) and by taking into account that:

$$\mu_{gm} = \int u_g^* \hat{\mu} u_m d^3 r \quad (2.1.23)$$

and

$$\omega_{mg} = (E_m - E_g)/\hbar = \omega_m - \omega_g \quad (2.1.24)$$

we obtain that the linear contribution in the electric dipole moment is:

$$\left\langle p^{(1)} \right\rangle = \frac{1}{\hbar} \sum_m \left[\frac{\mu_{gm} \mu_{mg} E_0}{(\omega_{mg} - \omega)} e^{-i\omega t} + \frac{(\mu_{mg} E_0)^* \mu_{mg}}{(\omega_{mg}^* - \omega)} e^{i\omega t} \right] \quad (2.1.25)$$

where the possibility of the transition frequency ω_{mg} is allowed to be a complex quantity. From a physical point of view, this complex angular frequency constitutes an elementary way to incorporate the damping phenomena into the theory, since there is always a population decay of the upper level m [1] [4][7][8][9][10].

The linear macroscopic polarization of the material will be given then by the equation:

$$P^{(1)}(\omega) = N \left\langle p^{(1)} \right\rangle \quad (2.1.26)$$

where N is the number density of atoms. By introducing the formal definition for the first-order polarization of an isotropic material:

$$P^{(1)}(\omega) = \varepsilon_0 \chi^{(1)}(\omega) \mathrm{E}(\omega) \quad (2.1.27)$$

and by taking into account (2.1.25) and (2.1.26) for the real part of an applied optical field given by (2.1.16), we are led in the result:

$$\chi^{(1)}(\omega) \approx \frac{2N\mu_{gm}\mu_{mg}}{\varepsilon_0 \hbar(\omega_{mg} - \omega)} \quad (2.1.28)$$

If we assume, that N=1/d^3, where d the lattice constant and that $\mu_{gm} = \mu_{mg} = ea_0$, where a_0 is the Bohr radius of the atom, we find that under highly non-resonant conditions ($\omega << \omega_{mg}$), the linear behavior of the material is expressed by:

$$\chi^{(1)} \approx \frac{2e^2 a_0^2}{\varepsilon_0 d^3 \hbar \omega_{mg}} \quad (2.1.29)$$

Taking the typical values $\omega_{mg} = 10^{16} rad/s$, $d = 3.0 \cdot 10^{-10} m$, $e = 1.6 \cdot 10^{-19} C$, $\hbar = 1.055 \cdot 10^{-34} J \cdot s$ and $a_0 = 0.5 \cdot 10^{-10} m$, one can obtain that $\chi^{(1)} \approx 0.5$, which constitutes a very reasonable value, concerning the order of magnitude, for the first order susceptibility of a material.

Respectively the second-order susceptibility is analogous to the linear case treatment. In this case, we substitute the equation (2.1.22) into (2.1.21) and we collect terms proportional to λ^2 in order to find the second-order contribution to the induced dipole moment per atom which is:

$$\left\langle p^{(2)} \right\rangle = \left\langle \psi^{(0)} \left| \hat{\mu} \right| \psi^{(2)} \right\rangle + \left\langle \psi^{(1)} \left| \hat{\mu} \right| \psi^{(1)} \right\rangle + \left\langle \psi^{(2)} \left| \hat{\mu} \right| \psi^{(0)} \right\rangle \quad (2.1.30)$$

where we define again λ equal to unity. By substituting $\psi^{(0)}$, $\psi^{(1)}$ and $\psi^{(2)}$ from (2.1.10),(2.1.11),(2.1.17) and (2.1.19) we finally get that:

$$\left\langle p^{(2)} \right\rangle = \frac{1}{\hbar^2} \sum_{mn} [\frac{\mu_{gn}(\mu_{nm}E_0)(\mu_{mg}E_0)}{(\omega_{ng} - 2\omega)(\omega_{mg} - \omega)} e^{-i2\omega t} + \frac{(\mu_{ng}E_0)^* \mu_{nm}(\mu_{mg}E_0)}{(\omega_{ng}^* - \omega)(\omega_{mg} - \omega)} + \frac{(\mu_{ng}E_0)^* (\mu_{nm}E_0)^* \mu_{mg}}{(\omega_{ng}^* - \omega)(\omega_{mg}^* - 2\omega)} e^{i2\omega t}] \quad (2.1.31)$$

If we ignore the second term of (2.1.30), which corresponds to a stationary induced dipole moment and assume that:

$$\frac{\mu_{gn}(\mu_{nm}E_0)(\mu_{mg}E_0)}{(\omega_{ng} - 2\omega)(\omega_{mg} - \omega)} \approx \frac{(\mu_{ng}E_0)^* (\mu_{nm}E_0)^* \mu_{mg}}{(\omega_{ng}^* - \omega)(\omega_{mg}^* - 2\omega)} \quad (2.1.32)$$

we can write for the case of highly non-resonant excitation ($\omega << \omega_{mg}$, $2\omega << \omega_{ng}$) that:

$$\left\langle p^{(2)} \right\rangle_{osc} \approx \frac{2\mu_{gn}\mu_{nm}\mu_{mg}E_0^2}{\hbar^2\omega_{ng}\omega_{mg}}\cos 2\omega t \quad (2.1.33)$$

where we have used the Euler's identity . The macroscopic second-order polarization of the medium will be then:

$$P^{(2)}(2\omega)_{osc} = N\left\langle p^{(2)} \right\rangle_{osc} \quad (2.1.34)$$

The formal definition of the second-order polarization for SHG in an isotropic medium is given by:

$$P^{(2)}(2\omega) = \varepsilon_0\chi^{(2)}(2\omega)\mathrm{E}(\omega)\cdot\mathrm{E}(\omega) \quad (2.1.35)$$

which for the real part of an excitation field expressed by (2.1.16), it is transformed into:

$$P^{(2)}(2\omega) = \varepsilon_0\chi^{(2)}(2\omega)E_0^2\cos^2\omega t = \frac{1}{2}\varepsilon_0\chi^{(2)}(2\omega)E_0^2(\cos 2\omega t - 1) \quad (2.1.36)$$

The combination of (2.1.33), (2.1.34) and the oscillating part of (2.1.36) will lead in an approximate expression for the second-order susceptibility (responsible for SHG) of a material, which will become:

$$\chi^{(2)} \approx \frac{4N\mu_{gn}\mu_{nm}\mu_{mg}}{\hbar^2\varepsilon_0\omega_{ng}\omega_{mg}} \quad (2.1.37)$$

For N=1/d^3 and μ in the order of ea_0 , (2.1.37) takes the final form:

$$\chi^{(2)} \approx \frac{4e^3a_0^3}{\varepsilon_0 d^3\hbar^2\omega_{ng}\omega_{mg}} \quad (2.1.38)$$

By taking the following typical values for the above involved quantities $\omega_{mg} = \omega_{ng} = 10^{16} rad/s$, $d = 3.0\cdot10^{-10} m$, $e = 1.6\cdot10^{-19} C$, $\hbar = 1.055\cdot10^{-34} J\cdot s$ and $a_0 = 0.5\cdot10^{-10} m$, one obtains that $\chi^{(2)} \approx 7.5\cdot10^{-12} m/V$. The latter result is in a very good agreement not only with the classical prediction but also with the experimental values presented by several materials [11].

Analogously, the third-order response of a material is given by the λ^3 proportional terms, so that the third-order correction in dipole moment per atom is given by:

$$\left\langle p^{(3)} \right\rangle = \left\langle \psi^{(0)} \left| \hat{\mu} \right| \psi^{(3)} \right\rangle + \left\langle \psi^{(1)} \left| \hat{\mu} \right| \psi^{(2)} \right\rangle + \left\langle \psi^{(2)} \left| \hat{\mu} \right| \psi^{(1)} \right\rangle + \left\langle \psi^{(3)} \left| \hat{\mu} \right| \psi^{(0)} \right\rangle \quad (2.1.39)$$

After the substitution of $\psi^{(0)}$, $\psi^{(1)}$,$\psi^{(2)}$,$\psi^{(3)}$ into (2.1.39) and several calculations, we finally find that:

$$\begin{aligned} \left\langle p^{(3)} \right\rangle = \frac{1}{\hbar^3} \sum_{mnv} [& \frac{\mu_{gv}(\mu_{vn}E_0)(\mu_{nm}E_0)(\mu_{mg}E_0)}{(\omega_{vg}-3\omega)(\omega_{ng}-2\omega)(\omega_{mg}-\omega)} e^{-i3\omega t} \\ & + \frac{(\mu_{vg}E_0)^*\mu_{vn}(\mu_{nm}E_0)(\mu_{mg}E_0)}{(\omega_{vg}^*-\omega)(\omega_{ng}-2\omega)(\omega_{mg}-\omega)} e^{-i\omega t} + \frac{(\mu_{vg}E_0)^*(\mu_{nv}E_0)^*\mu_{nm}(\mu_{mg}E_0)}{(\omega_{vg}^*-\omega)(\omega_{ng}^*-2\omega)(\omega_{mg}-\omega)} e^{i\omega t} \\ & + \frac{(\mu_{vg}E_0)^*(\mu_{nv}E_0)^*(\mu_{mn}E_0)^*\mu_{mg}}{(\omega_{vg}^*-\omega)(\omega_{ng}-2\omega)(\omega_{mg}^*-3\omega)} e^{i3\omega t}] \end{aligned} \quad (2.1.40)$$

For an order of magnitude estimation of third-order susceptibility concerning Third Harmonic Generation (THG) far from resonant conditions, we follow an analogous procedure to the first -order case to derive that:

$$\chi^{(3)} \approx \frac{8e^4 a_0^4}{\varepsilon_0 d^3 \hbar^3 \omega_{vg}\omega_{ng}\omega_{mg}} \quad (2.1.41)$$

which for typical values of the involved parameters gives:

$$\chi^{(3)} \approx 3.6 \cdot 10^{-22} m^2/V^2 \quad (2.1.42)$$

in a total agreement with both the classical anharmonic oscillator model predictions and the experimental values from a variety of materials [11].

2.2 Wave-Equation Description of Nonlinear Optical Interactions

The nonlinear electromagnetic wave equation

In the previous chapter, we have seen how the nonlinearity in the response of a material system to an intense laser field can cause the polarization of the medium to develop new frequency components and tried to use laws of quantum mechanics in order to derive explicit expressions for the nonlinear optical susceptibility. In the present chapter, the Maxwell equations are used, in order to describe the generation of the new frequency components of the polarization after acting with the electromagnetic field.

The propagation of light in a nonlinear medium is governed by the wave equation, which was derived from Maxwell's equations:

$$\vec{\nabla} \cdot \vec{E} = \frac{\rho}{\varepsilon_0} \quad (2.2.1) \qquad \text{(Gauss's law for electric fields)}$$

$$\vec{\nabla} \cdot \vec{B} = 0 \quad (2.2.2) \qquad \text{(Gauss's law for magnetic fields)}$$

$$\vec{\nabla} \times \vec{E} = -\frac{\partial \vec{B}}{\partial t} \quad (2.2.3) \qquad \text{(Faraday's law)}$$

$$\vec{\nabla} \times \vec{B} = \mu_0 \left(\vec{J} + \varepsilon_0 \frac{\partial \vec{E}}{\partial t} \right) \quad (2.2.4) \qquad \text{(Ampere's law)}$$

where ρ(r,t) is the density of free charges , ε_0 is the vacuum permittivity , μ_0 is the magnetic permeability and $\vec{J}$ (r,t) the corresponding current density of free charges.

It is convenient to be restricted in regions of space that contain no free charges and currents, so that ρ=0 (2.2.5) and $\vec{J}$=0 (2.2.6) respectively. While it is assumed that the material is nonmagnetic so that $\vec{B} = \mu_0 \vec{H}$ (2.2.7).

However, the nonlinear material ensures that the fields $\vec{E}$ and $\vec{D}$ are related by:

$$\vec{D} = \varepsilon_0 \vec{E} + \vec{P} \quad (2.2.8)$$

where $\vec{P}$ is the polarization vector which depends nonlinearly with the electric field strength $\vec{E}$.

Then, we proceed to derive the optical wave equation in the usual manner. Firstly, we take the curl of the curl $\vec{E}$ Maxwell equation (2.2.3):

$$\vec{\nabla}\times(\vec{\nabla}\times\vec{E}) = -\frac{\partial(\vec{\nabla}\times\vec{B})}{\partial t} \quad (2.2.9)$$

After that interchange, the order of the space and time derivatives on the right hand side of the resulting equation, and we use the equations (2.2.4),(2.2.6), (2.2.7) in order to replace the $\vec{\nabla}\times\vec{B}$ by $\mu_0\left(\frac{\partial\vec{D}}{\partial t}\right)$,to end up with the equation:

$$\vec{\nabla}\times\vec{\nabla}\times\vec{E} + \mu_0\frac{\partial^2\vec{D}}{\partial t^2} = 0 \quad (2.2.10)$$

In order to eliminate $\vec{D}$ from this equation, we substitute equation (2.2.8) into (2.2.10) and thereby we obtain the equation:

$$\vec{\nabla}\times\vec{\nabla}\times\vec{E} + \frac{1}{c^2}\frac{\partial^2\vec{E}}{\partial t^2} = -\mu_0\frac{\partial^2\vec{P}}{\partial t^2} \quad (2.2.11)$$

The above expression constitutes the most general form of the wave equation in nonlinear optics and it can be simplified after several calculations into the expression:

$$\vec{\nabla}^2\vec{E} - \frac{1}{c^2}\frac{\partial^2\vec{E}}{\partial t^2} = \mu_0\frac{\partial^2\vec{P}}{\partial t^2} \quad (2.2.12)$$

It is convenient to write the polarization density as a sum of linear and nonlinear parts as:

$$\vec{P} = \vec{P}^{(1)} + \vec{P}^{NL} \quad (2.2.13)$$

where the first order polarization is given by the equation:

$$\vec{P}^{(1)} = \varepsilon_0\chi^{(1)}\vec{E} \quad (2.2.14)$$

While for an isotropic material, the relative permittivity of a medium $\varepsilon^{(1)}$ is related to its first-order electric susceptibility $\chi^{(1)}$ as:

$$\varepsilon^{(1)} = 1 + \chi^{(1)} \quad (2.2.15)$$

Combining the equations (2.2.12)-(2.2.16), the wave equation for the case of an isotropic dispersionless material that obtain is:

$$\vec{\nabla}^2 \vec{E} - \frac{n^2}{c^2} \frac{\partial^2 \vec{E}}{\partial t^2} = \mu_0 \frac{\partial^2 \vec{P}^{NL}}{\partial t^2} \quad (2.2.16)$$

where n is a linear index of refraction that satisfies the relation $n^2 = \varepsilon^{(1)}$ and $c^2 = \frac{1}{\varepsilon_0 \mu_0}$.

The above equation (2.2.16) has the form of a driven wave equation, since the nonlinear response of the medium acts as a source term, which appears on the right hand side. In the absence of this source term, equation (2.2.16) admits solutions of the form of free waves by propagating with velocity c/n [7].

Plane wave

In order to predict the intensity of the irradiation emitted during N-th harmonic generation process for a collimated, monochromatic, continuous wave, the nonlinear optical wave equation (2.2.16) are used.

Therefore, the fundamental and N-th harmonic fields could been taken as plane waves of the form:

$$E_1(z,t) = A_1(z) e^{i(k_1 z - \omega_1 t)} + c.c. \quad (2.2.17) \qquad \textit{Fundamental wave}$$

$$E_N(z,t) = A_N(z) e^{i(k_N z - \omega_N t)} + c.c \quad (2.2.18) \qquad \textit{N-th Harmonic wave (N = 2, 3, 4...)}$$

where $A_1(z)$ and $A_N(z)$ is the spatially slowly varying assumed field amplitudes of the fundamental and harmonic waves respectively, and $\omega_N = N\omega_1$ (2.2.19).

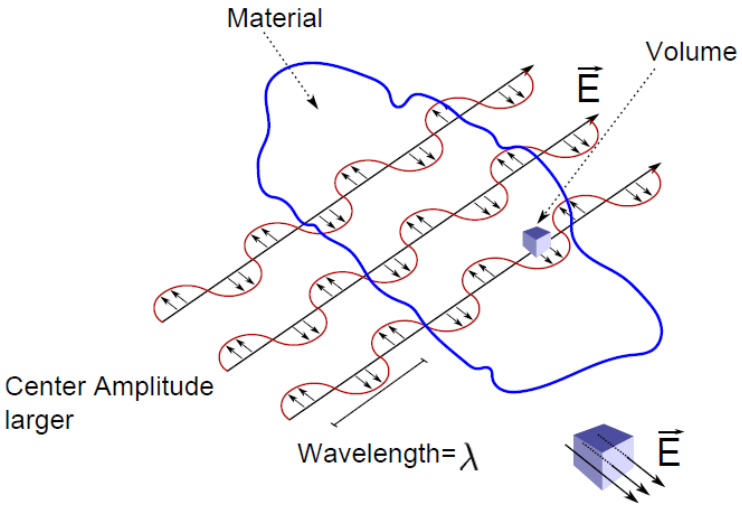

***Figure 2.2.1**: Light inducing a polarization inside a material. The light source is a monochromatic plane wave.*

Respectively the nonlinear polarization of N-th order will be given by the expression:

$$P_N(z,t) = \varepsilon_0 \chi^{(N)} [E_1(z,t)]^N \quad (2.2.20)$$

After introducing (2.2.18) and (2.2.19), equation (2.2.20) has the form of:

$$P_N(z,t) = \varepsilon_0 \chi^{(N)} [A_1(z)]^N e^{i(Nk_1 z - \omega_N t)} + c.c. \quad (2.2.21)$$

Furthermore, if the expressions (2.2.18) and (2.2.21) are introduced into the wave equation (2.2.16), we could easily find after calculations that:

$$\begin{aligned} &\frac{\partial^2 A_N(z)}{\partial z^2} e^{i(k_n z - \omega_N t)} + 2\frac{\partial A_N(z)}{\partial z} i k_N e^{i(k_N z - \omega_N t)} - A_N(z) k_N^2 e^{i(k_N z - \omega_N t)} \\ &+ \frac{n_N^2}{c^2} A_N(z) \omega_N^2 e^{i(k_N z - \omega_N t)} + c.c. = -\varepsilon_0 \mu_0 \chi^{(N)} [A_1(z)]^N \omega_N^2 e^{i(Nk_1 z - \omega_n t)} + c.c. \end{aligned} \quad (2.2.22)$$

The above expression can be simplified, if the first term on the left hand side on the ground is neglected, because it is much smaller than the second. This approximation is known as slowly varying amplitude approximation and it is valid when:

$$\left| \frac{\partial^2 A_N(z)}{\partial z^2} \right| << \left| k_N \frac{\partial A_N(z)}{\partial z} \right| . \quad (2.2.23)$$

The condition requires that the fractional change $A_N(z)$ in a distance of the order of an optical wavelength must be much smaller than unity.

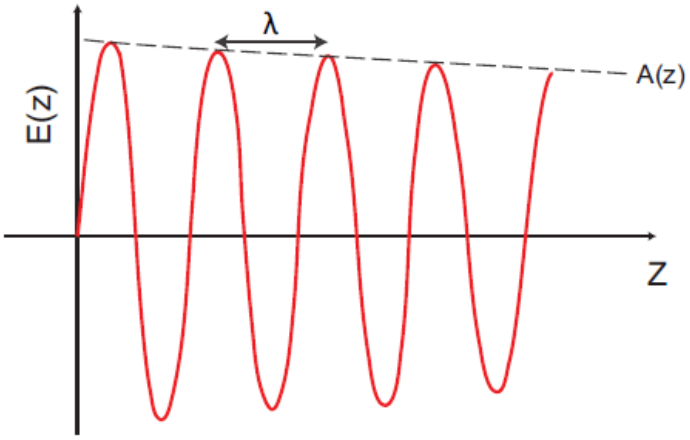

Figure 2.2.2: *Slowly varying envelope approximation: the variation of A(z) with respect to z is much smaller than the wavelength of the field's oscillation.*

Moreover, the third and fourth terms are cancelled since:

$$k_N = \frac{n_N \omega_N}{c} \quad (2.2.24)$$

As a result, the equation that is obtained is the following:

$$\frac{\partial A_N(z)}{\partial z} = \frac{i\chi^{(N)}\omega_N^2}{2c^2 k_N}[A_1(z)]^N e^{i\Delta kz} \quad (2.2.25)$$

where it was set:

$$c^2 = \frac{1}{\varepsilon_0 \mu_0} \quad (2.2.26)$$

and the quantity that has been introduced is:

$$\Delta k = Nk_1 - k_N \quad (2.2.27)$$

which is called the wavevector mismatch.

Then we proceed to the integration of expression (2.2.25) from zero to a propagation distance L and the amplitude of N-th harmonic generation that we get has the form:

$$A_N(L) = \frac{i\chi^{(N)}\omega_N^2[A_1]^N}{2c^2k_N}\int_0^L e^{i\Delta kz}dz = \frac{i\chi^{(N)}\omega_N^2[A_1]^N}{2c^2k_N}\cdot\left(\frac{e^{i\Delta kL}-1}{i\Delta k}\right) \quad (2.2.28)$$

Thus, the radiation intensity of the N-th harmonic plane wave can be easily calculated by using the magnitude of the time – averaged Poynting vector of field amplitude:

$$I_N = 2n_N\varepsilon_0 c|A_N|^2 \quad (2.2.29)$$

and after introducing the equation (2.2.28) into (2.2.29) we find that:

$$I_N = \frac{n_N\varepsilon_0[\chi^{(N)}]^2\omega_N^4|A_1|^{2N}}{2k_N^2c^3}\left|\frac{e^{i\Delta kL}-1}{\Delta k}\right|^2 \quad (2.2.30)$$

The above expression can alternatively be expressed as:

$$I_N = \frac{N^2\omega_1^2[\chi^{(N)}]^2 I_1^N L^2}{2^{N+1}n_1^N n_N\varepsilon_0^{N-1}c^{N+1}}\sin c^2\left(\frac{\Delta kL}{2}\right) \quad (2.2.31).$$

For N=2, equation (2.2.31) will have the form:

$$I_2 = \frac{\omega_1^2[\chi^{(2)}]^2 I_1^2 L^2}{2n_1^2 n_2\varepsilon_0 c^3}\sin c^2\left(\frac{\Delta kL}{2}\right) \quad (2.2.32)$$

which describes the intensity of Second Harmonic Generation (SHG). The intensity maximizes for Δk=0 and is called perfect phase matching.

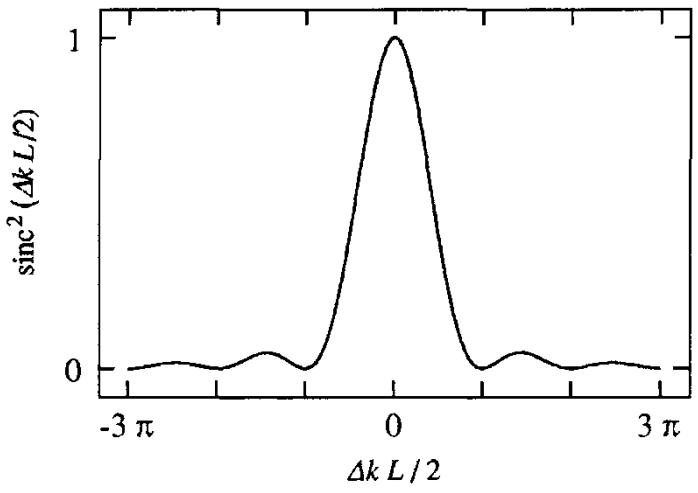

Figure 2.2.3.: *Effects of the wavevector mismatch on the optical harmonics generation efficiency. The intensity of the nonlinear irradiation is maximized for Δk = 0.*

In contrast to the Second Harmonic Generation (SHG), which requires a non-centrosymmetric medium, Third Harmonic Generation (THG) can appear to every kind of material. Nevertheless, the optical harmonic signal is obtained only if the phase matching condition is fulfilled, which means that the individual generated harmonic waves are added totally constructively, when the excitation light propagates through the material.

In case of plane wave, which is characterized by a wavenumber k_1 and for N-th harmonic order, the perfect phase matching implies that the quantity:

$$\Delta k = Nk_1 - k_N = 0 \quad (2.2.33)$$

This can be achieved if the refractive index that is experienced by the excitation light is equal to the refractive index experienced, by the generated optical harmonic. Otherwise, by substituting (2.2.24) into (2.2.33) we obtain that:

$$\frac{n_1 N\omega_1}{c} = \frac{n_N \omega_N}{c} \quad (2.2.34)$$

which ends up, by using the equation (2.2.19), to the expression:

$$n_1 = n_N \quad . (2.2.35)$$

Phase matching conditions and optical harmonics generation could be achieved by using birefringent materials. These materials have an index of refraction, which depends on the polarization and propagation direction of the incident light. However, in case of biological samples harmonic generation occurs in the presence of a large wavevector mismatch, which is leading to a greatly reduced efficiency of the whole process. Nonetheless, the conversion efficiency is typically sufficient enough to produce a signal that can be detected by extremely sensitive photomultiplier devices. As a result, harmonic generation is useful as a method to study certain biological structures (e.g. lipids) [4] [7-9].

2.3 Gaussian beams

In the previous section, the nonlinear optical process of harmonic generation is described for the infinite plane waves. In this chapter the case of the focusing laser beam into the sample will be discussed, by assuming a Gaussian spatial profile.

The nonlinear optical wave equation will be used once again, in order to describe the Gaussian beams:

$$\vec{\nabla}^2\vec{E} - \frac{n^2}{c^2}\frac{\partial^2\vec{E}}{\partial t^2} = \mu_0\frac{\partial^2\vec{P}^{NL}}{\partial t^2} \quad (2.3.1)$$

and the electric field $\vec{E}$ and polarization $\vec{P}^{NL}$ are expressed as:

$$\vec{E}_N(\vec{r},t) = \vec{A}_N(r)e^{i(k_N z-\omega_N t)} + c.c. \quad (2.3.2)$$

$$\vec{P}^{NL}(\vec{r},t) = \vec{p}_N(r)e^{i(k'_N z-\omega_N t)} + c.c. \quad (2.3.3)$$

where it is allowed to represent the non-plane waves by allowing the complex amplitudes A_N and p_N to be spatially varying quantities. In addition, the possibility of a wavevector is allowed to mismatch, by allowing the wavevector of $\vec{P}^{NL}$ to be different than that of $\vec{E}$. Furthermore, the z direction had been specified to be the dominant direction of propagation of the wave $\vec{E}$, so that it could be easily expressed by the Laplace operator as:

$$\vec{\nabla}^2 = \frac{\partial^2}{\partial z^2} + \vec{\nabla}_T^2 \quad (2.3.4)$$

The second term represents the transverse Laplacian and is given by:

$$\vec{\nabla}_T^2 = \frac{\partial^2}{\partial x^2} + \frac{\partial^2}{\partial y^2} \quad (2.3.5)$$

Thus, by substituting equations (2.3.2) and (2.3.3) into (2.3.1), the Laplacian could be replaced and make the slowly varying amplitude approximation, the final equation becomes:

$$2ik_N\frac{\partial\vec{A}_N(r)}{\partial z} + \vec{\nabla}_T^2\vec{A}_N(r) = -\frac{\omega_N^2}{\varepsilon_0 c^2}\vec{p}_N(r)e^{i\Delta kz} \quad (2.3.6)$$

where $\Delta k = k'_N - k_N$ (2.3.7) is the wavevector mismatch.

The electric field component of a Gaussian beam can be represented in the scalar approximation by the expression:

$$A(r,z) = A_0 \frac{w_0}{w(z)} e^{-r^2/w(z)^2} e^{ikr^2/2R(z)} e^{i\phi(z)} \quad (2.3.8)$$

where $w(z) = w_0 \sqrt{1 + \left(\frac{\lambda z}{\pi w_0^2}\right)}$ (2.3.9) is the beam width , where $R(z) = z\left[1 + \left(\frac{\pi w_0^2}{\lambda z}\right)^2\right]$ (2.3.10) is the wavefront radius of curvature after propagating distance z , and where $\phi(z) = -\arctan\left(\frac{\lambda z}{\pi w_0^2}\right)$ (2.3.11) describes a phase that is associated with the spatial and the temporal change of the curvature of the wavefront known as Gouy shift.

Moreover, in the above formulas, r represents the radial distance from the center axis of the beam and z is the distance propagated from the plane, where the wavefront is flat , λ represents the wavelength of light and w_0 represents the radius of the $1/e^2$ irradiance contour at the plane wave has propagated a distance z. R(z) is infinite at z=0, passes through a minimum at some infinite z, and rises again toward infinity as z is further increased, asymptotically and approaching the value of z itself. The plane z=0 marks the location of a Gaussian waist or a place, where the wavefront is flat, and w_0 is called the beam waist radius.

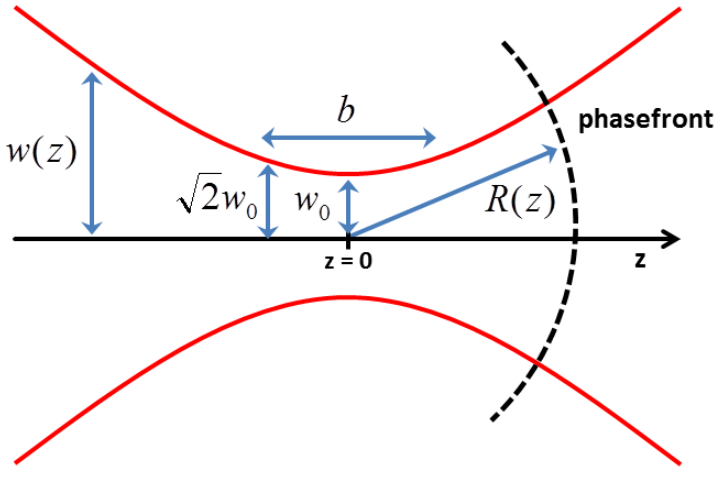

Figure 2.3.1: *Gaussian beam width w(z) as a function of the axial distance z. w_0 is the beam waist radius, b the confocal parameter and R(z) the radius of curvature of the optical phasefront.*

However, it is often convenient to represent the Gaussian beam in the more compact form

$$A(r,z)=\frac{A_0}{1+i\zeta}e^{-r^2/w_0^2(1+i\zeta)} \quad (2.3.12)$$

where $\zeta=\frac{2z}{b}$ (2.3.13) is the longitudinal coordinate defined in terms of the confocal parameter $b=\frac{2\pi w_0^2}{\lambda}$ (2.3.14), which is a measure of the longitudinal extent .

In case of N-th harmonic generation excited by a Gaussian fundamental beam, the nonlinear polarization is expressed by the equation:

$$p_N(r)=\varepsilon_0\chi^{(N)}(A_1(r,z))^N \quad (2.3.15)$$

where the complex amplitude $A_1(r,z)$ is described by the equation:

$$A_1(r,z)=\frac{A_0^{(1)}}{1+i\zeta}e^{-r^2/w_0^2(1+i\zeta)} \quad (2.3.16)$$

Nevertheless, the constant-pump approximation is used in order to solve the optical wave equation for the case of the N-th harmonic by adopting the trial solution:

$$A_N(r,z)=\frac{A_0^{(N)}(z)}{1+i\zeta}e^{-Nr^2/w_0^2(1+i\zeta)}. \quad (2.3.17)$$

It should be noted that the trial solution corresponds to a beam with the same confocal parameter as a fundamental beam equation (2.3.16); this means that the harmonic wave is generated coherently over a region whose longitudinal extent is equal to that of the fundamental wave.

Furthermore, by substituting equation (2.3.15) into (2.3.6) the equation that is transformed is the following:

$$2ik_N\frac{\partial A_N(r,z)}{\partial z}+\nabla_T^2A_N(r,z)=-\frac{\omega_N^2}{c^2}\chi^{(N)}(A_1(r,z))^Ne^{i\Delta kz} \quad (2.3.18)$$

where $\Delta k=Nk_1-k_N$ (2.3.19) is the wavevector mismatch, and $\omega_N=q\omega$ is the frequency component.

By introducing the trial equation (2.3.17) into the equation (2.3.18), it is found that:

$$\frac{\partial A_0^{(N)}}{\partial z} = \frac{iN\omega}{2n_N c}\chi^{(N)}(A_0^{(1)})^N \frac{e^{i\Delta kz}}{(1+i\zeta)^{N-1}} \quad (2.3.19)$$

The equation can be integrated directly to obtain:

$$A_0^{(N)} = \frac{iN\omega}{2n_N c}\chi^{(N)}(A_0^{(1)})^N J_N(\Delta k, z_0, z) \quad (2.3.20),$$

where:

$$J_N(\Delta k, z_0, z) = \int_{z_0}^{z} \frac{e^{i\Delta kz'}}{(1+2iz'/b)^{N-1}} dz' \quad (2.3.21)$$

and z_0 expresses the value of z at the entrance to the nonlinear medium.

The integral appearing in equation (2.3.21) can be evaluated analytically for certain special cases. One such case is the plane wave limit, where $b >> |z_0|, |z|$. In this limit the integral reduces to:

$$J_N(\Delta k, z_0, z) = \int_{z_0}^{z} e^{i\Delta kz'} dz' = \frac{e^{i\Delta kz} - e^{i\Delta kz_0}}{i\Delta k} \quad (2.3.22)$$

which implies that:

$$|J_N(\Delta k, z_0, z)|^2 = L^2 \sin c^2\left(\frac{\Delta kL}{2}\right) \quad (2.3.23)$$

where $L = z - z_0$ is the length of the interaction region.

The other opposite limiting case is that in which the fundamental wave is focused tightly within the interior of the nonlinear medium so that $b << |z_0|, |z|$. In this case the integral's limit is replaced by plus and minus infinity:

$$J_N(\Delta k, z_0, z) = \int_{-\infty}^{\infty} \frac{e^{i\Delta kz'}}{(1+2iz'/b)^{N-1}} dz' \quad (2.3.24)$$

and after integration we obtain that:

$$J_N(\Delta k, z_0, z) = \begin{cases} 0 & ,\Delta k \le 0, \\ \dfrac{b}{2} \cdot \dfrac{2\pi}{(N-2)!} \left(\dfrac{b\Delta k}{2} \right)^{N-2} e^{-b\Delta k/2} & ,\Delta k > 0. \end{cases} \quad (2.3.25)$$

This functional form is illustrated for the case of third harmonic generation (q=3) as represented in figure2.3.4. It is observed that THG vanishes identically for the case of perfect phase matching (Δk=0) and it is maximized through the use of a positive wavevector mismatch. This effect is known as the phase anomaly; it was firstly studied systematically by Gouy (1890) and shifted by π radians that are experienced by any beam passes through its focus.

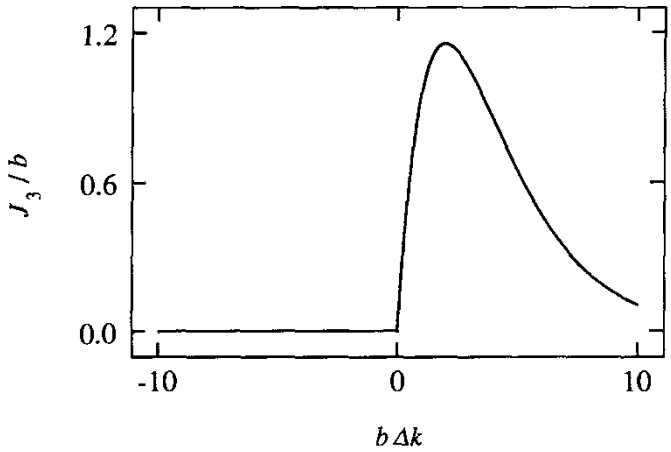

Figure 2.3.4: *Dependence of the phase matching factor J_3 for THG on the normalized confocal parameter bΔk, in the tight focusing limit.*

Consequently, the nonlinear polarization will be unable to couple efficiently to the generated wave of amplitude A_N unless a wavevector mismatch Δk is introduced to compensate for the phase shift due to passage of the incident wave through its focus. The reason why Δk should be positive can be understood intuitively from the below figure.

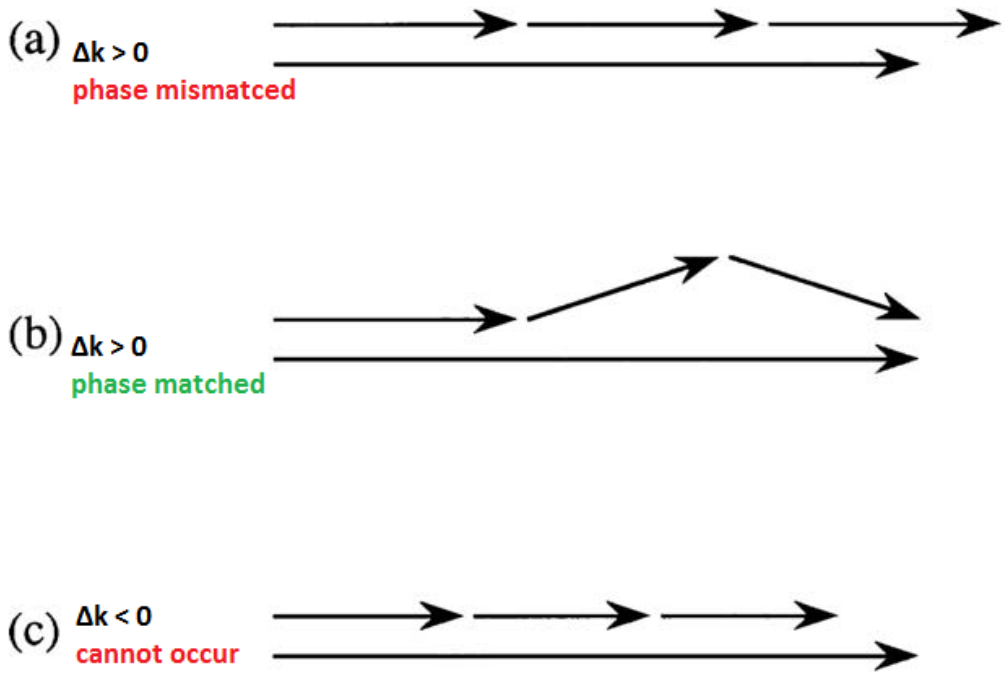

Figure 2.3.5.: *Illustration of why a positive value of Δk is eligible in harmonic generation with* focused laser beams. (a) Wavevector diagram for THG with Δk>0 .Even though that process is phase mismatched , the fundamental beam contains an angular spread of wavevectors and the phase – matched process illustrated in (b) can occur high efficiency.(c)Conversely , for Δk negative, efficient harmonic generation cannot occur (momentum conservation cannot be met).

In order to describe more precisely the Gouy phase, the Gaussian wave is expressed in the form:

$$E(z,r,t) = A_0 \frac{w_0}{w(z)} e^{-r^2/w(z)^2} \cos(\omega t - \left[k(z - z_0) - \phi + kr^2/2R\right]) \quad (2.3.26)$$

Where A_0 is the amplitude, w_0 represents the beam radius in the beam waist, z_0 is the position of the beam waist, w (z) is the beam radius at the position z-z_0 , k is the wave vector of the radiation , ϕ is the Gouy phase , and $kr^2/2R$ is a phase in lateral direction that becomes zero on the beam axis; the phase ϕ_0 is chosen so that waist lies at z_0. The beam radius is

$w(z) = w_0\sqrt{1+\left(\frac{z - z_0}{z_R}\right)^2}$, where $z_R = kw_0^2/2 = \pi w_0^2/\lambda$ is the Rayleigh range. The Gouy phase is given by $\phi(z) = \tan^{-1}\left(\frac{z - z_0}{z_R}\right)$. The curvature of the wave front is:

$$R(z) = z - z_0 + \left(\frac{z_R^2}{z - z_0}\right) \quad (2.3.27).$$

The derivative of the time- dependent portion ϕ_t of the phase yields the frequency,

$$d\phi_t / dt = \omega \quad (2.3.28).$$

For the position-dependent portion of the phase:

$$\phi(z) = k(z - z_0) - \phi \quad (2.3.29)$$

By differentiation, we obtain that the effective vector is:

$$k_{eff} = k - d\phi_t / dz \quad (2.3.30)$$

The effective length is:

$$\lambda_{eff} = \frac{2\pi}{k_{eff}} = \frac{\lambda}{1 - k^{-1} d\phi / dz} = \frac{\lambda}{1 - \lambda/(2\pi) d\phi / dz} \quad (2.3.31)$$

where $\lambda = (2\pi)/k$ is the wavelength of the radiation for outside the beam waist. The effective wave vector and the effective wavelength depend on the position z. The Gouy phase (figure 2.3.6) shows the strongest change in the Rayleigh range and the derivative:

$$d\phi / dz = \frac{1}{1 + (z - z_0)^2 / z_R^2} \quad (2.3.32)$$

has a maximum at the center of the beam waist. The phase far outside the beam waist, at $z - z_0 << 0$, is given by:

$$\phi_z = k_{eff} \times (z - z_0) \quad (2.3.33)$$

And for the range far outside the beam waist at $z - z_0 >> 0$ described by:

$$\phi_z = k_{eff} \times (z - z_0) - \pi \text{ . (2.3.34)}$$

The Gouy phase shift at a transit of radiation through the beam waist is π. In the range of the beam waist, the effective wavelength is larger than λ. In the center of the beam waist, the effective wavelength is equal to $\lambda_{eff} = \lambda + \lambda/(4\pi)$ (2.3.35). The wavefront have the largest distance in the center of the beam waist. The sum of all differences $\lambda_{eff} - \lambda$ at a transit of radiation through the beam waist is equal to $\lambda/2$ [6] [9] [12].

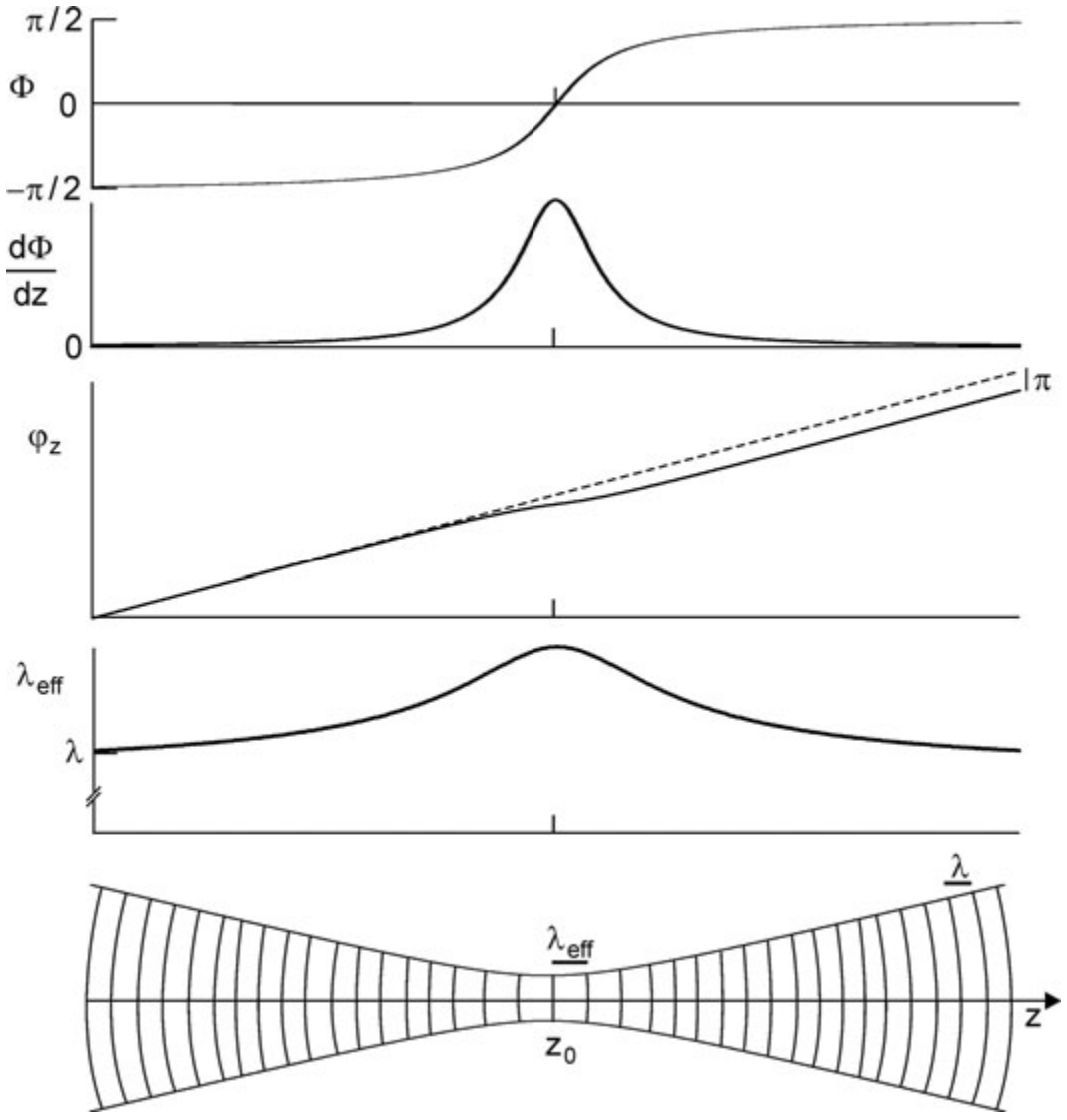

***Figure 2.3.6**.: Gaussian beam: Gouy phase; variation of the Gouy phase; spatial part (dashed) of the phase and total phase (Solid); effective wavelength; wavefront.*

Chapter 3.Fluorescence

The term fluorescence is related to the capability of certain molecules to emit light (in a time scale of 10^{-9} s) when they are illuminated with a proper wavelength. More precisely, the energy required to prime fluorescence is the energy that is necessary to produce a molecular transition to an electronic excited state. In other words, if λ is the wavelength of the light delivered on the sample, the energy provided by photons $E = c/\lambda$ (where $h = 6.6 \times 10^{-34}$ J s is the Plank's constant and $c = 3\times 10^{8}$ ms^{-1} is the speed of light) should be equal to the molecular energy gap ΔE_g between the ground state and one vibrational or rotational level of the electronic excited state: $\Delta E_g = E = hc/\lambda$.

Once the molecule has adsorbed the photon, it has several pathways for relaxing back to the ground state, including non-radiative phenomena, phosphorescence (associated to the forbidden transition to the triplet state) and fluorescence (Fig.3.1). In fluorescence the internal conversion from the lower vibrational level of the excited state is associated with light emission while the relaxation to the ground state is achieved by emitting one photon. For this reason, the fluorescence emission is generally shifted towards a longer wavelength than the one used for exciting the molecule. This phenomenon is known as Stokes' shift and it ranges from 50 to 200nm depending on the fluorescent molecule in consideration.

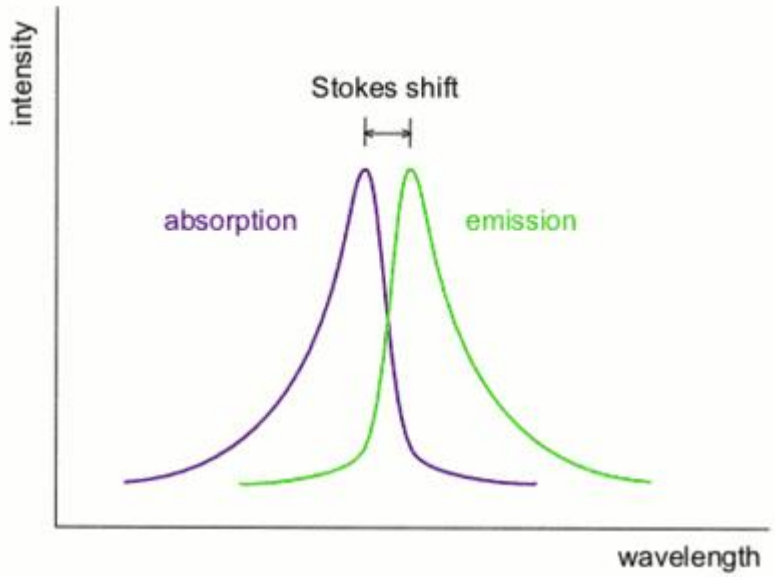

***Figure 3.1**.: Stokes shift is a phenomenon common to photoluminescent materials in which the activated material emits photons at different wavelengths than the photons it absorbed.*

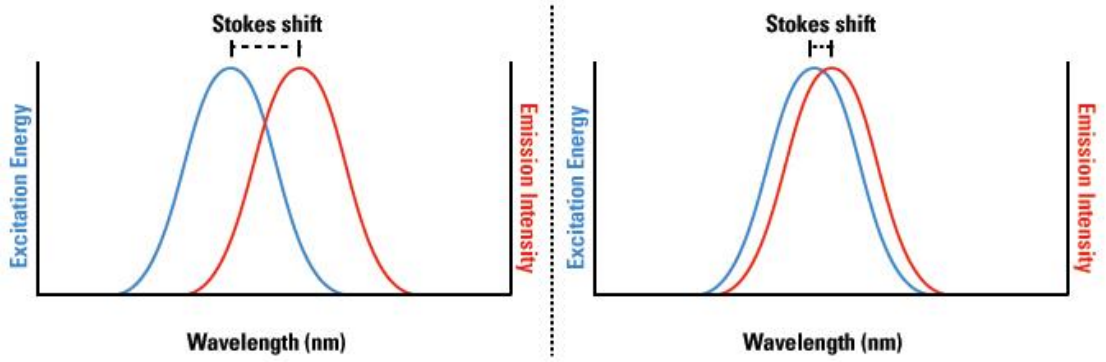

***Figure** 3.2: The Stokes shift of the excitation and emission spectra of a fluorophore.* Fluorophores with greater Stokes shifts (left) show clear distinction between excitation and emission light in a sample, while fluorophores with smaller Stokes shifts (right) exhibit greater background signal because of the smaller difference between excitation and emission wavelengths.

Conventional imaging techniques use ultraviolet or visible light for the excitation. In multi-photon excitation the jump between the ground state and the excited one is due to the simultaneous absorption of two or more photons. As the sum of the energy of the absorbed photons must match the molecular energy gap, multi-photon processes allow using longer excitation wavelength. Multi-photon microscopy generally uses infrared (IR) light for the excitation, resulting in the increase of penetration depth in turbid media and in the decrease of the photo-toxicity in biological samples.

Due to the fact that the molecule is memoryless of the way in which excitation is accomplished, the two-photon induced fluorescence retains the same characteristics of conventional emission process. Therefore, in multiphoton excitation, the fluorescent emission is generally at shorter wavelengths than the one absorbed by the molecule.

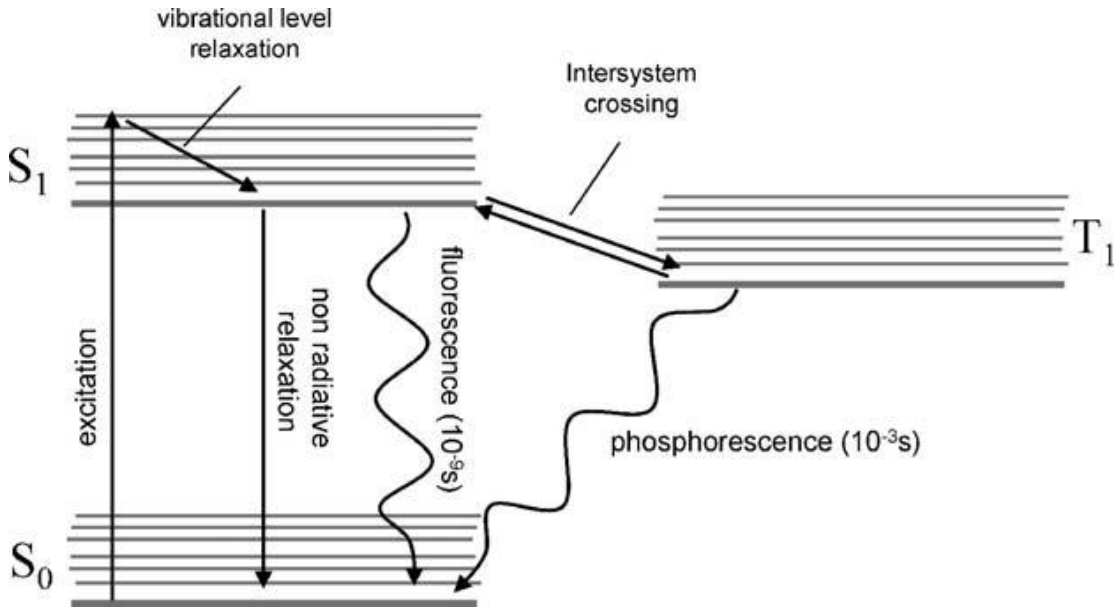

***Figure 3.3**.: Perrin–Jablonski diagram representing the possible pathways for one molecule to relax back to the ground state once excited.*

In the next chapters, the theory of one-photon and multiphoton absorption is presented. Specifically, these two stages are described in case of the atomic system is treated quantum mechanically. At the end some equations briefly defined, in order to have a further understanding of the procedure.

Theory of Single and Multiphoton Absorption

In this section, quantum mechanics laws will be used in order to calculate single and multiphoton absorption rates. The calculation uses procedures similar to those used in section 2.1 to calculate the nonlinear susceptibility. Initially it is assumes that the atomic wave function $\psi(\vec{\mathrm{r}},\mathrm{t})$ obeys the time dependent Schrodinger's equation:

$$i\hbar\frac{\partial\psi(\vec{\mathrm{r}},\mathrm{t})}{\partial\mathrm{t}}=\hat{H}\psi(\vec{r},t) \quad (3.1)$$

where the Hamiltonian is expressed by:

$$\hat{H}=\hat{H}_0+\hat{V}(t) \quad (3.2)$$

Here $\hat{H}_0$ is the Hamiltonian for a free atom and:

$$\hat{V}(t)=-\hat{\mu}E(t) \quad (3.3)$$

where $\hat{\mu}=e\hat{r}$ (3.4) is the interaction energy with the applied optical field. In order to simplify the calculations, take monochromatic wave of the form:

$$E(t)=Ee^{-i\omega t}+c.c. \quad (3.5)$$

which is switched suddenly at time t=0.

Then we proceed by assuming that the solutions to Schrodinger's equation for a free atom are known, and that the wavefunctions associated with the energy eigenstates can be represented as:

$$\psi_n(\vec{r},t)=u_n(\vec{r})e^{-i\omega_n t} \quad (3.6)$$

where $\omega_n=E_n/\hbar$ is the angular frequency. (3.7)

The above expression (3.6) , will satisfy the equation (3.1) (with $\hat{H}=\hat{H}_0$), if u_n satisfies the eigenvalue equation:

$$\hat{H}_0u_n(\vec{r})=E_nu_n(\vec{r}) \quad (3.8)$$

In case of the presence of a time dependent interaction potential $\hat{V}(t)$, Schrodinger's equation will have the form:

$$i\hbar\frac{\partial\psi(\vec{\mathrm{r}},\mathrm{t})}{\partial\mathrm{t}}=(\hat{H}_0+\hat{V}(t))\psi(\vec{r},t) \quad (3.9)$$

The solution of the above equation (3.9) can be expressed as a linear combination of the free atom $\hat{H}_0$ eigenstates as:

$$\psi(\vec{r},t) = \sum_l a_l(t) u_l(\vec{r}) e^{-i\omega_l t} \quad (3.10)$$

By introducing equation (3.10) into (3.9), we obtain that:

$$\begin{aligned} &i\hbar \sum_l \frac{da_l(t)}{dt} u_l(\vec{r}) e^{-i\omega_l t} + i\hbar \sum_l (-i\omega_l) a_l(t) u_l(\vec{r}) e^{-i\omega_l t} \\ &= \sum_l a_l(t) \hat{H}_0 u_l(\vec{r}) e^{-i\omega_l t} + \sum_l a_l(t) \hat{V}(t) u_l(\vec{r}) e^{-i\omega_l t} \end{aligned} \quad (3.11)$$

where (since $E_l = \hbar\omega_l$) clearly the second and the third terms cancel. To simplify this expression even further, we multiply both sides by the factor $u_m^*(\vec{r})$, we integrate over all space and we get that:

$$\int u_m^*(\vec{r}) i\hbar \sum_l \frac{da_l(t)}{dt} u_l(\vec{r}) e^{-i\omega_l t} d^3r = \int u_m^*(\vec{r}) \sum_l a_l(t) \hat{V}(t) u_l(\vec{r}) e^{-i\omega_l t} d^3r \quad (3.12)$$

Furthermore by using the orthonormality condition:

$$\int u_m^*(\vec{r}) u_l(r) d^3r = \delta_{ml} \quad (3.13)$$

we obtain that:

$$i\hbar \frac{da_m(t)}{dt} = \sum_l a_l(t) V_{ml} e^{-i\omega_{lm} t} \quad (3.14)$$

where $\omega_{lm} = \omega_l - \omega_m$ (3.15) and where:

$$V_{ml} = \int u_m^*(\vec{r}) \hat{V} u_l(\vec{r}) d^3r \quad (3.16)$$

Equation (3.14) is a matrix form of Schrodinger equation and equation (3.16) is the matrix elements of the interaction Hamiltonian $\hat{V}$.

However, the equation (3.14) cannot simply be solved exactly, for this reason perturbation technique is used. To this end, an expansion parameter λ is continuously introduced, which is assumed to vary continuously between zero and one. The value λ=1 is taken to correspond

to the physical situation at hand. Firstly, we replace V_{ml} by λV_{ml} in (3.14) and we expand $a_m(t)$ in a power series as:

$$a_m(t) = a_m^{(0)}(t) + \lambda a_m^{(1)}(t) + \lambda^2 a_m^{(2)}(t) + \ldots \quad (3.17)$$

By equating powers of λ on each side of the resulting form of the equation (3.14), we obtain the set of equations:

$$\frac{da_m^{(N)}(t)}{dt} = \frac{1}{i\hbar}\sum_l a_l^{(N-1)}(t) V_{ml} e^{-i\omega_{lm}t} \quad , N = 1,2,3\ldots \quad (3.18)$$

Initially, one photon absorption is described by the linear form of equation (3.18) by setting N=1 which corresponds to a first order interaction in the field. Firstly, we assume that in absence of the applied laser field is in the stage g (ground state) so that:

$$a_g^{(0)}(t) = 1, \qquad a_l^{(0)} = 0 \quad for\ l \neq g \quad (3.19)$$

for all times t. Through use of equations (3.3) and (3.5), V_{mg} can be represented as:

$$V_{mg} = -\mu_{mg}(Ee^{-i\omega t} + E^* e^{i\omega t}) \quad (3.20)$$

where μ_{mg} is given by the relation:

$$\mu_{mg} = \int u_m^*(\vec{r})\hat{\mu} u_g(\vec{r}) d^3 r \quad (3.21)\,.$$

Then equation (3.18) becomes:

$$\frac{da_m^{(1)}(t)}{dt} = -\frac{1}{i\hbar}\mu_{mg}[Ee^{i(\omega_{mg}-\omega)t} + E^* e^{i(\omega_{mg}+\omega)t}] \quad (3.22)$$

which after integration we obtain that:

$$\begin{aligned} a_m^{(1)}(t) &= -\frac{1}{i\hbar}\mu_{mg}\int_0^t [Ee^{i(\omega_{mg}-\omega)t'} + E^* e^{i(\omega_{mg}+\omega)t'}]dt' \\ &= \frac{\mu_{mg}E}{\hbar(\omega_{mg}-\omega)}[e^{i(\omega_{mg}-\omega)t} - 1] + \frac{\mu_{mg}E^*}{\hbar(\omega_{mg}+\omega)}[e^{i(\omega_{mg}+\omega)t} - 1] \end{aligned} \quad (3.23)$$

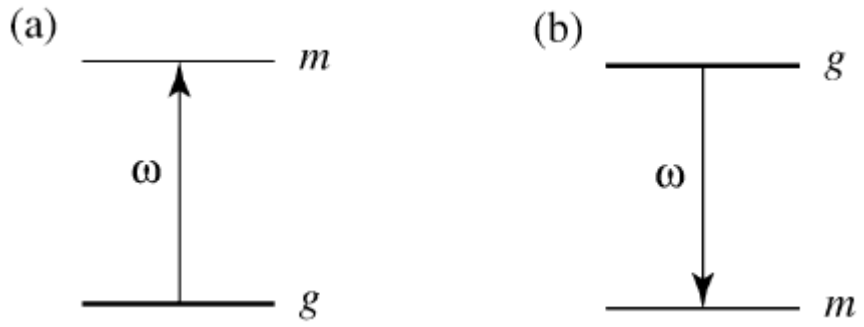

Figure 3.4.: *(a) The first term in Eq. (3.23) describes the process of one-photon absorption, whereas (b) the second term describes the process of stimulated emission.*

The resonance structure of this expression is illustrated schematically in figure 3.4. The first term in expression (3.23) can become resonant for the process of one- photon absorption, and that the second term can become resonant for the process of stimulated emission. As one-photon absorption is examined at present, the second term is dropped from considerations. The neglect of the second term is known as the rotating wave approximation. Since $a_m^{(1)}(t)$ is probability amplitude, the probability $p_m^{(1)}(t)$ that the atom is in state m at time t is given by:

$$p_m^{(1)}(t) = \left|a_m^{(1)}(t)\right|^2 = \frac{\left|\mu_{mg} E\right|^2}{\hbar^2} \left| \frac{e^{i(\omega_{mg}-\omega)t} - 1}{\omega_{mg} - \omega} \right|^2 \quad (3.24)$$

or in an alternative and more convenient trigonometric form:

$$p_m^{(1)}(t) = \frac{\left|\mu_{mg} E\right|^2}{\hbar^2} \cdot \frac{4\sin^2[(\omega_{mg} - \omega)t/2]}{(\omega_{mg} - \omega)^2} = \frac{\left|\mu_{mg} E\right|^2}{\hbar^2} f(t) \quad (3.25)$$

where:

$$f(t) = \frac{4\sin^2[(\omega_{mg} - \omega)t/2]}{(\omega_{mg} - \omega)^2}. \quad (3.26)$$

In order to examine the time dependence of the above expression in case of large values of the interaction time t, for simplicity $f(t)$ is expressed as:

$$f(t) = t^2 \frac{\sin^2 x}{x^2} \quad (3.27)$$

where $x \equiv (\omega_{mg} - \omega)t/2$.

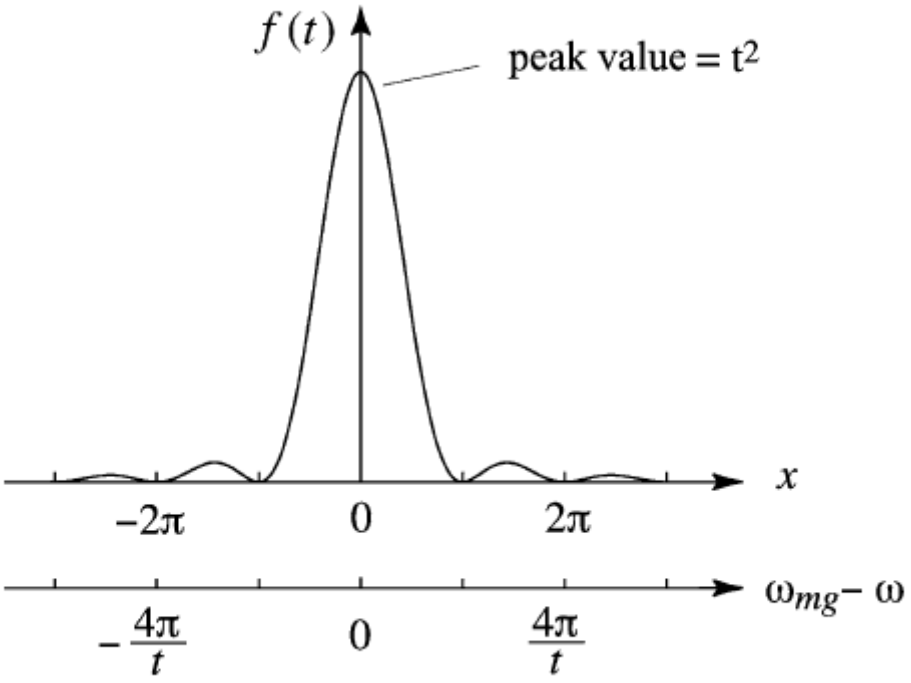

Figure 3.5.*: Plot of f(t) function (3.27) versus the detuning ω_{mg}-ω. It is observed that for very large times, f(t) becomes highly peaked, thus approximating a Dirac delta function.*

Figure 3.5 illustrates for large t, that $f(t)$ is proportional to t times a Dirac delta function and in particular the peak value of the function becomes greater and its width narrower as t increases. In fact, it can be shown that:

$$\lim_{t\to\infty} f(t) = 2\pi t(\omega_{mg} - \omega)\,. \quad (3.28)$$

Thus, for large t the probability to be in the upper level m can be represented as:

$$p_m^{(1)}(t) = \frac{\left|\mu_{mg}E\right|^2 t}{\hbar^2} 2\pi\delta(\omega_{mg} - \omega)\,. \quad (3.29)$$

As it can be seen, the above expression describes an unphysical situation because of the presence of the delta function on the right hand side. In physically realistic situations, the transition frequency ω_{mg} is not perfectly well defined but is spread into a continuous distribution by various line broadening mechanisms such as the natural broadening, the thermal Doppler broadening etc. Usually, this is expressed by saying that the final state m is actually spread into a density of final states $\rho(\omega_{mg})$, which is defined in such a manner so

that the quantity $\rho(\omega_{mg})d\omega_{mg}$ corresponds to the probability that the transition frequency lies between ω_{mg} and $\omega_{mg}+d\omega_{mg}$. The density of states function $\rho(\omega_{mg})$ is normalized so that:

$$\int_0^\infty \rho(\omega_{mg})d\omega_{mg} = 1 \quad (3.30)$$

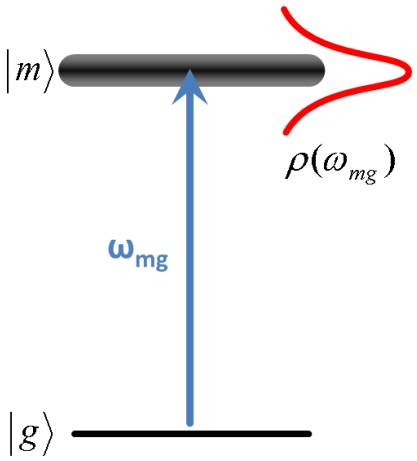

***Figure 3.6**: The state $|m\rangle$ is spread into a density of states described by the function ρ(ω_{mg}).*

Thus, for a transition characterized by a density of final states, the probability $p_m^{(1)}(t)$ to be in the upper level given by (3.29), it must be averaged over all possible values of the transition frequency. Therefore it obtains:

$$\begin{aligned} p_m^{(1)}(t) &= \frac{\left|\mu_{mg}E\right|^2 t}{\hbar^2}\int_0^\infty \rho(\omega_{mg})2\pi\delta(\omega_{mg}-\omega)d\omega_{mg} \\ &= \frac{2\pi\left|\mu_{mg}E\right|^2 t}{\hbar^2}\rho(\omega_{mg}=\omega) \end{aligned} \quad (3.31)$$

where the notation $\rho(\omega_{mg}=\omega)$ means that the density of final states is to be evaluated at the frequency ω of the incident laser light. Since the probability for the atom to be in the upper level is seen to increase linearly with time, a transition rate is defined for linear absorption by the below expression:

$$R_{mg}^{(1)} = \frac{p_m^{(1)}(t)}{t} = \frac{2\pi\left|\mu_{mg}E\right|^2}{\hbar^2}\rho(\omega_{mg}=\omega) \quad (3.32)$$

It has to be noted that equation (3.32) constitutes a special case of Fermi's golden rule.

Another way to express how probable one physical process is, its respective cross section can be calculated. In case of linear absorption cross section is defined as the notional area that the atom had, it would collect the necessary photon energy within the characteristic time $\tau = [R_{mg}^{(1)}]^{-1}$ of the procedure. This definition is derived from the purely classical picture of a large number of point-like projectiles (i.e. photons) directed to an area that includes a solid target (i.e. atom) and where an interaction will occur with 100% the projectile hits the solid, and not at all (0% probability) if it misses.

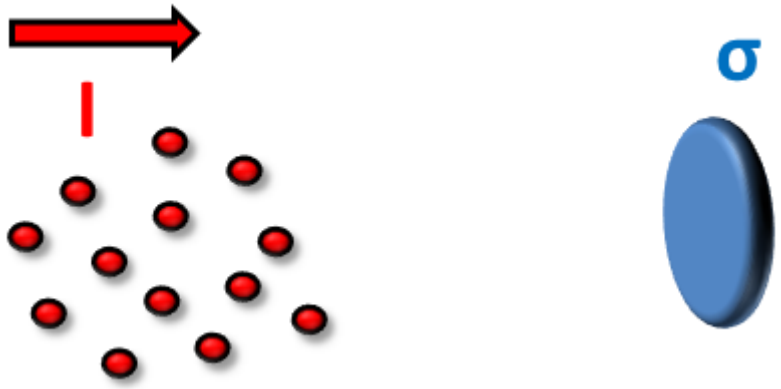

Figure 3.***7:*** *The interaction probability between the point-like projectiles and the solid target is proportional to its respective cross section σ and the intensity I of the incident beam.*

Thus, the cross section $\sigma_{mg}^{(1)}(\omega)$ for the linear absorption is defined as:

$$R_{mg}^{(1)} = \sigma_{mg}^{(1)}(\omega)F \quad (3.33)$$

The F variable represents the photon flux of the incident beam (photons per unit area and unit time) given by:

$$F = \frac{I}{\hbar\omega} \quad (3.34)$$

where I is the intensity of the irradiation, which for our definition of the field amplitude is expressed through the time-averaged Poynting vector as:

$$I = 2n\varepsilon_0 c|E|^2 \quad (3.35)$$

where n is the refractive index of the medium, ε_0 the vacuum permittivity, c the speed of light in vacuum and E the field amplitude. The combination of equations (3.32), (3.33), (3.34) and (3.35) will result in an expression for the cross section of the linear absorption procedure given by:

$$\sigma_{mg}^{(1)}(\omega) = \frac{\pi\omega\left|\mu_{mg}\right|^2 \rho(\omega_{mg} = \omega)}{n\varepsilon_0 c\hbar} \quad .(3.36)$$

In order to examine two photon absorption, which is the simplest case of multiphoton absorption have to solve the set of equation (3.18) for N=1 and N=2, to obtain the probability amplitude $a_n^{(2)}(t)$ for the atom to be in level n at time t. The conventions for labeling the various levels are presented in figure 3.8. The target of this section is to solve equation (3.18) firstly for N=1 to obtain $a_n^{(1)}(t)$, which is then used on the right hand side of equation (3.18) with N=2. As well as V_{nm} expressed as:

$$V_{nm} = -\mu_{nm}(Ee^{-i\omega t} + E^* e^{i\omega t}) \approx \mu_{nm} Ee^{-i\omega t} \quad (3.37)$$

The second term is neglected, because it does not lead to the two-photon absorption.

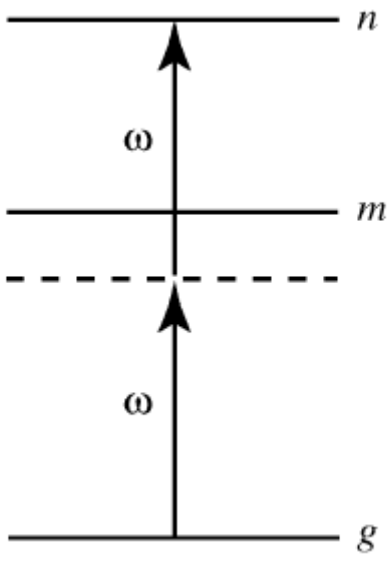

Figure 3.8: *Definition of energy levels used in the calculation of the two-photon transition rate.*

By combining, the equations (3.37) and (3.23) we obtain that:

$$\frac{da_n^{(2)}(t)}{dt} = -\frac{1}{i\hbar}\sum_m \frac{\mu_{nm}\mu_{mg}E^2}{\hbar(\omega_{mg}-\omega)}[e^{i(\omega_{ng}-2\omega)t} - e^{i(\omega_{nm}-\omega)t}] \quad (3.38)$$

by taking into account that $-\omega_{mn} = \omega_{nm}$ and that $\omega_{ng} = \omega_{nm} + \omega_{mg}$. Then the second term is dropped in square brackets, which describes the transient response of the system but does not lead to two-photon absorption. The resulting equation can be integrated directly to obtain:

$$a_n^{(2)}(t) = \sum_m \frac{\mu_{nm}\mu_{mg}E^2}{\hbar^2(\omega_{mg}-\omega)}\left[\frac{e^{i(\omega_{mg}-2\omega)t}-1}{\omega_{ng}-2\omega}\right] \quad (3.39)$$

and the probability to be in level n is given by:

$$p_n^{(2)}(t) = \left|a_n^{(2)}(t)\right|^2 = \left|\sum_m \frac{\mu_{nm}\mu_{mg}E^2}{\hbar^2(\omega_{mg}-\omega)}\right|^2 \left|\frac{e^{i(\omega_{mg}-2\omega)t}-1}{\omega_{ng}-2\omega}\right|^2 . \quad (3.40)$$

For large t, the expression becomes:

$$p_n^{(2)}(t) = \left|a_n^{(2)}(t)\right|^2 = \left|\sum_m \frac{\mu_{nm}\mu_{mg}E^2}{\hbar^2(\omega_{mg}-\omega)}\right|^2 2\pi t\delta(\omega_{ng}-2\omega) \quad (3.41)$$

and if we assume that level n is smeared into a density of states , we obtain that:

$$p_n^{(2)}(t) = \left|\sum_m \frac{\mu_{nm}\mu_{mg}E^2}{\hbar^2(\omega_{mg}-\omega)}\right|^2 2\pi t\rho(\omega_{ng}=2\omega) \quad . (3.42)$$

Thus the transition rate for the two-photon absorption is given by:

$$R_{ng}^{(2)} = \frac{p_n^{(2)}(t)}{t} = \left|\sum_m \frac{\mu_{nm}\mu_{mg}E^2}{\hbar^2(\omega_{mg}-\omega)}\right|^2 2\pi\rho(\omega_{ng}=2\omega) \quad (3.43)$$

However, it is more convenient to express the above equation in terms of a two photon cross section defined by:

$$R_{ng}^{(2)} = \sigma_{ng}^{(2)}(\omega) I^2 \quad (3.44)$$

where $I = 2n\varepsilon_0 c|E|^2$ is the intensity of the incident light beam. Then it is easily to find that:

$$\sigma_{ng}^{(2)}(\omega) = \frac{\omega^2}{4n^2\varepsilon_0^2 c^2}\left|\sum_m \frac{\mu_{nm}\mu_{mg}E^2}{\hbar(\omega_{mg}-\omega)}\right|^2 2\pi\rho(\omega_{ng}=2\omega) \quad (3.45)$$

In order to have a numerical estimation of $\bar{\sigma}^{(2)}$, we assume that a single level dominates the sum in equation (3.45) and that the one photon transition is highly non-resonant so that $\omega_{mg} - \omega \approx \omega$. We also assume that the laser frequency is tuned to the peak of the two photon resonance, so that $\rho(\omega_{ng} = 2\omega) \approx (2\Gamma\pi)^{-1}$, where Γ is the width of level n. Thus, we obtain that:

$$\sigma_{ng}^{(2)}(\omega) \approx \frac{\left|\mu_{nm}\mu_{mg}\right|^2}{n^2\varepsilon_0^2\hbar^2c^2\Gamma} \quad (3.46)$$

Analogously in case of one photon absorption cross section, we calculate that:

$$\sigma_{ng}^{(2)}(\omega) \approx 2.5\times10^{-58}\frac{m^4 s}{photon^2} \quad (3.47)$$

The molecular two photon cross section is usually quoted in the units of Goeppert-Mayer (GM) after its discoverer, Nobel laureate Maria Goeppert-Mayer and where 1 GM is equal to $10^{-50} cm^4 s / photon^2$. Therefore, the numerical value found in corresponds to 2.5 GM, a typical order of magnitude two photon cross section for several fluorophores[8] such as DsRed (11.01 GM at 960 nm), eCFP (7.87 GM at 860 nm) etc . In a comparison to the one photon absorption, we clearly see that the respective two photon cross section values is by several orders of magnitude smaller, a fact which explains the reason why this process is efficiently occurring only when the applied excitation fields are extremely high.

The above results can be generalized to higher order processes. For instance, we can obtain the following set of relations:

One-photon absorption:

$$R_{mg}^{(1)} = \frac{2\pi \left| \mu_{mg} E \right|^2}{\hbar^2} \rho(\omega_{mg} = \omega) \quad (3.48)$$

Two-photon absorption:

$$R_{ng}^{(2)} = \left| \sum_m \frac{\mu_{nm} \mu_{mg} E^2}{\hbar^2 (\omega_{mg} - \omega)} \right|^2 2\pi \rho(\omega_{ng} = 2\omega) \quad (3.49)$$

Three-photon absorption:

$$R_{og}^{(3)} = \left| \sum_{mn} \frac{\mu_{on} \mu_{nm} \mu_{mg} E^3}{\hbar^3 (\omega_{ng} - 2\omega)(\omega_{mg} - \omega)} \right|^2 2\pi \rho(\omega_{og} = 3\omega) \quad (3.50)$$

Four-photon absorption:

$$R_{pg}^{(4)} = \left| \sum_{omn} \frac{\mu_{po} \mu_{on} \mu_{nm} \mu_{mg} E^4}{\hbar^4 (\omega_{og} - 3\omega)(\omega_{ng} - 2\omega)(\omega_{mg} - \omega)} \right|^2 2\pi \rho(\omega_{pg} = 4\omega) \quad (3.51)$$

and so forth [7][13-15].

Chapter 4. Nonlinear Microscopy

The constant evolution of optical microscopy over the past century has been driven by the desire to improve the spatial resolution and image contrast with the goal to achieve a better characterization of smaller specimens. Numerous techniques such as confocal, dark-field, phase-contrast, Brewster angle and polarization microscopies have emerged as improvement of conventional optical microscopy. Being a pure imaging tool, conventional optical microscopy suffers from its low physical and chemical specificity. This can be remedied by combining it with spectroscopic technique like fluorescence, infrared or Raman spectroscopy. Such microscopes have been successfully applied to the study of a wide range of materials with good spectral resolution. However, their spatial resolution is restricted by the diffraction limit imposed by the wavelength of the probe light. In infrared microscopy, for instance, the lateral resolution is a few microns, which is insufficient to resolve sub-micron structures. Conventional microscopy also does not provide microscopic information about the real surface structure of a specimen. Even in reflection geometry, they can only probe the structure of a surface layer averaged over a thickness of a reduced wavelength. Furthermore, they are insensitive to the polar organization of molecules in the layer although this could be important. In biophysics, for example, it is interesting to know the polar orientation of molecules adsorbed on a membrane and its influence on the membrane physiology.

In this context, nonlinear optical measurements that are used in conjunction with microscopy observation have created new opportunities [16-17]. Second-order nonlinear processes such as second harmonic (SH) or sum frequency generation (SFG) are highly surface-specific in media with inversion symmetry and uniquely suited for *in-situ* real-time investigation of surfaces and interfaces [18-20]. With their submonolayer surface sensitivity, SHG and SFG microscopies can be used to characterize inhomogeneities, impurities, formation of domains on surfaces or buried interfaces by mapping out the spatial variation of nonlinear susceptibilities at the interfaces. They are also sensitive to the orientation and distribution of molecules, useful for evaluation of the structure and reactivity of a surface. Third-order processes such as third harmonic generation (THG), coherent anti-Stokes Raman scattering (CARS) and two-photon excited fluorescence (TPEF) microscopies are of interest for the study of buried structures. As the output of second and third- order processes scales respectively, with the square and the cube of the excitation intensity, the focal excitation volume is greatly reduced, enhancing the depth resolution and reducing the out-of-focus background noise. This simple idea has stimulated the development of THG, CARS and TPEF

microscopies in an effort to image buried structures in transparent materials or in biological tissues with a three dimensional sectioning capability. Using ultra-short pulses (10^{-12}–10^{-15} s) CARS has also been demonstrated to be a possible technique to probe the interior of living cells in real time.

Vibrational spectra are known as fingerprints of molecules. Nonlinear optical microspectrometry finds more interest in the mapping of localized domains via vibrational resonances. Microscopy with infrared (IR)–visible (Vis) sum frequency vibrational spectroscopy allows imaging of molecule-specific domains at a surface.

Using a conventional far-field microscope, it can have a spatial resolution one order of magnitude better than Fourier-transform infrared microspectrometry. CARS microscopy also provides vibrational identification of chemical species and is an alternative way to conventional Raman confocal microscopy. Microspectrometry in the electronic transition region is also useful. Multiphoton fluorescence microscopy is becoming a standard technique for biological research. In contrast to one photon-excited fluorescence, multiphoton-excited fluorescence allows the use of input radiation in the transparent region of a sample and is capable of probing the interior structure of the sample with little laser-induced damages.

In this chapter, a number of optical techniques are discussed. Specifically confocal microscopy is firstly described, because it is a common technique in microscopy. Then we proceed to nonlinear techniques such as SFG, CARS, STED, HHG and multiphoton fluorescence microscopies. For each technique, we recall the underlying principle and describe the typical optical setup. Finally, we focus our interest on the two-photon fluorescence excitation microscopy and Higher Harmonics Generation and their main applications [12].

4.1. Confocal Microscopy

Confocal microscopy was developed to remove the out-of-focus light. It is based on the recognition that when an illumination point source (i.e., light emerging from a pinhole) is focused to diffraction limited spot in the sample. This in-focus spot is represented again as a point in the focal plane of an imaging (tube) lens (Figure 4.1A). The illumination and detection pinholes and the in-focus spot in the sample are said to be “con-focal”. A detection pinhole positioned precisely at the focus of the image lens will selectively pass the light collected from the confocal point in the sample, but it will exclude most of the light arising from non-confocal points, both from within the specimen plane and from out-of-focus planes. The diameter of the detection pinhole is chosen to be less than or equal to the central maximum of the diffraction-limited spot, i.e., the size of the Airy disk (and therefore often expressed in ‘Airy units’). Light emerging from points in front of, behind or beside the point of interest at the focus of the objective will not converge at the same spot, and, therefore, only a small fraction of the emitted out-of-focus light will pass through the confocal pinhole (illustrated as dotted and dashed lines in Figure. 4.1.1A). As is done in classical epifluorescence, the fluorescence emission is spectrally separated from the reflected and scattered excitation light. Detection is typically achieved with an ‘area detector (i.e., a detector that is not spatially resolved), such as a photomultiplier tube or avalanche photodiode.

This simple confocal geometry produces the ‘image’ only of a point. One method to obtain a two dimensional (2-D) image is to move the sample relative to the focused spot in the xy plane. For each position, the fluorescence intensity is digitally recorded, and its value assigned to the corresponding xy position on the displayed image. Thus, in contrast to the process in wide-field (camera-based) imaging, in confocal imaging, the image is sequentially constructed from a two-dimensional (2-D) array of point intensities. 3-D image stacks are achieved by additionally moving the objective with a precision motorized focus.

Modern confocal microscopes move the excitation light beam rather than the sample: a laser beam is expanded to fill the objective's back focal plane (BFP) and its angle of incidence in the BFP is scanned with a pair of galvanometric mirrors or other scanning devices.

This arrangement typically requires a high-quality scan lens and the classical tube lens that (nearly) form a telescope. As a result of beam scanning, a diffraction-limited spot sweeps the focal plane (Figure 4.1.1B; for simplicity, only a single mirror is illustrated). The problem is that, to maintain confocality in the detection pathway, the pinhole should be scanned as well. Therefore, the pinhole (and detector) is usually placed behind the pair or scanners so

that the fluorescence that is collected from that spot, traces back the same light path and is 'descanned' before hitting the pinhole. This makes the microscope fairly alignment-sensitive. An interesting recent variant for a confocal microscope based on a nonlinear detection scheme that uses a transmitted pulsed-excitation beam and a virtual pinhole to obtain a confocal transmission image is discussed below [21].

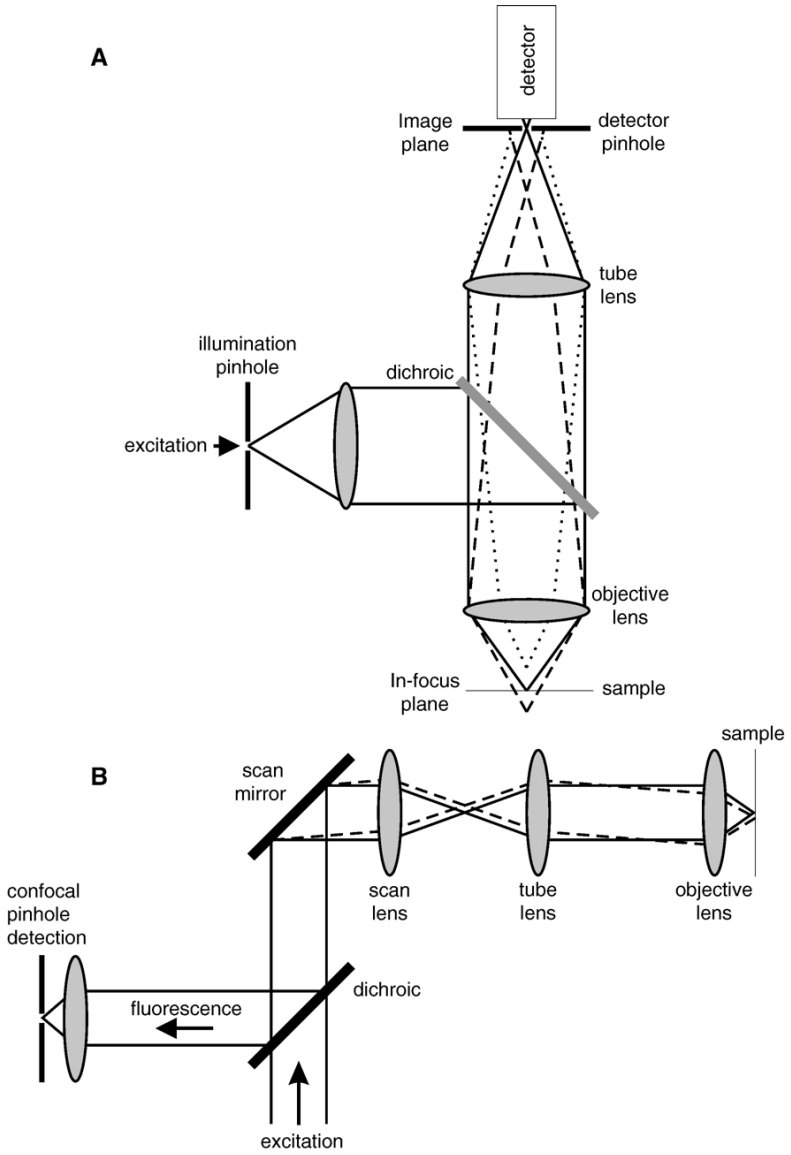

Fig. 4.1.1: *(A) Confocal detection generates crisper images by the suppression of photons from out-of-focus planes by placing a tiny pinhole in front of the detector. However, also fluorescence emanating from peripheral locations of the focal plane are rejected, so that scanning of the sample relative to the beam is required to form a 2-D image. (B) Sketch of the optical elements in a scanning microscope.*

4.2 Sum Frequency Generation Microscopy

4.2.1 Basic Principle of Sum Frequency Generation

A second-order nonlinear optical process, sum frequency generation (SFG) is highly surface-specific in media with inversion symmetry, and can be used as a surface probe. The IR-Vis SFG has already been developed into a powerful surface vibrational spectroscopic technique. In IR-Vis SFG, a visible laser pulse (ω_{Vis}) overlaps with an infrared pulse (ω_{IR}) at a surface and induces a nonlinear polarization $\boldsymbol{P}^{(2)}$ at the sum frequency $\omega_{SF} = \omega_{VIS} + \omega_{IR}$:

$$P^{(2)}(\omega_{SF} = \omega_{VIS} + \omega_{IR}) = \varepsilon_0[\chi^{(2)} : E(\omega_{VIS})E(\omega_{IR}) \quad (4.2.1.1)$$

which radiates and generates the SF output.

Then the SF output in the reflected direction is given by:

$$S\ (\omega_{SF}) \propto \left|\chi^{(2)}_{eff}(\phi)\right|^2 \mathrm{I}(\omega_{VIS})\mathrm{I}(\omega_{IR})\mathrm{AT} \quad (4.2.1.2)$$

with:

$$\chi^{(2)}_{eff}(\phi) = (\overleftrightarrow{L}_{SF} \cdot \hat{e}_{SF})\chi S^{(2)} : (\overleftrightarrow{L}_{\omega_{VIS}} \cdot \hat{e}_{\omega_{VIS}})(\overleftrightarrow{L}_{\omega_{IR}} \cdot \hat{e}_{\omega_{VIS}}) \quad (4.2.1.3)$$

and $\chi^{(2)}_S$ is related to the molecular hyperpolarizability $a^{(2)}$. If ω_{IR} is tuned over vibrational resonances, $a^{(2)}$ must exhibit corresponding resonance enhancement and can be expressed in the form:

$$a^{(2)} = a_{NR} + \sum_q \frac{a_q}{(\omega_{IR} - \omega_q) + i\Gamma_q} \quad (4.2.1.4)$$

where a_{NR} is the non-resonant contribution and a_q , ω_q and Γ_q denote the strength, resonant frequency and damping constant of the q^{th} vibrational mode, respectively.

Correspondingly, we have:

$$\chi_S{}^{(2)} = \chi^{(2)}{}_{NR} + \sum_q \frac{\mathrm{A}_q}{(\omega_{IR} - \omega_q) + i\Gamma_q} \quad (4.2.1.5)$$

If the infrared input is tunable and scans over vibrational resonances, the resonant enhancement of the SF output naturally yields a surface vibrational spectrum. Such spectra with different input/output polarization combinations can yield information about surface composition and structure in a local surface region. This technique has found many applications in many areas of surface science. However, only a few studies combining SFG vibrational spectroscopy and optical microscope techniques have been reported.

4.2.2 Far-Field SFG Microscopy

The combination of SF vibrational spectroscopy with optical microscopy allows detection or mapping of selective molecular species at a surface or interface. It has also the advantage of an improved spatial resolution in comparison to conventional FTIR microscopy because the resolution is now limited by the SF wavelength instead of the IR wavelength. This is similar to Raman microscopy, but the latter is not surface specific. Florsheimer [22] first has extended his development of SH microscopy to SF microscopy. Unfortunately that setup was not possible to be accomplished. Following the pioneering work of Florsheimer, Kuhnke and coworkers have extended SFG microscopy to opaque and reflecting samples [23]. Nevertheless, such microscopy configurations did not allow 3D sectioning imaging because the signal was coming only from the surface.

SFG is however allowed in chiral media through their optical activity. Shen, Yang and coworkers have extended SFG microscopy to image systems containing chiral molecules [24]. In this optically active SFG setup (OA-SFG), the two input beams, polarized in the incidence plane are focused on the sample with the same microscope objective (60x, 1.4 NA oil immersion) and the SF beam polarized perpendicular to the incidence plane, is collected in the transmission direction and detected by a UV-sensitive photomutiplier. (Figure 4.2.2.1)

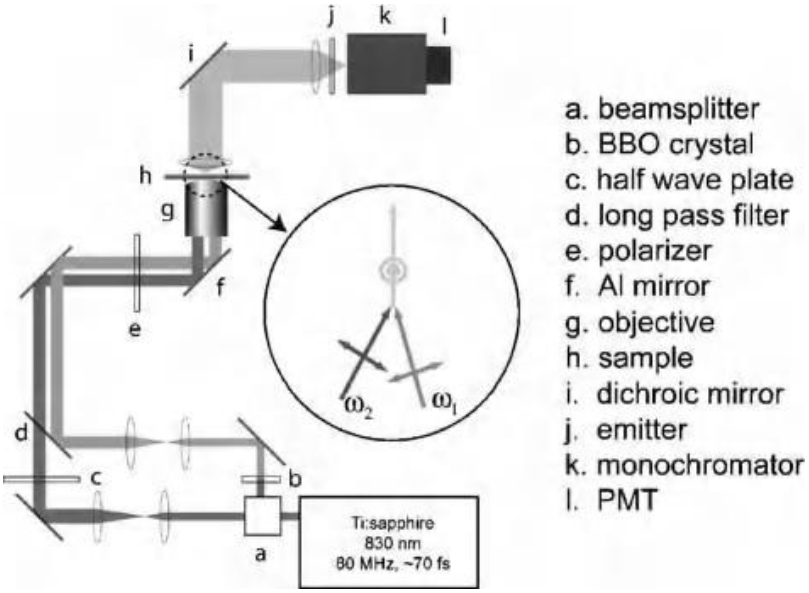

Figure 4.2.2.1: (Scheme of experimental setup. The polarization arrangement for optically active SFG imaging is SPP (for S, P- and P-polarizations of the SF output, 1 and 2 inputs, respectively) in shown is the inset [23].

Chiral molecules, Binol (R/S-(-)- 1,1'-bi-2-naphtol), were used in their experiment. The OA-SFG signal was measured at 277 nm in a band of electronic transitions of Binol. The optical activity of Binol (R/S-(-)- 1,1'-bi-2-naphtol) was evidenced by comparing the SF signals from a racemic mixture and from a pure enantiomer.

The SFG microscopic images of a thin liquid cell containing Binol decorated with silica beads of 2.4 µm diameter are shown in (Fig. 4.2.2.2). The resolution of the images is 400 nm. Since the two beams were focused by the same microscope objective, 3D sectional imaging was possible by raster scanning the sample around the focal region. In addition, this setup permits simultaneous measurements of chiral SHG and SFG from a sample and therefore allows both surface and bulk imaging of the same chiral system. OA-SFG microscopy has the advantage that it is free from achiral background and therefore can exhibit excellent contrast in discriminating chiral molecules from the achiral surrounding. While more research is still needed for applications to biological macromolecules, the technique could emerge as a powerful tool for microscopic imaging of biophysical processes.

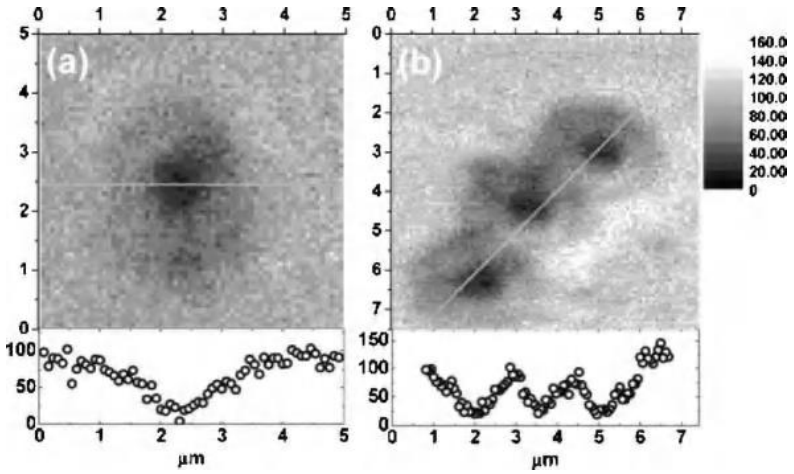

Figure 4.2.2.2.: *(OA-SFG images of (**a** one and (**b**) three 2.4 µm diameter silica beads in R.Binol solutions. Bottom panels show signal variations along the lines in the images. The polarization combination used was SPP and the collection time per image was 78 ms/pixel at power levels of 0.18mW (λ = 415 nm) and 14mW (λ = 830 nm).*

4.3 Coherent Anti-Stokes Raman Scattering Microscopy

Similar to THG, coherent anti-Stokes Raman scattering (CARS) is a third order four-wave mixing process, but is resonantly enhanced at vibrational resonances. In addition it consists a powerful vibrational spectroscopic tool.

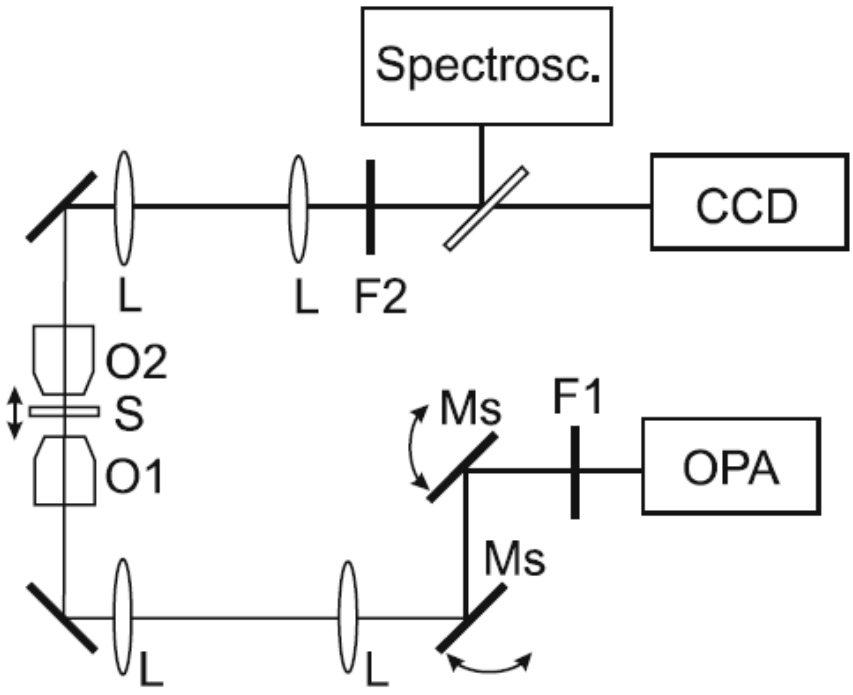

Figure 4.3.1: *Optical setup used by Squier et al. for both writing and reading microdamage patterns in optical glass: OPA: optical parametric amplifier, F1: long pass filter, Ms: scanning mirrors, O1 and O2: objective lenses, F2: blocking filter, M1: insertable mirror [25].*

The process involves two input waves at frequencies ω_P and ω_S with $\omega_P - \omega_S$ tuned to a vibrational resonance of the medium. The two inputs overlap in the medium and induce a third-order nonlinear polarization in the medium at the anti-Stokes frequency $\omega_{AS} = 2\omega_P - \omega_S$:

$$P_{\omega_{AS}}^{(3)} = \varepsilon_0 \chi^{(3)} : E(\omega_P) E(\omega_P) E^*(\omega_S) \quad (4.3.1)$$

which is the radiation source for CARS. Similar to SFG, the nonlinear susceptibility can be written as the sum of a non-resonant and a resonant term:

$$\chi^{(3)} = \chi^{(3)}{}_{NR} + \sum_q \frac{A_q}{(\omega_P - \omega_S) - \omega_q + i\Gamma_q} \quad (4.3.2)$$

Under the plane-wave approximation, the CARS output intensity from a uniform sample of thickness *d* is given by:

$$S\ (\omega_{AS}) \propto \left|\chi^{(3)}_{eff}(\phi)\right|^2 I_P^2 I_S^2 \sin^2(|\Delta k| d/2)/|\Delta k|^2 \quad (4.3.3)$$

where $\Delta k = 2k_P - k_S - k_{AS}$ and:

$$\chi^{(3)}_{eff} = (\overleftrightarrow{L}_{\omega AS} \cdot \hat{e}_{\omega AS})\chi^{(3)} : (\overleftrightarrow{L}_{\omega_1} \cdot \hat{e}_{\omega_1})(\overleftrightarrow{L}_{\omega_2} \cdot \hat{e}_{\omega_{V2}}) \quad (4.3.4)$$

In the case of a strongly focused geometry or a heterogeneous medium, the expression (4.3.3) needs to be modified, but the characteristic's dependence of the CARS output on the phase matching Δ***k*** is still approximately true. For CARS generated in the forward direction (F-CARS), |Δ***k***| is generally much smaller than $1/\lambda_{AS}$. For CARS generated in the backward direction (E-CARS, where E stands for epi-detection), |Δ***k***| is larger than $2\pi/\lambda_{AS}$. From a thin sample, F-CARS and E-CARS, both having |Δ***k***|*d* << π, are expected to have nearly the same signal intensity. From a thick sample with |Δ***k***|*d* < π for F-CARS but |Δ***k***|*d* >> π for E-CARS, F-CARS should have a much stronger output than E-CARS.

Xie and coworkers [26] have studied theoretically the ratio of E-CARS and F-CARS outputs in strongly focusing geometry by varying the sample thickness *d*.

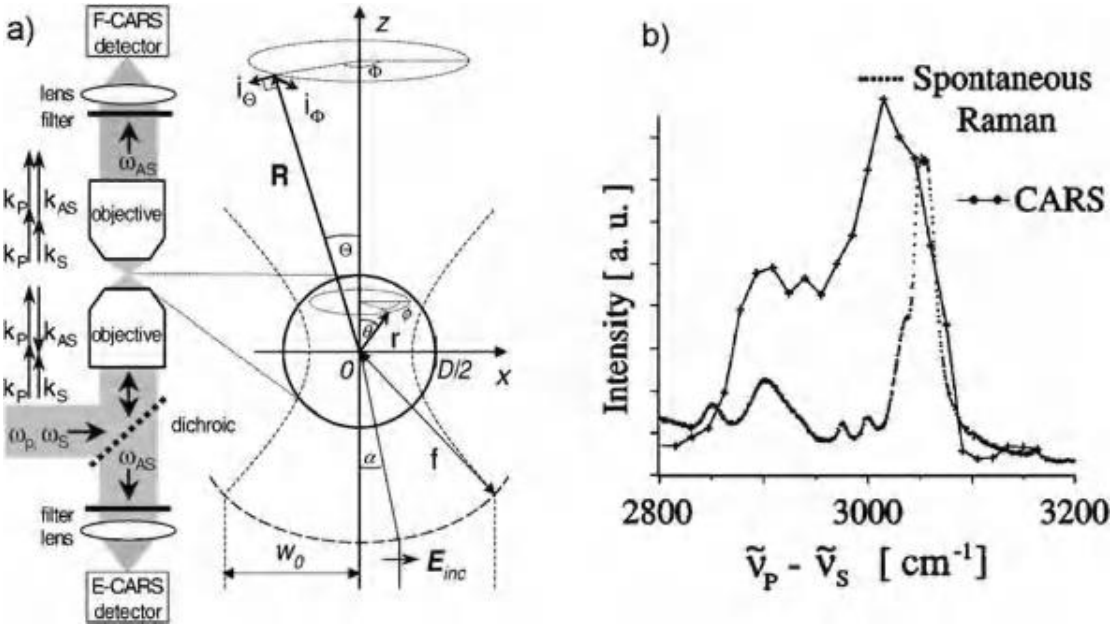

Figure* 4.3.2*: (a) *Optical scheme of the collinear configurations for F- and E-CARS microscopy with collinear pump and Stokes beams and confocal detection in both forward and backward directions. (**b**) CARS and spontaneous Raman spectra of a 910 nm polystyrene bead. For*

CARS, the pump wavelength (v_P) was fixed at 854 nm and the Stokes wavelength (v_S) was tuned from 1.12 to 1.17 µm. The spectral resolution is estimated to 60 cm^{-1}.

They show that the E-CARS output reaches the relative maximum at d = 0.65λ_P. Incorporation of CARS into optical microscopy provides microspectrometric imaging of materials. Duncan and coworkers firstly used CARS microscopy with psec laser pulses to image biological cells soaked in deuterated water. Asides from being able to selectively map out distributions of molecular species via their vibrational resonances, it also has a number of other advantages compared to, in particular, Raman spectroscopy. (1) Since the CARS intensity (4.3.3) is proportional to $I_P^2 I_S$, both the lateral and the axial resolution are $\sim \sqrt{3}$ times better than that of linear optical microscopy. For $\omega_P - \omega_S$ = 3053cm−1 (CH ring stretching mode), a lateral resolution around 300nm and an axial resolution around 1.6 µm (even without a confocal pinhole) have been obtained. (2) A moderate laser intensity and power can be used to avoid damaging of biological samples like living cells. (3) The anti-Stokes emission in CARS is spectrally separable from fluorescence as its wavelength is shorter than λ_P. (4) Transparency of the medium to the input waves allows 3-D microscopy and imaging of buried samples.

Recently, Zumbusch et al. [27] and Volkmer et al.[28] have developed F-CARS and E-CARS microscopy in the 2600 − 3300cm^{-1} region using femtosecond pulses generated by a Ti:sapphire laser and an associated optical parametric oscillator/amplifier). The input beams are focused through a 60× oil-immersion objective with NA=1.4. A similar objective was used to collect the signal in both forward and backward directions. The broad spectral width of femtosecond pulses limits the spectral resolution to ∼60cm^{-1}, as seen in Figure 4.3.3. For better spectral resolution longer input pulses with a narrower spectral width are required.

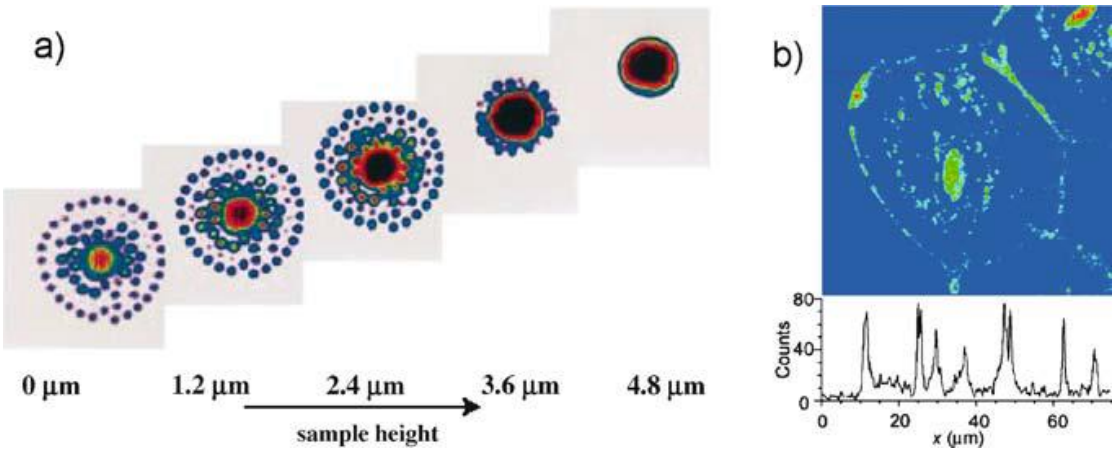

Fig. 4.3.3.: *(**a**) CARS section images (20 × 20 μm^2) of 910 nm polystyrene beads around a 4.3μm bead taken at $\omega_P - \omega_S$ = 3038 cm^{-1}. Sectioning is in the z direction with 1.2 μm increments. The average powers of femtosecond pulses incident on the sample were 120mW and 50mW at 855 nm and 1.155 μm, respectively [29]. (**b**) E-CARS image with a Raman shift of 1570 cm^{-1} of an unstained human epithelial cell in an aqueous environment (size: 75 × 75 μm^2). The average powers of picosecond (f = 100 kHz) Stokes (800 nm) and pump (741 nm) pulses were 1 an 2mW, respectively. The lateral profile of the image displays features as small as 375 nm.*

The 3-D imaging capability of CARS microscopy is shown in Figure 4.3.3a where images of polystyrene beads are presented. The Raman transition probed is the CH ring stretch mode of polystyrene at 3038cm^{-1}. The lateral spatial resolution obtained is around 300 nm. If the sample is immersed in a liquid, the non-resonant background contribution from the solvent can significantly distort the CARS signal [30]. In such a case, since the overall thickness of the solution with the sample is much larger than the input wavelengths, the background contribution in F-CARS is much larger than in ECARS. In fact, because of $|\Delta \boldsymbol{k}| >> 2\pi/\lambda AS$, the background contribution in E-CARS from the solvent is largely suppressed. Figure 4.3.3 b shows an E-CARS image taken at $\omega_P - \omega_S$ = 1570cm^{-1} of a human living cell (75 × 75μm^2 in size) in an aqueous solvent. It clearly exhibits many detailed features. The total imaging time was about 8min.

Following the idea of surface enhanced Raman scattering, Kawata et al. [30] have demonstrated that CARS signal from molecules can be strongly enhanced if the molecules are attached to gold particles and inserted in a CARS microscope. The combination of CARS with an AFM gold tip interacting with samples in the near field region can provide excellent spatial resolution beyond the diffraction limit of light with enhanced signal from the sample. For maximum field enhancement, the tip has to be properly positioned with respect to the focused spot (Figure 4.3.4). The enhanced electric field at the tip apex is strongly polarized along the tip axis and is effective not only to enhance the CARS signal but also to probe molecules oriented along the beam polarization under the tip. The strong local field enhancement makes near-field CARS microscopy possible.

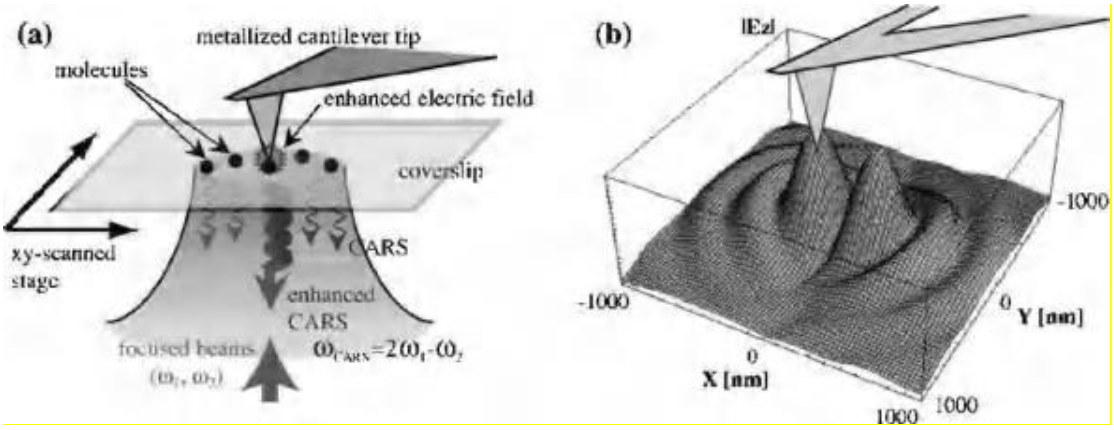

Figure 4.3.4: *(**a**) Schematic of tip enhanced-CARS generated from a gold coated cantilever tip adjusted onto a tightly focussed laser spot by a high NA (1.4) objective lens. (**b**) Calculated z-polarized electric field (along the tip axis) at the tightly focused spot with the excitation wavelength of 800 nm. For the electric field enhancement effect, the tip has to be adjusted onto one of the lobes of the strong z field.*

4.4 Stimulated-Emission-Depletion (STED) Fluorescence Microscopy

The concept of stimulated emission depletion (STED) microscopy was introduced a decade ago by Hell et al. and Schrader et al. STED provides nanometer resolution in a farfield detection geometry. The principle that underlies this variant of nonlinear microscopy is to use two precisely timed and successive light pulses, one to create an excitation volume and the other (the socalled “STED beam”) to pare down the region that fluoresces by illuminating the excited fluorescent molecules with short-lived, donut-shaped depletion beam that drives (depletes) the excited states of the fluorophores to the ground state, sparing only the central donut “hole”. The trick here is to use a depletion beam that is intense around the focal spot, but dark in the center. This can be accomplished by the use of an optical phase plate that produces destructive interference at the center of the focal spot. The only volume left with fluorescent molecules is the hole of the donut.

The excitation beam and the STED beam are of different wavelengths, the former appropriate for excitation, while the latter has the same wavelength as the fluorescence.

Conceptually, STED is based upon an early discovery of Einstein. It had been known for a long time that atoms and molecules could absorb light of one wavelength and then re-emit light of a different wavelength. In 1917, Einstein found that light could also stimulate atoms or molecules to emit light of the same wavelength, polarization and direction of propagation

as the incident light. Stimulated emission forces excited molecules into an upper vibrational level of the ground state, whose ultrafast vibrational decay prevents re-excitation by the same beam.

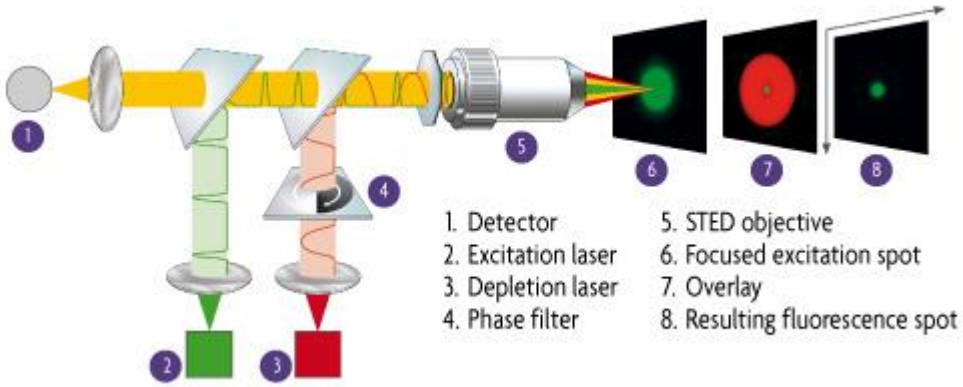

Figure 4.4.1: Diagram of the Leica TCS STED microscopy. *The basis of STED microscopy is the coupling of the excitation laser with the STED depletion laser, resulting in the doughnut-shaped depletion. The two perfectly aligned laser systems minimize the size of the fluorescence spot, overcoming the resolution-limiting effects of diffraction.*

After the STED beam has passed through the focal volume, the majority of molecules not having undergone stimulated emission is still in an excited state and will fluoresce, as the fluorescence lifetime is an order of magnitude longer than the STED pulse duration. Stimulated emission is also the basic process in the laser. For appreciable stimulated emission (i.e., depopulation of the excited state) to occur lasing requires a population inversion, i.e. a more populated excited than ground state, which is achieved by “pumping” the lasing medium electrically or optically.

In as much as resolution in STED images does not depend on diffraction but only on the attainable saturation level, i.e., the STED beam intensity distribution, the focal spot can, in principle, shaped down to a volume of molecular dimensions [31-34].

In practice, STED imaging with a resolution of ~30–40 nm, i.e., ~λ/20 to 25 has been demonstrated. Also, combined with spectral detection of time-resolved fluorescence, STED can circumvent orientational averaging constraints and spontaneous emission selection rules inherent in all conventional techniques. The technique, although still in its infancy, is already producing impressive results, e.g., in the studying the organization of the presynaptic active zone at the nanoscale and will certainly open a view onto the nanoscale world which until now was obscured by diffraction.

STED has been successfully applied to a number of animal cell types and has been pushed to lateral resolutions of below 20 nm [31] [35]. Most excitingly for microbiologists, STED was recently used to image two different protein complexes in mitochondria, demonstrating that the TOM complex forms distinct nanoscale particles [36]. At only 200–500 nm in size, mitochondria are even smaller than most bacteria such that STED should be readily applicable to nearly all microbes of interest. Using four lasers instead of two nanoscale colocalization of two different proteins was recently performed by STED [37], and a variant called IsoSTED enables isotropic super-resolution in all three dimensions [35]. STED has the advantages of being fast (a recent study was able to image synaptic vesicle dynamics at video-rate [35]. Demonstrates the power of rapid STED imaging to follow protein dynamics in living cells.]), suitable for live-cell imaging, unburdened by complicated image processing, and compatible with any type of fluorescent molecule. The disadvantages of STED largely stem from the fact that it works by only imaging the fluorescence of a small fraction of the fluorophores it excites, leading to relatively high rates of bleaching and phototoxicity. The cost and complexity of the multi-laser system have limited STED's widespread appeal, but its recent commercialization should soon reduce the barrier to its implementation.

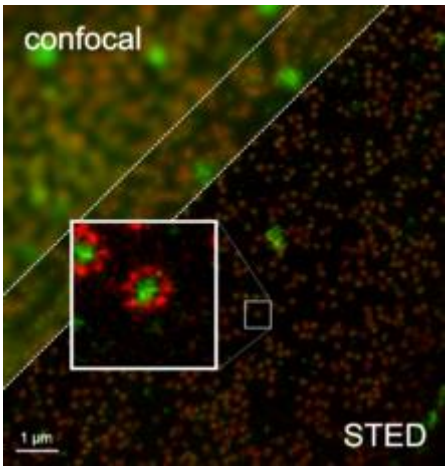

***Figure 4.4.2**: Comparison of confocal microscopy and STED microscopy. This shows the improved resolution of STED microscopy over traditional techniques [36].*

4.5. Multiphoton Excited Fluorescence Microscopy

The invention of two-photon fluorescence light microscopy by Denk, Webb and co-workers revolutionized three-dimensional (3D) in vivo imaging of cells and tissues. In 1931, the theoretical basis of two-photon excitation was established, by Maria Goppert- Mayer, and this photophysical effect was verified experimentally by Kaiser and Garret in 1963. Two-photon excitation is a fluorescence process in which a fluorophore (a molecule that fluoresces) is excited by the simultaneous absorption of two photons (Figure 4.5.1). The familiar one-photon fluorescence process involves exciting a fluorophore from the electronic ground state to an excited state by a single photon. This process typically requires photons in the ultraviolet or blue/green spectral range. However, the same excitation process can be generated by the simultaneous absorption of two less energetic photons (typically in the infrared spectral range) under sufficiently intense laser illumination. This nonlinear process can occur if the sum of the energies of the two photons is greater than the energy gap between the molecule's ground and excited states. Since this process depends on the simultaneous absorption of two infrared photons, the probability of two-photon absorption by a fluorescent molecule is a quadratic function of the excitation radiance. Under sufficiently intense excitation, three-photon and higher photon excitation is also possible and deep UV microscopy based on these processes has been developed [13][40-43].

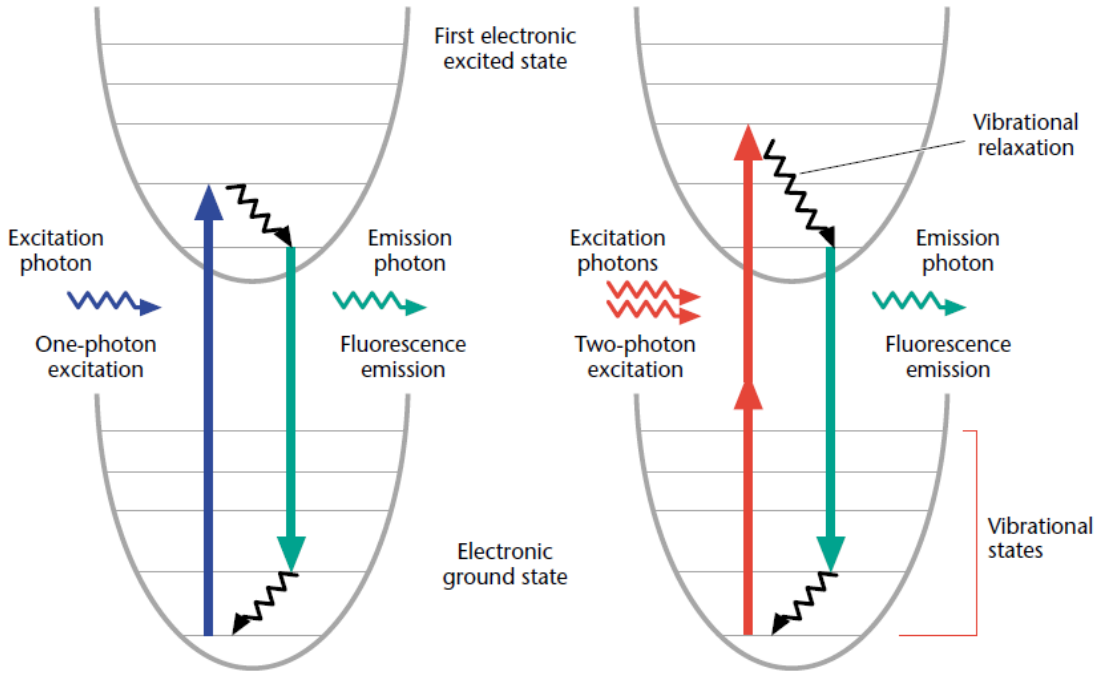

Figure 4.5.1: *Jablonski diagram of one-photon (a) and two-photon (b) excitation, which occurs as fluorophores are excited from the ground state to the first electronic states. One-photon excitation occurs through the absorption of a single photon. Two-photon excitation occurs through the absorption of two lower-energy photons via short-lived intermediate states. After either excitation process, the fluorophore relaxes to the lowest energy level of the first excited electronic states via vibrational processes. The subsequent fluorescence emission process for both relaxation modes is the same.*

Although the possibility of nonlinear excitation was recognized in 1978 (Sheppard and Kompfner, 1978), two-photon microscopy was not demonstrated until 1990 (Denk et al., 1990) [13]. The investigators noted that the two-photon process could be exploited to implement microscopy imaging in three dimensions. Depth discrimination is one of the most important properties of two-photon microscopes equipped with high numerical aperture objectives. For a spatially uniform specimen, fluorescence signals are generated equally from each z-section above and below the focal plane for one-photon excitation. In contrast, over 80% of the total fluorescence signal can be confined to a region 1 µm thick about the focal point using two-photon excitation. This depth discrimination results from the quadratic dependence of the fluorescence probability on the spatial distribution of the excitation radiance. Appreciable two-photon fluorescence occurs only at the microscope focal volume, where the photon density is high; negligible fluorescence is excited outside of this volume (Figure 4.5.2 a, b). A typical TPEF microscope is very similar to the confocal microscope and will be analytically described in the experimental part of this work.

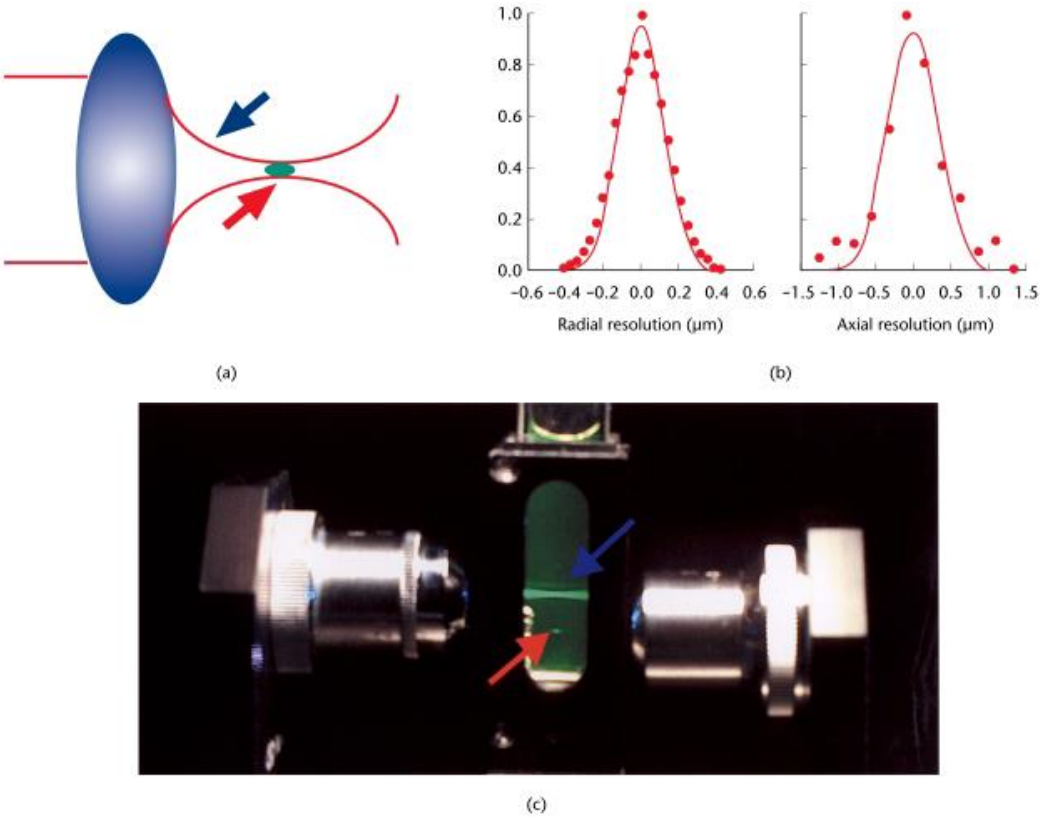

Figure 4.5.2: *A schematic representation of the localization of two-photon excitation. (a) Infrared light (blue arrow) is focused by an objective lens and fluorescence (red arrow) occurs only at the focal volume. (b) A detailed excitation profile of the two-photon excitation volume. The full width at half maximum of the excitation profile is 0.3 μm along the radial direction (left) and is 0.9 μm along the longitudinal direction (right) at a laser wavelength of 960 nm. (c) A demonstration of the localization of two-photon excitation volume. Fluorescein solution is excited by one-photon excitation (blue arrow) via a 0.1 numerical aperture objective; fluorescence excitation is observed throughout the path of the laser beam. For two-photon excitation using a second objective with the same numerical aperture (red arrow), fluorescence excitation occurs only from a 3D localized spot.*

4.5.1 Fluorophores for Two-photon Microscopy

A fluorophore that is one-photon active at wavelength can often be excited by two photons of twice the wavelength (2λ). However, one should recognize that one-photon and two-photon excitation are fundamentally different quantum-mechanical processes and have very different selection rules. A fluorophore's two-photon excitation spectrum scaled to half the wavelength is typically not equivalent to its one-photon excitation spectrum. However, a

fluorophore's emission spectrum, in the absence of ground-state heterogeneity, is independent of the excitation mechanism, since the molecule relaxes to the same excited state through vibrational mechanisms before emission. Since the two-photon spectra of many molecules can be significantly different from their scaled one-photon equivalent, it is important to characterize the spectral properties of common fluorophores under two-photon excitation. The two-photon excitation spectra of over 20 fluorophores have been measured (Xu et al., 1996) [19][43].

4.5.2 Advantages

TPEF microscopy is already widely used for characterization of biological samples [44-57], because of its many advantages compared with other microscopy methods.

Firstly, the two-photon microscopy is particularly suited for imaging in optically thick specimens. Near-infrared radiation that is used in two-photon excitation has orders of magnitude less absorption in biological specimens than UV or blue-green light. The attenuation of excitation light from scattering is also reduced, as the scattering cross-section decreases with increasing wavelength.

Secondly, because of the power dependence on the excitation intensity, the fluorescence originates mainly from the tight focal region. Therefore, sectioning of planes in 3-D imaging is limited only by the focal volume, and a confocal pinhole is often not required to suppress the out-of-focus fluorescence background. This localization of excitation also minimizes photobleaching and photodamage, which are the ultimate limiting factors in imaging living cells. These advantages allow experiments on thick living samples that would not be possible with other imaging techniques. Finally, the recent introduction of commercial two-photon excitation laser-scanning microscope systems allows a much larger group of researcher's access to this state-of-the-art methodology.

TPE is growing tremendously in terms of applications in many areas of biology, physics, medicine, and engineering. Its capability of deep imaging makes it extremely valuable for in vivo imaging. The related technology is still developing rapidly and its range of utilization is broadening.

4.6 Higher Harmonics Generation

Optical higher harmonic generation (HHG), including second harmonic generation (SHG), and third harmonic generation (THG), is known to leave no energy deposition to its interacted matters due to the energy conservation characteristic and the emitted HHG photon energy is the same as the annihilated excitation photon energy [64]. This energy-conservation characteristic releases no energy to its interacted specimens and provides the optical ‘‘noninvasive’’ nature desirable for microscopy applications, especially for clinical imaging [65-68]. Due to its nonlinear nature, the generated SHG intensity depends on square of the incident light intensity, while the generated THG intensity depends on cubic of the incident light intensity (see chapter 2). Similar to multiphoton induced fluorescence processes, these nonlinear dependencies allow localized excitation and provide intrinsic sectioning capability. It is thus important to utilize these endogenous HHG signals (that is sometimes stronger than multi-photon induced autofluorescence) for imaging purpose to replace unnecessary usage of invasive and toxic fluorophores in common multi-photon microscopy.

By using the endogenous HHG sources as the microscopic contrast agents, no fluorescence is required and the common issues of photodamage, phototoxicity, photobleaching, dye availability, or dye toxicity can all be eliminated and therefore this technique can be regarded as a truly ‘‘noninvasive’’ imaging modality.

SHG and THG are both nonlinear processes, related to the interaction of intense light with matters. SHG describes the generation of light waves that are twice the frequency (with half of the original wavelength) of the original waves while THG describes the generation of light waves that triple the frequency (with one-third of the original wavelength) of the original waves. Similar to TPEF, SHG and THG microscopy provides superior axial resolution due to quadratic and cubic dependencies of the signals on the illumination intensity [69].

Usually the third-order nonlinear susceptibility $\chi^{(3)}$ responsible for THG is much weaker than the second-order nonlinear susceptibility $\chi^{(2)}$ responsible for SHG, thus THG is harder to observe. However, not all materials have second-order nonlinear susceptibility. For centrosymmetric media, the lowest order nonlinear susceptibility will be $\chi^{(3)}$ instead of $\chi^{(2)}$. Random distribution of biomolecules and sub-organelles inside tissues and cells create optical centro-symmetry in the optical wavelength (0.4–1 μm) scale, thus inhibiting SHG. SHG is only allowed in non - centrosymmetric media. On the other hand, all materials allow the creation of third-order susceptibility, of which the magnitudes vary according to material properties and wavelengths.

Since SHG does not occur in optically centro-symmetric media, SHG microscopy was first demonstrated for the studies of SHG photonic crystals [69], surfaces/interfaces [70], field distribution in semiconductors [71], and was then applied to biological studies. Biological tissues such as muscles, tendons, skin dermis, and corneas are known strong generators of second harmonic signals [72-74]. SHG microscopy has been demonstrated to be an effective

and minimally invasive imaging tool capable of probing a wide array of issues in biomedical studies including cell-extracellular matrix interaction, in vivo liver metabolism, cancer proliferation, cornea pathology, skin thermal effects, and tissue engineering [72-81]. In addition to morphological information, the excitation polarization dependences of SHG signal can provide structural information below the resolution of optical microscopy [73]. Furthermore, dependence of SHG signal on excitation polarization can be used to differentiate the tissues responsible for generating the second harmonic signals [73, 84-86].

On the other hand, THG is only generated from small inclusions or at the interfaces between materials with different nonlinear coefficients. This makes THG especially suited for biological imaging, since inhomogeneity appears in biological samples on almost any scale.

The phenomena of third harmonic generation (THG) under tight focusing conditions has recently been explored by Tsang [87], who demonstrated that, through the presence of an interface within the focal volume of the excitation beam, third harmonic production is allowed. Normally, tight focusing conditions inhibit the production of the third harmonic [6], requiring a positive wave vector ($\Delta k > 0$) mismatch between the fundamental and harmonic beam to achieve phase-matching. In the case of an interface as considered by Tsang, no such mismatch was required, the resulting breakage in focal volume symmetry enabling efficient generation for $\Delta k = 0$. This can be understood by calculation of the third harmonic power as a function of the interface uniformity as done by Barad et al [86], who show that when there is either a change in refractive index or third-order nonlinear susceptibility, the third harmonic power is non-vanishing. Barad et al [86] demonstrate that as a result of this interface effect imaging with the third harmonic is possible and especially suitable for transparent specimens with low intrinsic contrast, and is sensitive to changes in the specimen's nonlinear optical properties. Squier and Muller had also been exploring the imaging potential of the third harmonic and demonstrated that volumetric imaging was possible using this technique in both biological and non-biological specimens [6, 32].

After that THG microscopy has been tested to date on a variety of biological specimens. Many studies are shown that THG microscopy yields detailed images of multi-cellular and single cell specimens without any prior treatment, and with no observable damage.

Specifically, THG has been used to image red blood cells [88], embryonic development [89][90], neurons [91], skin biopsy samples [92] ,muscle fibers [93], and most recently large intracellular lipid vesicles [94].

4.6.1 Applications

Owing to their similarities and differences , two photon excitation fluorescence(TPEF) , second and third harmonic generation (SHG and THG) imaging microscopy techniques have the potential to provide complementary information about functions and processes of several biological systems in vivo [38]. In this section will be described briefly some applications of this techniques in biological samples and applications of combination of these in a single instrument [44-57].

Multi-photon excitation fluorescence (MPEF), SHG and THG signals can be generated simultaneously from the focal spot of the biological sample providing complementary information. The development of compact, user-friendly, push-button, long term stable femtosecond laser sources, not requiring highly trained laser operators and extreme technical support, facilitates the widespread adoption of non-linear imaging microscopy for biological research. Multi-photon microscopes are now commercially available and it can be is easily upgraded for the detection of additional non-linear signals (SHG, THG). Non-linear microscopes are flexible and easy to use systems. A single femtosecond laser beam is required for the realization of the non-linear measurements (MPEF, SHG, and THG), in contrast to other more complicated label free microscopy techniques such as CARS (two picosecond sources, four wave mixing modality). Therefore, we anticipate that the non-linear optical imaging and especially the THG modality could be extensively used as non-destructive diagnostic tools for the study of complex biological processes in many settings.

First, signaling mechanisms at individual synapses can be monitored in brain slices. The ability of TPE to provide high-resolution images within scattering turbid media has a key role for these studies (Beaurepaire et al. 2001)[61]. Oertner and colleagues (2002) [62] found that the amount of glutamate released per action potential changes during short-term facilitation, suggesting a multivescicular release of glutamate. Moreover, Sabatini et al. (2002) [62] investigated calcium buffering capacity in spines of pyramidal neurons using 2PE. Examples of these applications are given in Figure. 4.6.1, showing a calcium-related image of rat granule cerebrellar cells loaded with Indo-1 acetoxymethyl (AM). The cellular network has been optically sectioned at a moderate average power on the focal plane, 2 mW, at 720 nm excitation wavelength and by focusing with a 100x/1.3 NA objective. The complex and intricate organization in Purkinje cells is shown in Figure 4.6.1 [63].

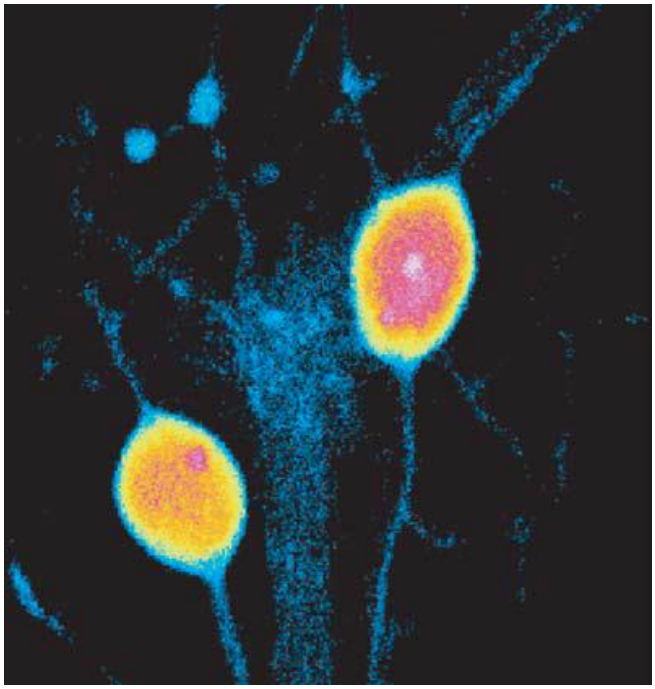

Figure: 4.6.1.: *Granule rat cerebrallar cell loaded with Indo-1 AM, a calcium-binding dye. This UV-excitable fluorescent molecule has been excited at 720 nm at a moderate average power at the focal plane of 2 mW.*

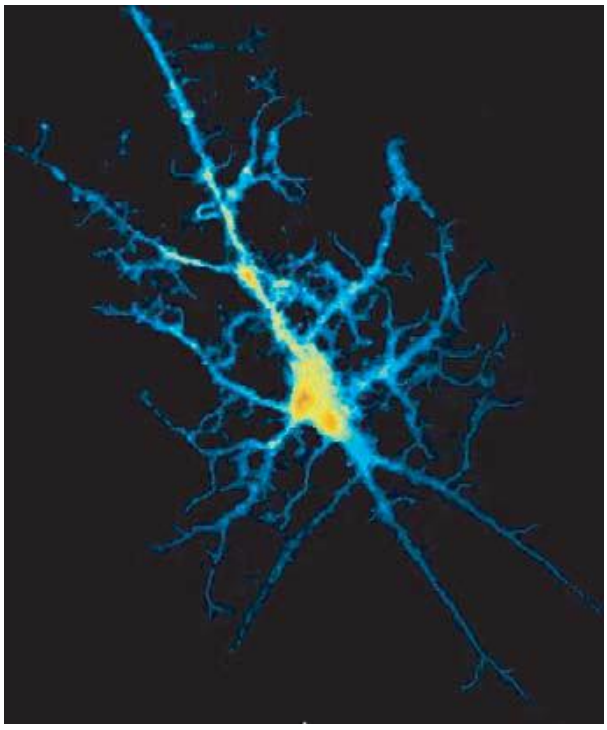

Figure 4.6.2: Purkinje cell labelled with Oregon Green. Calcium ion concentration is mapped by means of a color scale from blue (low concentration level) to red (maximum concentration level).

Moreover TPE in vivo has been used to study the renal excretion of sulfone fluorescein (SF) in normal and cystic rat kidneys. Figure 4.6.3 shows a low power view of the kidney surface of a normal rat infused with SF. SF intensities in proximal tubules are not uniform, but are higher in late proximal tubules than in early proximal tubules. Figure 4.6.3b shows a representative high-power view from a non-pathological kidney. Proximal tubule cell SF fluorescence intensity clearly exceeds that of the plasma and the tubule lumen. This brilliant work by Tanner and colleagues (2003) clearly demonstrates the ability of TPE microscopy to study quantitatively the renal excretion of fluorescent probes in vivo [59].

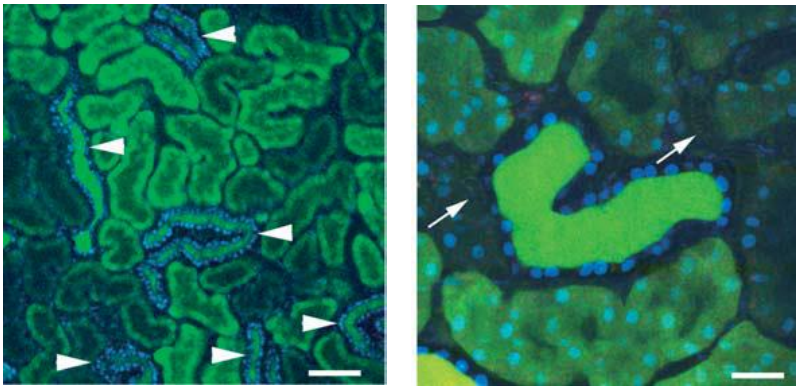

Figure 4.6.3*: Low power (20 X objective) view of the surface of the kidney of an anaesthetized rat kidney during constant intravenous infusion of a solution of sulfone fluorescein (SF). SF is an organic anion secreted by proximal tubules, and it accumulates in proximal tubule cells, especially in late proximal segments. Distal tubules (arrowheads) do not secrete SF (scale=90 µm). (b) Higher power (60 X objective) view of normal kidney. Proximal tubule cell SF fluorescence intensity averages that of peritubullar capillary blood plasma (fine arrows) and is also higher than in the proximal tubule lumen. The distal tubule cells do not take up SF, and their nuclei stain brightly (blue) with the Hoechst dye 33342. SF is concentrated in the distal tubule lumen due to glomerula filtration of SF, secretion by upstream proximal tubule segments, and water reabsorption along the nephron (scale=30 µm).*

Moreover transgenic animals that express GFP under the mec-4 touch-cell specific promoter in two out of the six mechanoreceptor neurons are presented below. The PLM(L/R) touch receptor neurons are located in the posterior part of the worm, close to the tip of the tail, away from the gut autofluorescence. In figure 4.6.4 TPEF signal arising from these neurons are shown. Scanning was performed at a specific z position, where the TPEF signal

emanating from the neuron axon was maximal. The dimensions of the scanned region were 12 x 6 µm. Two different kinds of GFP markers have been used diffuse and oriented GFP. The first one is localized in the cytoplasm of the mechanoreceptor neurons of the animal, when the second is attached to the membrane of the neuron. The absorption and emission maxima for GFP are 489 and 508, respectively. Although the wavelength of this system is not optimal excite GFP molecules (only 20% is absorbed at 514 nm) not only the neuronal cell bodies (2-3 microns) but others anatomical components such as neuronal axons (~200 nm) are detectable [50].

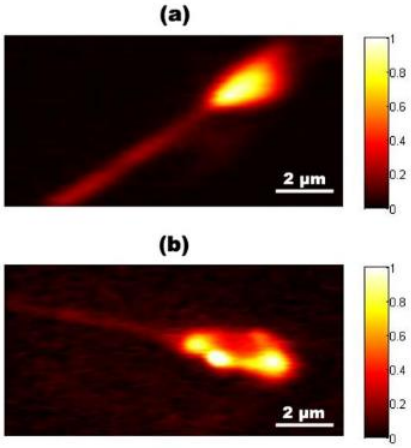

Figure 4.6.4*: TPEF images from mechanosensory neurons of C. elegans marked with (a) diffused GFP (b) oriented GFP [50].*

Moreover, multimodal images can be obtained since SHG and TPEF can be simultaneously generated from a sample by a focused beam and detected in the same microscopy system. Both processes have an output proportional to the square of the input laser intensity, but one is coherent and the other incoherent. If they are pumped by the same laser input, then, as shown in Fig. 4.6.5, both experience the same two-photon resonant excitation. However, SHG is surface-specific in media with inversion symmetry and TPEF is not. Thus the two processes can provide complementary information about the sample. Specifically, Figure 4.6.5 illustrates a color-coded image, which displays SHG signals in cyan originated from type I collagen and antibody fluorescence in yellow revealing that the fibres in the raft (membrane microdomains enriched in cholesterol and glycosphingolipids) correspond to collagen (Zoumi et al. 2002) [60].

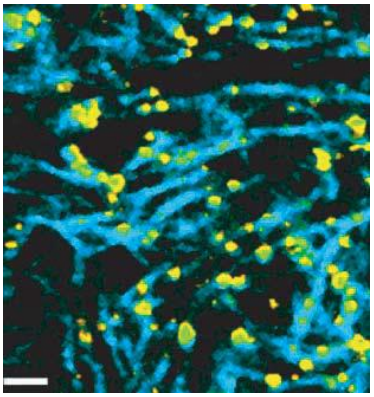

Figure 4.6.5: *Colour-coded image of immunostained collagen fibres in the RAFT. The image is an overlay of two images obtained from the same sample site by using an SBG39 (322–654 nm) wide-pass emission filter and a 520/40 nm bandpass emission filter for 800 nm excitation, and P=60 mW. Collagen fibers are shown in cyan, and the spotted staining pattern of the antibody is shown in yellow (bar, 3 µm).*

Figure 4.6.6 depicts the ability to perform simultaneous THG, SHG and TPEF imaging which allows obtaining complementary information from C elegans samples[90][95].

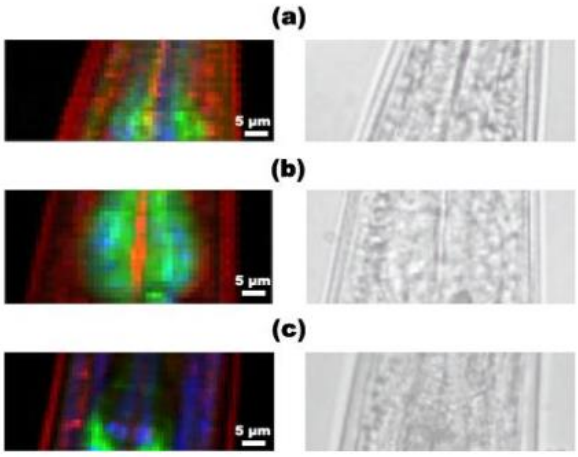

Figure 4.6.6.*: Multimodal image obtained by the combination of TPEF (green), THG (red) and SHG (blue) from C. elegans expressing GFP in the pharynx cytoplasm.*

In this contribution, we have briefly surveyed the field of nonlinear optical microscopy and presented a few examples of contemporary applications. Compared to linear-optics, nonlinear optics has the advantage that it probes a larger domain of material properties. At the time a large number of biophysical processes are under investigation using nonlinear optical processes measured with a microscope. TPEF and THG microscopy used in our lab and in next chapter will be analytically described the experimental setup.

Chapter 5. Experimental apparatus- Biological sample

5.1 Experimental setup

The experimental set-up is outlined in figure 5.1.1. The laser used is an Yb femtosecond t- pulse laser operating at 1028nm. The average power of the laser is 1 Watt, with pulse duration of less than 200fs and a pulse repetition rate of 50MHz. This laser system is employed for the realization of the nonlinear measurements due to the advantage it presents. Its third harmonic signal is in the near ultraviolet (UV) part of the spectrum (~343nm). Consequently, there is no need to use UV optics with special coatings for the collection of the THG signal. Most of the commercial photomultiplier tubes (PMTs) present satisfying quantum efficiency, concerning this wavelength (343nm) resulting in high signal to noise ratio images without the need of high-energy fluencies at the focal plane.

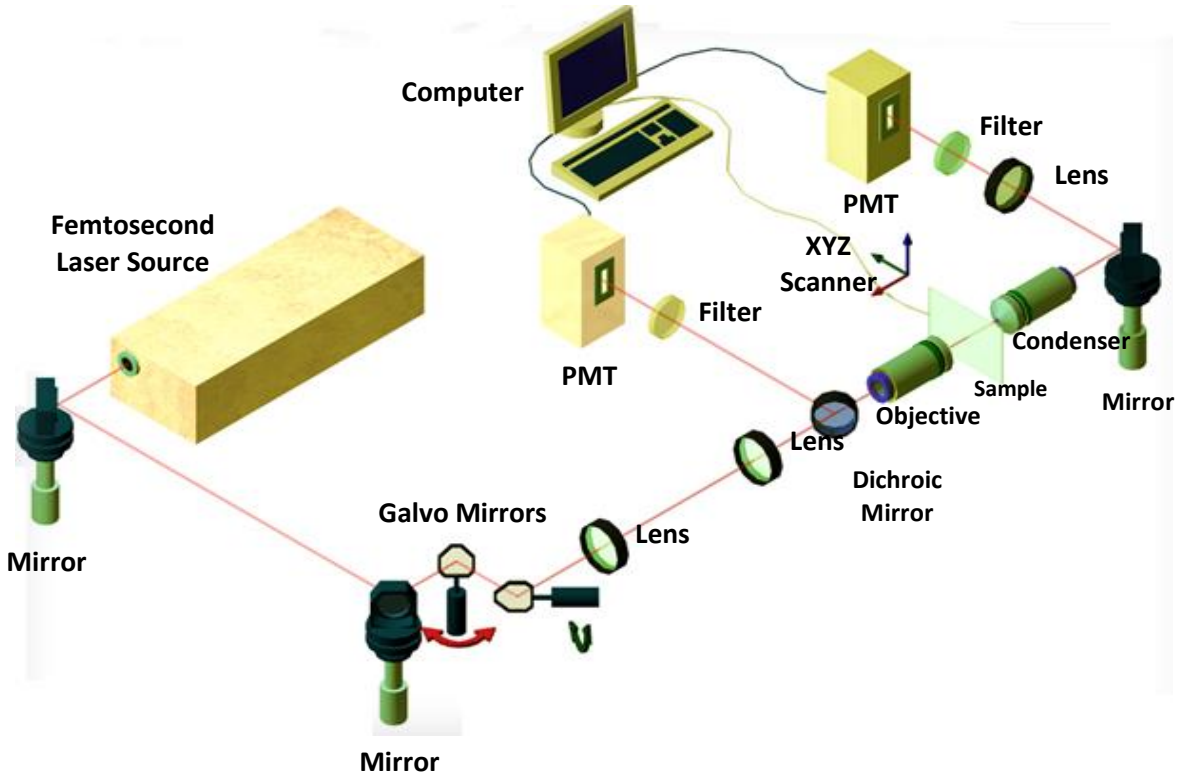

Figure 5.1.1: *Schematic of the experimental apparatus ND filters: Neutral Density filters, PMT: Photomultiplier tube [48].*

Initially, the laser beam is passing through a couple of adjustable neutral density filters. These filters control with precise the power at the sample plane. Subsequently, the

laser beam is guided on a set of galvanometric mirrors (Cambridge Tech. 6210H), which are placed on a modified upright optical microscope (Nikon Eclipse ME600D), in order to scan the biological sample on the X-Y plane. Mirror galvanometer systems are used as beam positioning or beam steering elements in laser scanning systems. The first mirror moves the laser beam in horizontal plane and the second in the vertical plane. By rotating the mirrors it is able to sweep out even arbitrary sections.

A telescope system, which expands the laser beam approximately six times, has been used to fulfil the back aperture of the objective lens. The telescope is consisted of two convergent lenses. The first lens has focus f_1=30mm and the second f_2=175mm. The beam is tightly focused on the sample plane, by using a high numerical aperture objective lens (Carl Zeiss, C-Achroplan 32X, N.A. 0.85, Water immersion, 75% transmission at 1040nm). NA is important because it indicates the resolving power of a lens. The size of the finest detail that can be resolved is proportional to λ/NA, where λ is the wavelength of the light. A lens with a larger numerical aperture would be able to visualize finer details than a lens with a smaller numerical aperture. Assuming quality (diffraction limited) optics, lenses with larger numerical apertures collect more light and will generally provide a brighter image, but this will provide shallower depth of field.

Biological samples were placed between two round glass slides (Marienfeld 0.06-0.08 mm) separated by a spacer of approximately 100μm and were fixed on a XYZ motorized translation stage (Standa 8MT167-100) by using a special holder. The focal plane was selected with the motorized translation stage (1μm resolution).

The induced losses of the emitted THG signals are constrained, due to the thin cover slips, which are used to mount the biological samples. Lab View interface was controlling both the scanning and the data acquisition procedures. A CCD camera (PixeLINK PL A662) was used for observation of the biological specimens. Since different non-linear signals (TPEF, THG) are generated simultaneously at the focal plane, they can be detected via two different detection channels; one in the transmission and another one in the reflection mode. In our configuration TPEF signals were recorded via the reflection mode by using a photomultiplier tube (PMT Hamamatsu R4220). The photomultiplier tube is attached at the position of the microscope eye-piece and connected to the computer.

In case of calibration the photomultiplier tube is connected to a Lock in Amplifier (SR810 Stanford Research Systems). Lock-in amplifiers are used to measure the amplitude and phase of the signals buried in noise. They achieve this by acting as a narrow bandpass filter, which removes much of the unwanted noise while allowing through the signal that is

to be measured. Choppers are often used together with lock-in amplifiers. Optical choppers are used to modulate light beams or particle streams. By modulating the optical beams or particle streams, optical choppers allow these signals to be measured accurately in environments with high ambient noise. Therefore, the use of a Lock in Amplifier provides a very good noise rejection, and measurements can be performed in less stringent lighting conditions. However, Lock in Amplifier wastes a lot of time to measure signals that is why we use it only at calibration progress.Furthermore, a short pass filter (SPF 700 nm, CVI) is placed at the PMT input to cut off the reflected laser light.

The condenser lens (Carl Zeiss, Plan-Apochromat 100X, N.A. 1.4, Oil immersion, 35% transmission at 347nm) has been employed for the collection of THG signal in transmission mode. Condensers are located above the light source and under the sample in an upright microscope, and above the stage and below the light source in an inverted microscope. They act to gather light from the microscope's light source and concentrate it into a cone of light that illuminates the specimen. The condenser lens system should have an N.A. greater than or equal to the largest NA of the objectives. The higher the power, the more important this *condenser lens* becomes.

After passing through a colored glass filter (U 340-Hoya, 80% transmission at 347nm), the THG signals are guided into a second photomultiplier tube (PMT Hamamatsu H9305-04) the respective PMT voltage values are recorded simultaneously from the same computer. By detecting THG images in the forward direction and TPEF images in the backward direction, our experimental apparatus allows the collection of two non-linear optical signals simultaneously. Therefore, the developed set-up provides us the capability of sub-micron processing and nonlinear imaging of biological samples.

Finally, the time needed to record a 2D THG image of 600x600 pixels is less than 800ms. The recording voltage values are proportional to the nonlinear intensity signal stored in a two-dimensional array 600 by 600. Through specifically designed software that values are translated into one of 256 shades of gray ranging black color for the weaker signal intensity to white color for stronger. The result of the translation is a set of two-dimensional 8 bit grayscale images at different depths within the sample. After that we are able to create a "Stack" of these two-dimensional images, by putting them (digitally) the one over the other. Moreover, we have software (Image J) that merges smoothly images in the vertical direction, so that we could eventually receive a 3- dimensional representation of the observed object. The final image can be rotated 360 degrees in the space to see the

observed object under different angles. In order to improve the signal to noise ratio, one 2D optical section is obtained from 30 averaged scans. The total time for obtaining an image is 8 seconds.

5.2 Biological sample

In this study, the biological specimen under investigation was the BV2 microglia cell line. BV2 cells were used to exploit the capacity of combined non-linear optical imaging to provide specific structural and functional information, related to cellular and intracellural processes of our biological model system. The developed nonlinear microscope could be used in a variety of studies in the field of physics, biophysics and medicine. The determination of the intracellural structures such as the mitochondria and/or the lipids of BV2 cell line is the target of the current study. For this reason, a brief discussion of this cell line is necessary.

BV-2 cells are derived from primary mouse microglia cells (Blasi, Barluzzi, Mazzolla, & Bistoni, 1990). BV-2 cells are a useful cell line, because they can be maintained in culture; yet they keep many of the functions and features that microglia express *in vivo* (Henn, Lund, Hedtjarn, Schrattenholz, Porzgen, & Leist, 2009). Culturing these cells means that they must be kept in media, to provide them with the necessary materials they would normally receive in their native environment. BV-2 media contains a red dye to indicate metabolic activity of the cells, fetal bovine serum (nutrition), essential amino acids and antibiotics to help ward off the contamination. [96-98]

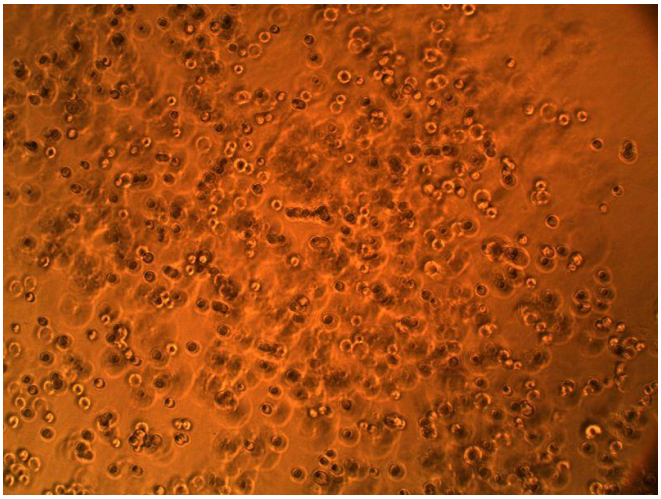

Figure 5.2.1 BV-2 cells in 3D culture (note round morphology) [70]

5.2.1 Microglia

Microglia – the resident immune cells of the CNS – was firstly described in 1919 by del Rio-Hortega (del Rio-Hortega 1919; see Kreutzberg 1996). During the development of the CNS, microglia are important in axonal pruning, as well as for the clearance of debris and

apoptotic cells (Ashwell 1990; Brockhaus *et al.* 1996; Mallat *et al.* 2005). Microglia have a role throughout life in the protection of the immune-privileged CNS against foreign entities, and represent the link between the CNS and the immune system. Like other elements of the CNS, such as neuronal dendrites and astrocyte processes, microglial processes are constantly motile, allowing microglia to monitor the environment and respond accordingly with changes in their morphology and gene expression profile (Davalos *et al.* 2005; Nimmerjahn *et al.* 2005). Microglia may also be mobile within the CNS and able to migrate as a response to tissue damage, or to specific chemoattractants released by CNS or immune cells (Carbonell *et al.* 2005) [98].

5.2.2 Origin

Microglia bear a certain resemblance to the resident cells of the mononuclear phagocyte lineage which exist in other tissues. Indeed, after decades of debate, it is now widely accepted that microglia too are of hematopoietic origin and derive from infiltrating monocytes during early development (Ling and Wong 1993; Kreutzberg 1996). However, unlike other resident monocyte populations, microglia appear to constitute a self-renewing population throughout adulthood, separated from the bone marrow-derived monocyte lineage. The large increase in the local microglial population (microgliosis) following CNS insult was until fairly recently believed to originate at least partly from bone marrow-derived progenitors (Hickey and Kimura 1988; Flugel *et al.* 2001; Djukic *et al.* 2006). However, the latest studies have utilised novel methodology to generate data suggesting that in mouse models of CNS disease and injury, microgliosis is due entirely to proliferation of resident cells (Ajami *et al.* 2007; Mildner *et al.* 2007) [99].

5.2.3 Morphology of microglia

During early postnatal development, monocytes infiltrate the brain and transform into amoeboid microglia, characterized morphologically by their large cell body and short processes (Ling and Wong 1993). This allows them to move within the brain, pruning axons where appropriate and phagocytosing apoptotic cells and other debris associated with CNS development (Ashwell 1990; Brockhaus *et al.* 1996; Mallat *et al.* 2005). Within weeks of their appearance in the CNS, microglia adopt a more ramified, down regulated phenotype (Ling and Wong 1993).

Under normal circumstances, microglia in the adult CNS exist in this branched state. Such ramified microglia were until recently often referred to as "resting" microglia. The recent discovery that microglia are in fact constantly active, monitoring the CNS environment, has prompted a re-evaluation of the role of ramified microglia (Davalos *et al.* 2005; Nimmerjahn *et al.* 2005). At a given moment, individual microglia appear to be responsible for specific portions of brain volume; adjacent microglia are closely opposed, and the boundaries between them may move over time, but their processes mutually repel one another (Nimmerjahn *et al.* 2005). Little is known regarding the true characteristics of ramified microglia *in vivo*, as any manipulation or investigation is likely to activate microglia to some extent (Streit *et al.* 1999).

Microglia adopt an activated phenotype when exposed to substances not usually present in the CNS environment (Kreutzberg 1996). Activated microglia are morphologically similar to the amoeboid microglia present during development (Dheen *et al.* 2007). Microglial activation is also associated with changes in the release profile of microglia and altered receptor expression. Under conditions of neuronal degeneration, microglia may transform into ovoid phagocytic cells, also known as foamy macrophages (Kreutzberg 1996), distinguished by the presence of phagosomes (Streit and Kreutzberg 1988; Rieske *et al.* 1989) [98].

5.2.4 Microglial activation

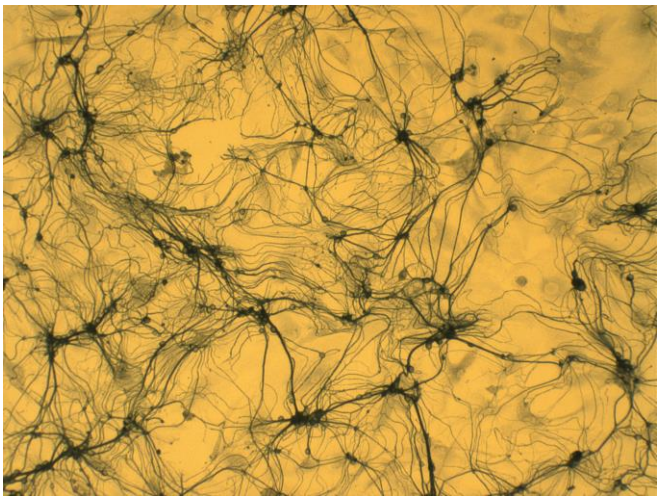

***Figure 5.2.2**: BV2 activated cells*

Microglia may be activated by a whole host of apparently structurally unrelated compounds. Microglia are activated in infectious diseases of the CNS, and pathogens and pathogen components activate microglia *in vitro* (Aloisi 2001). The most commonly used compound to stimulate microglial activation experimentally *in vitro* and *in vivo* is the bacterial endotoxin lipopolysaccharide (LPS), the major mediator of shock induced by gram-negative bacteria (Rietschel *et al.* 1994) [100-101].

As it mentioned the activity of microglia is closely associated with the neural activity, neurodegeneration and infection. Microglia have been implicated in a number of neurological and psychological diseases (e.g., schizophrenia, substance abuse, depression, Alzheimer's disease, Huntington's Chorea, etc.) and they express a large variety and number of neurotransmitter receptors , making them a relevant model for investigating the effects of psychoactive compounds on CNS function [102].

Although microglia activation is often neuroprotective, hyper-activation of these cells can cause neurotoxicity via the release of inflammatory cytokines and chemokines. In addition to secreting chemical signals, microglia, much like systemic macrophages, are phagocytic cells; yet microglia have the unique ability to proliferate as opposed to the terminally differentiated systemic macrophages. These functions give microglia the ability to recognize, engulf, digest and display foreign material and dead cells in the brain as well as the ability to proliferation if the situation requires increased neuroprotection. Unfortunately, microglia activation and proliferation, in response to brain insults, can produce additive or synergistic effects on neurotoxicity through dysregulation of chemical signaling and/or byproducts of the phagocytic process. What is more, brain insults can have direct toxic effects on the microglia, which further compromises the neurons. Therefore, the state of microglia activation (e.g., the number of microglia and their phagocytic activity) is an important indicator of neuropathology and a target for pharmacological manipulation.

5.2.5 Preparation

The biological sample was prepared in Professor's Irene Athanassakis lab by Maria Kalognomou in the Biology Department at the University of Crete. A brief description of the preparation of the biological sample is presented below.

The BV-2 cell line was derived from primary cultures of microglial cells, which were transfected with a retrovirus, who brought the oncogene v-raf/v-myc .

Culture Media:

- DMEM 10% v / v FBS (GIBCO)

DMEM (GIBCO)

Under sterile conditions, we add 5 ml Penicillin / Streptomycin (104 U / ml), 50 ml FBS.

- Culture flasks 25 cm^2 and 75 cm^2
- 6 well plates

- Incubator (Forma Scientific, USA)
- Trypsin / EDTA 0,05%

These cells have the capacity to adhere to the plastic surface of the plate or the flask of which they are developed. The cell culture is at a concentration of $5x10^5$ cells / ml in an incubator Forma Scientific at 37^oC with the presence of 5% CO^2. Medium change occurs every 48-72 hours.

For the detachment of cells we add 2ml or 4 ml Trypsin / EDTA 0,05% to 25 cm^2 culture flasks and 75 cm^2 respectively, and 1 ml for culture in 6well plates. Then, we place the cultivation at 37 °C for 3-5min and after that we add twice the volume of DMEM 10% FBS, in order to stop the action of trypsin. We centrifuge at 1200rpm for 6min, and then we redissolve the cells into new medium, so that we could have the desired concentration of cells in culture.

Cell's Freeze

Materials and solutions:

- Cryovials
- Tubes 15ml
- Pasteur pipettes
- Centrifuge Kubota
- hemocytometer
- Visible light microscope
- Culture medium (DMEM-10% v / v FBS)
- DMSO (Dimethyl-sulphoxide Sigma, Germany)

Experimental procedure:

The cells detached were from the surface on which it was grown with Trypsin / EDTA 0,05% as described above. Then we counted the cells, by using haemocytometer and we dissolved them in the medium, so that the freeze would become a final concentration of 106 cells / ml. To freeze the cells, DMEM 10% v / v FBS, 10% v / v DMSO were used. The addition of DMSO was very gently while stirring and the procedure should be done as quickly as possible, because the DMSO is toxic agent for the cells at room temperature.

The cell suspension was placed in cryovials and stored at -80 ^{o}C.

Defrosting cells

DIALPHA and Materials:

- Tubes 15 ml
- Pasteur pipettes
- water bath
- Centrifuge Kubota
- culture medium (DMEM-10% v / vFBS)
- culture flasks 25 cm2 and 75 cm2
- petri dishes
- Incubator (Forma Scientific, USA)

Experimental procedure:

We, put the cells at 37^{o}C. Immediately after defrost they were diluted 10 times in DMEM-20% v / v FBS. Then the cells were centrifuged at 1200 rpm for 6 min to remove the DMSO, contained in the solution in which it had been freezing. Then they were redissolved in DMEM-20% FBS and we placed them in culture flasks or in 6well plates in the incubator (37^{o}C). The process should be done as quickly as possible because the DMSO is a toxic agent (factor) to the cells at room temperature. The BV2 cell line under the effect of lipopolysaccharide LPS (500ng/ml) was performed under 24 hour cultivation.

We performed a 24 hour culture by using a BV-2 cell line under the effect of the lipopolysaccharide LPS (500ng/ml). In addition, we proceeded in immunofluorescence experiments to identify the Rab7 and the Rab11 surface, which were witnesses of the late and recycling endosomes vesicles, and then we stained with the mitotracker to identify the mitochondria. At the end we used Nile Red dye, in order to identify the lipid particles as described below.

Internal Immunofluorescence

The purpose of the technique was the identification and determination of the expression level of a protein intracellular. In order to study the expression of intracellular proteins (inner immunofluorescence) in the solutions we used saponine, which was a mild detergent that made the cell membrane transiently permeable.

Materials and solutions:

Centrifuge (Kubota)

PBS 1x, pH 7,5

0,2 M phosphate and 1,5 M NaCl

(Initially, the solution was prepared as PBS 10x by dissolving 2, 28 g NaH2PO4 (0,038 M) or 2,62 g NaH_2PO_4 (H_2O) (0,038 M), 11,5 g Na_2HPO_4 (0,162 M) and 43,84 g NaCl in 500 ml dH_2O . Continuously the pH was adjusted to 7.5 and we used it in a final concentration 1x)

- PBS-BSA 3% w/v
- PBS-BSA 1% w/v
- PBS-BSA 3%-saponine 0,3% v/v
- PBS-BSA 1%-saponine 0,3% v/v
- PFA 4% in PBS v/v
- FAC Scan (Becton Dickinson)
- Confocal microscope (Leica)

Experimental procedure:

To conduct the experiment we started with an initial cell concentration of $5x10^5$ cells / sample. The experimental procedure we followed is described below:

1) We rendered the permanent cells by using PFA 4% (100 ml/5x105 cells) incubated for 10 min to 4^oC.

2) For washing the cells we dissolved them in PBS 1x and then we centrifuged them at 1200

rpm for 6 min. Then we repeated the step.

3) We performed blocking by using PBS-BSA 3%-saponine 0.3% and we incubated at room temperature for 30 min.

4) To continue with, we proceed with three washes with PBS 1x.

5) In the cell sediment we added the first antibody, which was diluted in PBS-BSA 1%-saponine 0.3%. We incubated at room temperature for 45 min - 1 h.

6) We followed three washes with PBS 1x.

7) In the cell sediment we added the second antibody, which was diluted in PBS-BSA 1%-saponine 0.3%. We incubated at room temperature for 30-45min in the dark.

8) Then three washes with PBS 1x were following.

9) THG

Staining mitochondria

Experimental procedure:

To start the experiment, we started with an initial cell concentration of $5x10^5$ cells / sample and then we followed the procedure described below:

1) For washing the cells we dissolved them in DMEM 10% FBS , and then we centrifuged them at 1200 rpm for 6 min. Then we repeated by dissolving the cells in PBS 1x, which we had already heat at 37 C.

2) We incubated the cells with Mitotracker, 300nM at 37^oC for 30min

3) Three washes with PBS 1x at 37 C were following.

4) We made the cells permanent, by using PFA 4% (100 ml/5x105 cells) and we incubated them for 10 min at 37^oC.

5) Finally, three washes with PBS 1x at 37 C were following.

Staining of lipid particles

Experimental procedure:

To conduct the experiment we started with an initial cell concentration of $5x10^5$ cells / sample. The procedure we followed is described below:

1) In order to wash the cells, we dissolved them in DMEM 10% FBS, and then we centrifuged

them at 1200 rpm for 6 min. To continue with, we repeated the procedure, by dissolving the cells in PBS 1x

2) We made the cell permanent, by using PFA 4% (100 ml/5x105 cells) and we incubated them for 10 min TO 4oC.

3) Three washes with PBS 1x were following.

4) We, incubated the cells with Nile Red (1:50)

5) Three washes with PBS 1x were following.

Then we cultured for 24 hours a BV-2 cell line, with the presence of the lipopolysaccharide LPS (500ng/ml) by using three different concentrations of serum culture medium. To continue with, we evaluated the results simultaneously, by performing cultures with absence of factor. The conditions that we used are the following:

1) DMEM absence of serum

2) DMEM 10% FBS

3) DMEM 20% FBS

The cells, after passing 24 hours were made permanent, by using PFA 4% (100 ml/5x105 cells) for 10 min at 4^{o}C and then they were observed with THG.

Chapter 6. Colocalization of sub cellular structures in BV-2 cell line by using THG and TPEF imaging microscopy measurements.

The field of nonlinear light microscopy has been rapidly developed, since the appearance of compact femtosecond lasers. The two-photon fluorescence microscopy shows better axial resolution and improved signal-to-background ratios, compared to the standard laser scanning fluorescence microscopy [19].

In THG microscopy, third-harmonic light is generated at the focal point of a tightly focused short-pulse laser beam. When the medium at the focal point is homogeneous, the third-harmonic waves are generated before and after the focal point, interfere destructively, resulting in zero net THG [94][103-105].

However, when there are inhomogeneities near the focal point, such as an interface between two media, the symmetry along the optical axis is broken and a measurable amount of the third harmonic is generated. Due to its nonlinear nature, the third-harmonic light is generated only in close proximity to the focal point. Therefore, high depth resolution can be obtained, allowing THG microscopy to perform optical sectioning and to construct three-dimensional images of transparent samples. Since all materials have non-vanishing third-order susceptibilities, THG microscopy can be utilized as a general-purpose microscopy technique, with no need for fluorescence labeling or staining [58][106].

As it is mentioned before Third-harmonic microscopy is a general-purpose technique and mainly provides structural information. Nevertheless, it cannot give information on specific molecules or organelles. This problem could be solved, by combining third-harmonic imaging with specific fluorescence labeling. Using our suitable experimental setup, it is possible to perform third-harmonic and two-photon excitation fluorescence (TPEF) imaging with a single laser source. Using a single laser source is mostly desirable for the following reasons: firstly, the problem of chromatic aberration does not exist and therefore the third harmonic and the TPEF are generated exactly at the same depth. Secondly, the microscope system and its alignment are mostly simplified, by using only one laser beam and by using two separate collection paths, in the forward direction for the THG and in the backward direction for the TPEF, a single scan is sufficient to provide the combined image.

In this chapter, we firstly use THG microscopy by employing our home made experimental setup in BV2 cells. Then we proceed by using the simultaneous TPEF and THG microscopy

techniques, in order to identify the subcellular structures of BV2 cells that gives high THG signals , by using different dyes.

6.1 THG microscopy

Several studies demonstrate the ability of THG measurements to image various biological samples [6][25][86][93][107-109]. In our study we firstly employed THG imaging for mapping optical heterogeneities inside BV2 cells. In figure 6.1.1, we can notice the evident difference between THG and bright field image of microglia BV2 cells. THG imaging can provide structural images, in contrast to the bright field image that we have very low contrast and low apparent optical resolution of cells. The average laser power on the specimen was almost 30mW (0.5nJ per pulse). This range of THG imaging laser power does not affect the viability of bv2 cells.

The recorded THG image presents high levels of contrast values within each cell, due to the refractive index discontinuities or changes of $\chi^{(3)}$ values of sub-cellular structures. The imaging properties of THG microscopy strongly depend on the field distribution near focus. In THG microscopy, third harmonic light is generated at the focal point of a tightly focused ultrashort-pulsed laser beam. Due to the coherent nature of the THG, no net signal is obtained when focussed inside a homogeneous, normally dispersive medium. This is happening because of the Gouy phase shift experienced by the excitation beam near the focus. However, when the nonlinear medium is not uniform, either in the refractive index or in the nonlinear susceptibility, the THG signal does not vanish, and significant THG output can be obtained. This coherent nature of the THG process renders THG microscopy highly sensitive to inhomogeneities and the efficiency of signal generation strongly depends on the relative size of the inhomogeneity and the focal volume. This specificity makes THG microscopy useful as a tool for material characterization. Results have shown that the magnitude of the THG signal from different specimen geometries strongly depends on the presence of aberrations [105]. Debarre et al. [103] claim that the influence of excitation focusing on the signal depends on sample geometry, allowing one to highlight certain structures within a complex system.

In our work the overall structure of each cell can be identified with satisfactory analysis from the recorded THG signals (figure 6.1.1) .The dark round areas in the central area of each cell represent nucleus, which does not emit any THG signal due to its optical homogeneous constitution. In contrast, moderate to high levels of signals are generated

from the cytoplasm and cell's membrane. The bright spots located within the volume of each cell are either sub-cellular organelles such as mitochondria or lipid droplets [9][94]. Mitochondria and lipid bodies have been considered as the most prominent structures of the THG signal from cells. It could be assumed that they both give information related to the energetic profile of the cell.

Mitochondria and other organelles are effective THG emitters, due to their complex internal structure, which create multiple interfaces and local refractive index differences resulting in the constructive interference of third harmonic waves [110]. Furthermore, lipid droplets present different optical properties and thus different refractive index values in comparison to the surrounding watery environment of the cell. As we can observe in the figure 6.1.1, a THG image gives us a richer amount of structural and morphological information concerning microglia brain cells in contrast of a bright field image. THG presents high contrast among sub-cellular features, such as cell membrane, nucleus and organelles, without the necessity of any staining preparation in contrast of a bright-field image.

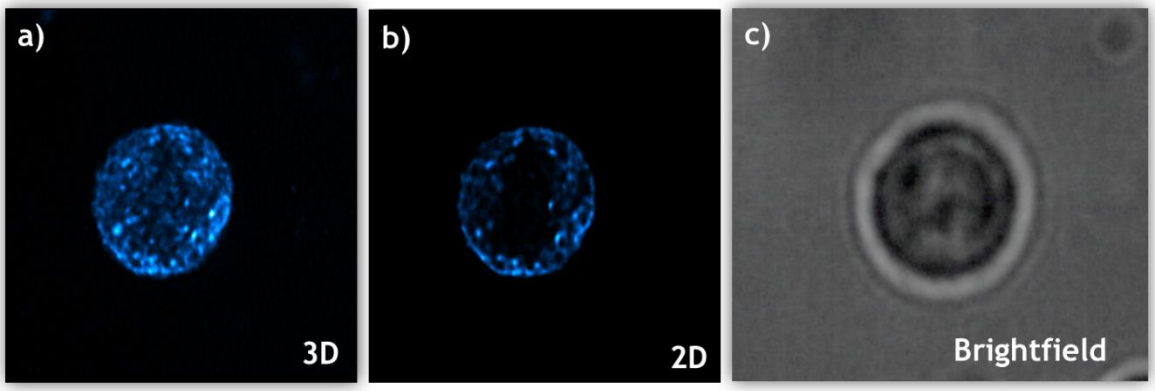

Figure6.1.1: ***a)*** *Three Dimensional (3-D) THG image (500x500pixels),* ***b)*** *Two Dimensional (2-D) THG image (500x500 pixels) in a middle layer,* ***c)*** *Bright field image of BV2 microglia cell.*

6.2 Colocalization

Co-localization of different intracellular structures and simultaneous monitoring of their dynamics is one of several very successful ways to investigate subcellular interactions and functional dynamics inside a cell. Frequently, simultaneous investigations of several structures are accomplished by specifically labeling them with dyes that fluoresce at different wavelengths. Multiphoton Fluorescence (MPF) microscopy is often employed for such studies, where several fluorescence labels can be efficiently excited with spectrally broad femtosecond pulses [13].

Two – photon excited fluorescence (TPEF) permits focal plane specific fluorescence because the only point in the cell/organelle at which the photon intensity is high enough to result in two-photon absorption in the focal point of the laser beam. Thus, the absorbing molecule absorbs two photons virtually simultaneously and as a result behaves as if it has absorbed a single photon at one half the wavelengths of the impinging photons. The result is fluorescence at a wavelength shorter than the excitation wavelength.

Besides, two-photon excitation fluorescence, the nonlinear optical process third harmonic generation (THG) may take place during excitation. Simultaneous detection of third harmonic generation signal together with fluorescence is a very efficient way of imaging and enables direct comparison of structures that are revealed by the different contrast mechanisms. In previous studies, simultaneous MPF and THG was applied to imaging C elegans structures [97], cardiomyocytes [111] and larval spicules [112].

THG signals provide different contrast mechanisms for biological investigations and neither requires staining. The harmonics can be generated at non-resonance conditions i.e. the excitation energy is not deposited into the sample if the excitation wavelength is selected to be outside the absorption bands of the target molecules. The third harmonic can be efficiently generated in a volume containing molecules with high third order non-linear susceptibility or interfaces of materials with different refractive indices [6]. Additionally, multilayer arrangements can enhance THG [103].

In this chapter we describe the imaging of microglia BV2 cell line by the collection of TPEF, and THG simultaneously into separate detection channels, by employing the previously described home-made nonlinear microscope. Micrometer sized intracellular structures appeared as readily detectable bright spots in the THG images. For this reason, in this study

we used different dyes, in order to detect the subcellular structures, which are responsible for high THG signal.

Firstly, we used Mitotracker dye, which stained mitochondria. Next, we used Nile red dye, which stained lipid droplets and in the end we proceeded, by using rab7, which stained the endosomes. This method provides fast data acquisition that enables to perform in vivo dynamic investigations of cellular activity.

6.2.1 Staining Mitochondria

As mentioned above the bright spots located within the volume of each cell are not exactly identified and we know that these structures can be any of the subcellular organelles.

In previous works, it was determined that very strong THG signal is generated in mitochondria, probably due to THG enhancement from the multilayer structures [110-111].

For this reason, BV2 cells were first stained with MitoTracker (specific fluorescent dye for mitochondria), in order to identify if these structures are mitochondria or not that give high THG signals. Specifically, the dye was MitoTracker Red FM, a far red-fluorescent dye (abs/em ~581/644 nm) that stained mitochondria in live cells and its accumulation was dependent upon membrane potential. The spectrum of this dye is indicated in the figure presented below.

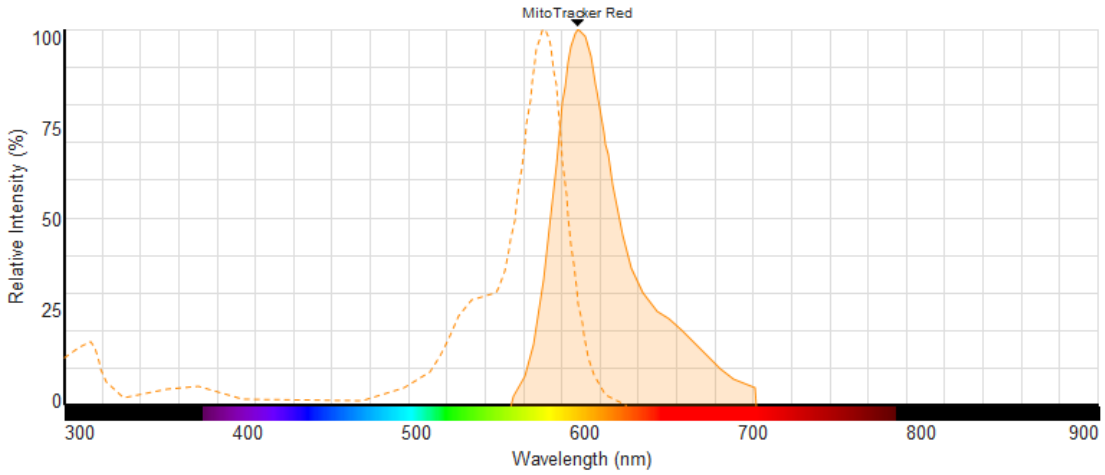

Figure 6.2.1.1: *Absorption and Fluorescence spectra of MitoTracker Red FM fluorophore [118].*

Fluorescence images of BV2 cells with MitoTracker were generated and recorded simultaneously (via TPEF measurements) with THG images. It was shown that co-localization

of the mitochondria specific fluorescent dye with the strong THG emitting structures was poor in both activated and control BV-2 cells (Figure 6.2.1.2,3,4,5).

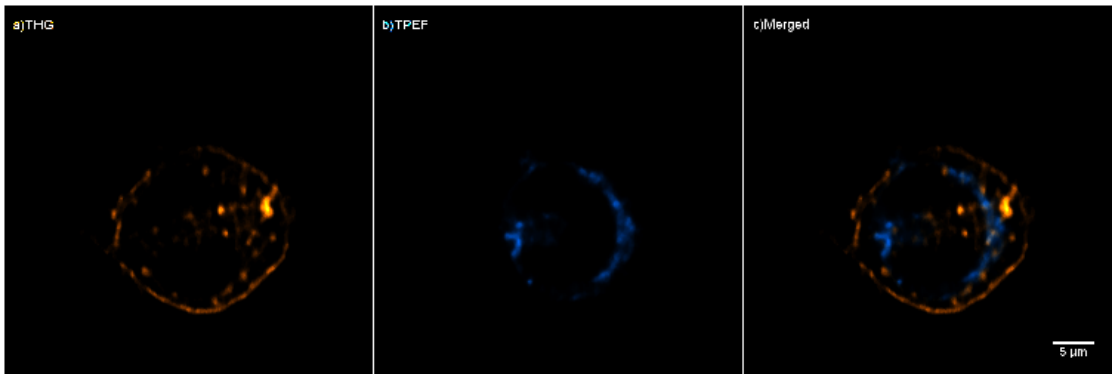

Figure 6.2.1.2: A two dimensional montage of control BV-2 cell stained with mitotracker dye . a) THG image, b) TPEF image ,c) Merged THG and TPEF image.

TPEF

Figure 6.2.1.3 *a) 2-D THG image (500x500 pixels) of a BV-2 control cell stained with MitoTracker b) TPEF of the same BV-2 cell c) multimodal image (THG in yellow, TPEF in blue).*

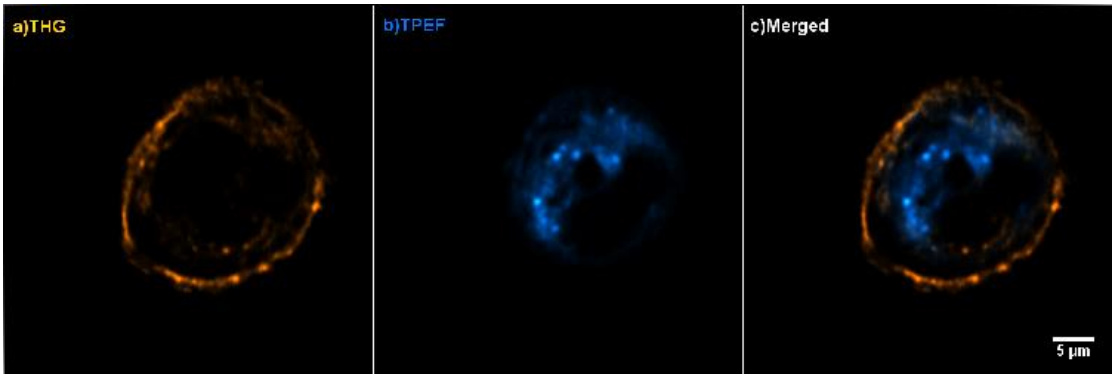

Figure 6.2.1.4: *a) 2-D THG image (500x500 pixels) of a BV-2 activated cell stained with MitoTracker b) TPEF of the same BV-2 cell c) multimodal image (THG in yellow, TPEF in blue).*

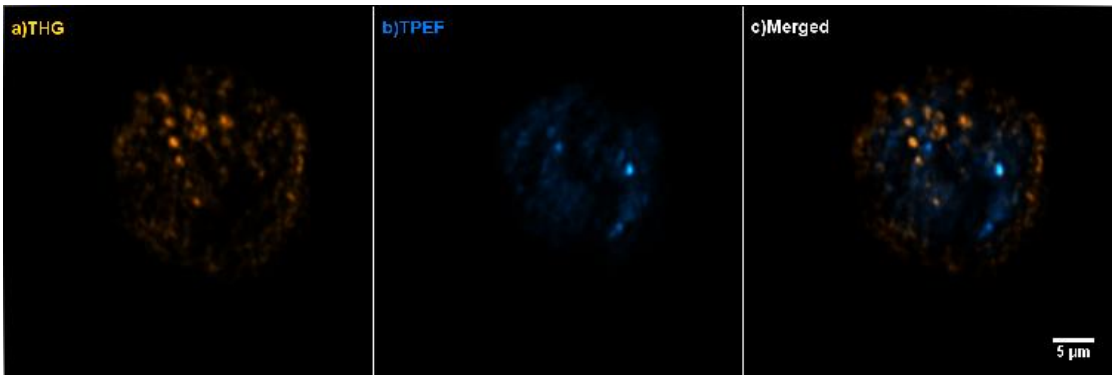

Figure 6.2.1.5: a) 2-D THG image (500x500 pixels) of a BV-2 activated cell stained with MitoTracker b) TPEF of the same BV-2 cell c) multimodal image (THG in yellow, TPEF in blue).

6.2.2 Staining Lipids

Debarre et al. [94][103][108] claim that the micrometer-sized lipid bodies are a major source of contrast in THG images and can be detected with high specificity in a variety of cells and tissues.

Generally, lipid bodies have an important role in energy storage and lipid regulation. Lipid bodies are ubiquitous structures, composed of a neutral lipid core surrounded by phospholipids and associated proteins, and are present in many cells and tissues. Various recent studies [100][103] indicate that these structures are complex and dynamic organelles that interact with numerous cell components. Besides, their role in the digestive track, lipid bodies participate in the physiology of cells and tissues with many different functions.

Consequently, BV-2 cells were stained with Nile red dye both for activated and control cells, in order to identify THG signal for lipid droplets. Specifically, the dye that was used was

Nile red phospholipid, which stains intracellular lipid droplets red, excites in 551 nm and emits in 638 nm. The spectrum is indicated in the figure 6.2.2.1 presented below.

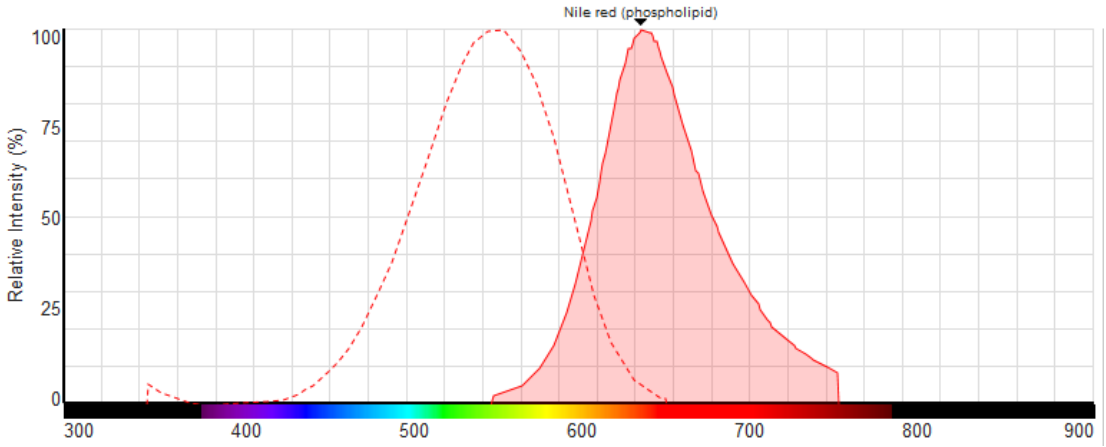

Figure 6.2.2.1: Spectrum of Nile red (phospholipid) dye [118].

Fluorescence images of BV2 cells with Nile red were generated and recorded simultaneously (via TPEF measurements) with THG images. It was shown that co-localization of the lipid droplets of the specific fluorescent dye with the THG emitting structures was strong control BV-2 cells (Figures 6.2.2.1-6).

Specifically, Figure 6.2.2.2 indicates a montage of a 2D control BV-2 cell, on the left is presented a third harmonic generation image, in the middle a two photon excitation fluorescence image of the same cell and on the right there is a merged image of both THG and TPEF images. As we can notice, we have totally co-localized THG and TPEF signal, which means that probably the main part of THG signal comes from lipid droplets.

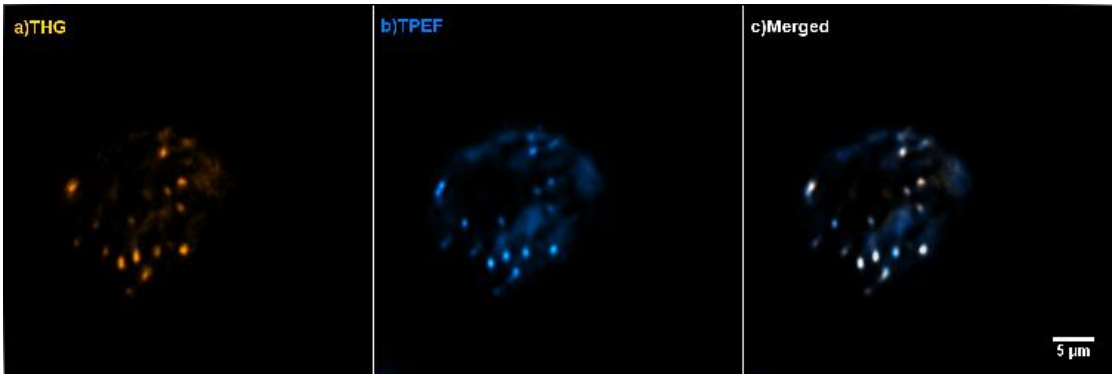

Figure 6.2.2.2: *a)* 2-D THG image (500x500 pixels) of a BV-2 control cell stained with Nile red b) TPEF of the same BV-2 cell c) multimodal image (THG in yellow, TPEF in blue).

Similarly, figure 6.2.2.3 indicates another BV-2 cell stained with Nile red dye. The results here are pretty the same; there is almost totally colocalization of THG and TPEF signals.

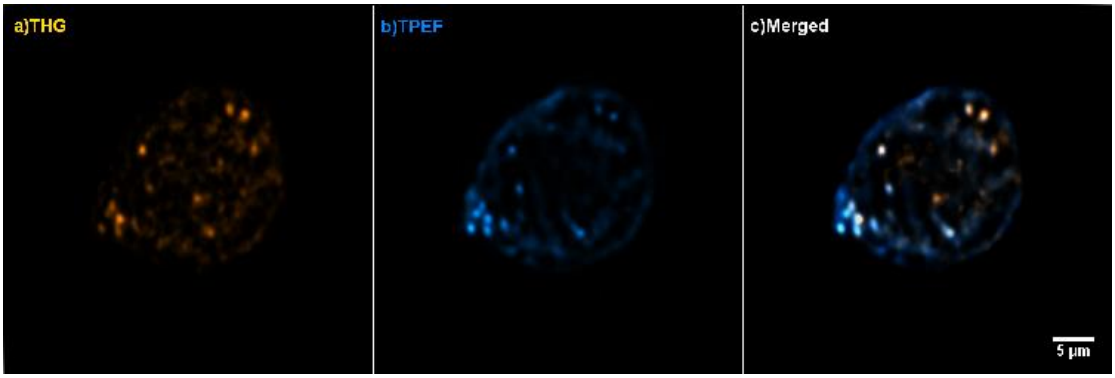

Figure *6.2.2.3:* a) 2-D THG image (500x500 pixels) of a BV-2 control cell stained with Nile red b) TPEF of the same BV-2 cell c) multimodal image (THG in yellow, TPEF in blue).

In the end, Figure 6.2.2.4 shows one more control BV2 cell stained with Nile red dye and the results are also the same – almost total colocalization.

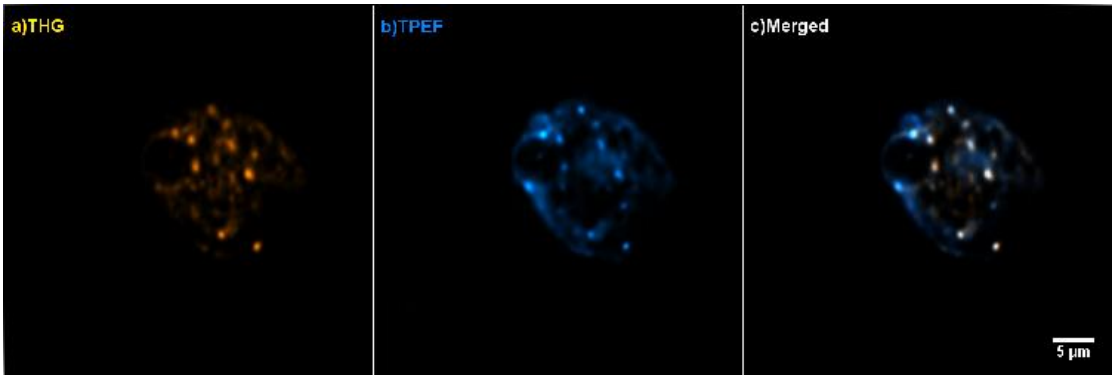

Figure *6.2.2.4:* a) 2-D THG image (500x500 pixels) of a BV-2 control cell stained with Nile red b) TPEF of the same BV-2 cell c) multimodal image (THG in yellow, TPEF in blue).

What is more, activated cells were stained with Nile red dye. As we can observe, the results are almost similar with the control cells. Even in this case, we have almost total colocalization of THG and TPEF signal (Figure 6.2.2.5, 6.2.2.6 and 6.2.2.7).

In case of activated cells, the colocalization is not total, in contrast to the control cells. This is probably due to the activation since the components of lipid droplets changes.

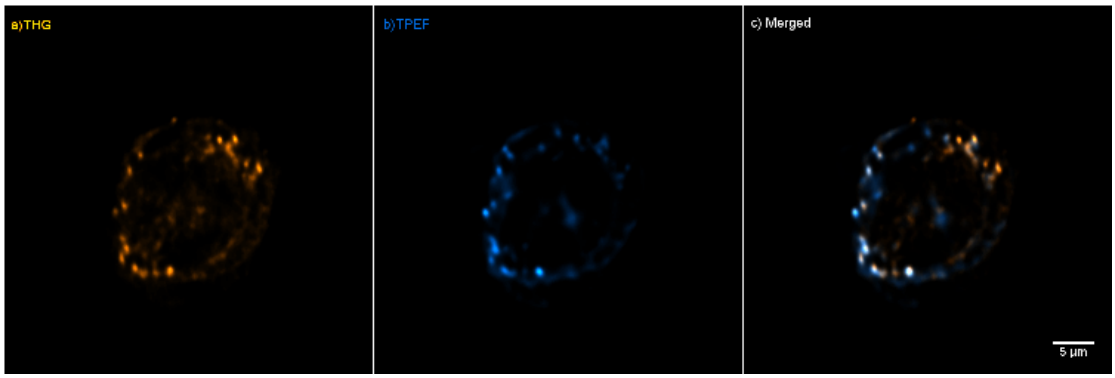

Figure *6.2.2.5:* a) 2-D THG image (500x500 pixels) of a BV-2 activated cell stained with Nile red b) TPEF of the same BV-2 cell c) multimodal image (THG in yellow, TPEF in blue).

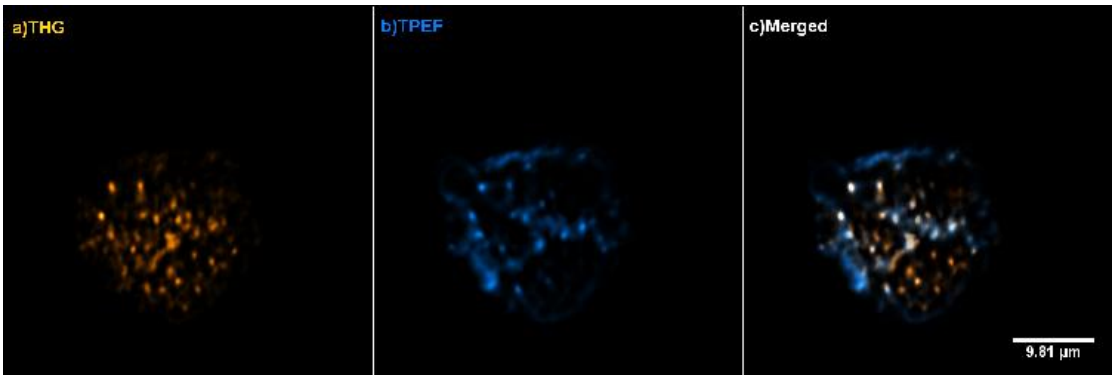

Figure *6.2.2.6:* a) 2-D THG image (500x500 pixels) of a BV-2 activated cell stained with Nile red b) TPEF of the same BV-2 cell c) multimodal image (THG in yellow, TPEF in blue).

As we can notice, figure 6.2.2.7 indicates the cell in the state of division, in this case the cell has three cores (black areas) that does not emit THG signal.

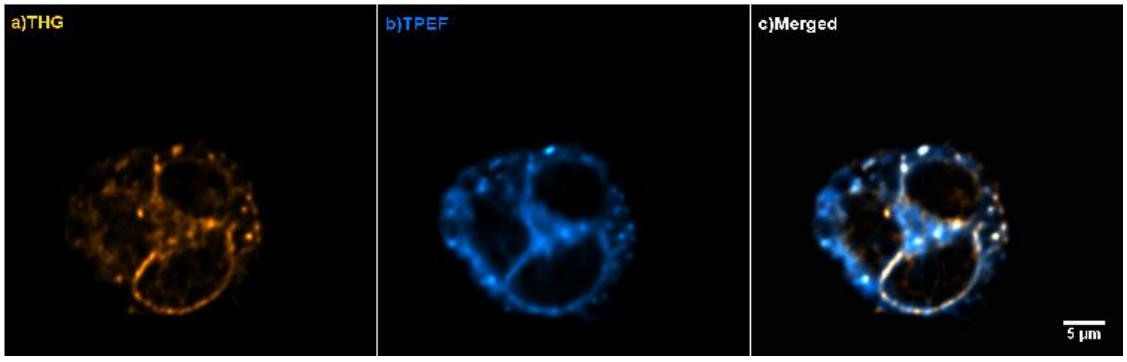

Figure *6.2.2.7:* a) 2-D THG image (500x500 pixels) of a BV-2 activated cell stained with Nile red b) TPEF of the same BV-2 cell c) multimodal image (THG in yellow, TPEF in blue).

6.2.3 Staining endosomes

To continue with, BV-2 cells were stained with a dye, which is localized to late endosomes and is involved in the regulation of membrane transport between late endosomes and lysosomes. Specifically, the dye was anti goat IgG-alexa 488, which excites in 488 and emits in 519 nm. Figure 6.2.3.1 indicated below, shows the spectrum of this dye.

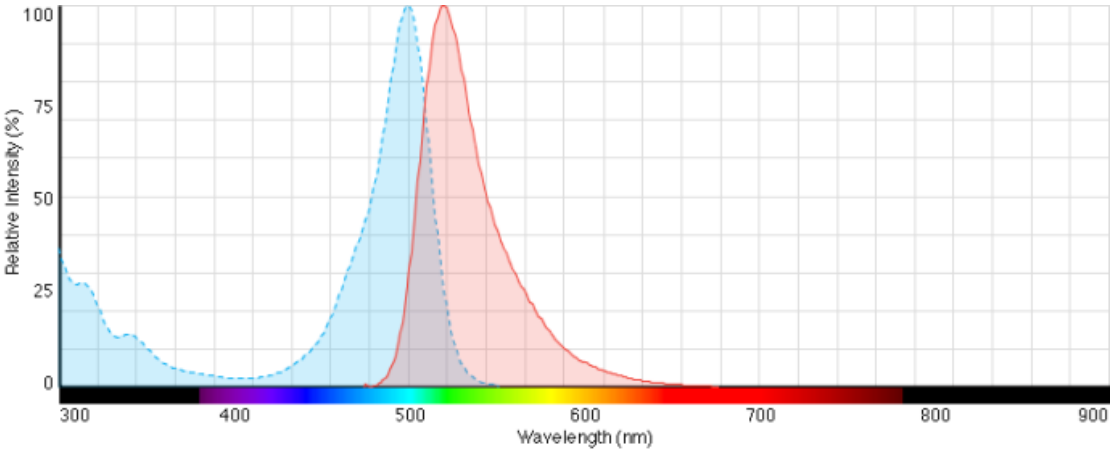

Figure 6.2.3.1: Spectrum of anti-goat IgG-alexa 488 [118].

An endosome is a membrane-bounded compartment inside eukaryotic cells. It is a compartment of the endocytic membrane transport pathway from the plasma membrane to the lysosome. Moreover, it represents a major sorting compartment of the endomembrane system in cells. Endosomes are approximately 500 nm in diameter when fully mature .

The primary responsibility of endosomes is to separate proteins that will recycle to other cellular locales from those that will be degraded in lysosomes. In this way, endosomes regulate the composition of the cell surface and thus play a pivotal role in a vast array of biological functions. Maturation from early to late endosomes entails the removal of both proteins and lipids via tubulo-vesicular elements that sort components back to the trans Golgi network and plasma membrane. Integral membrane proteins that have not been recycled, as well as soluble lumenal materials, are instead delivered to late endosomes and lysosomes (Gruenberg & Maxfield 1995) [113-15].

In this case of dye the colocalization of the late endosomes specific fluorescent dye with the THG emitting structures was poor (Figure 6.2.3.2, 3, 4).

We have to mention that these result images were only for activated cells, as this dye probably does not express the control cells.

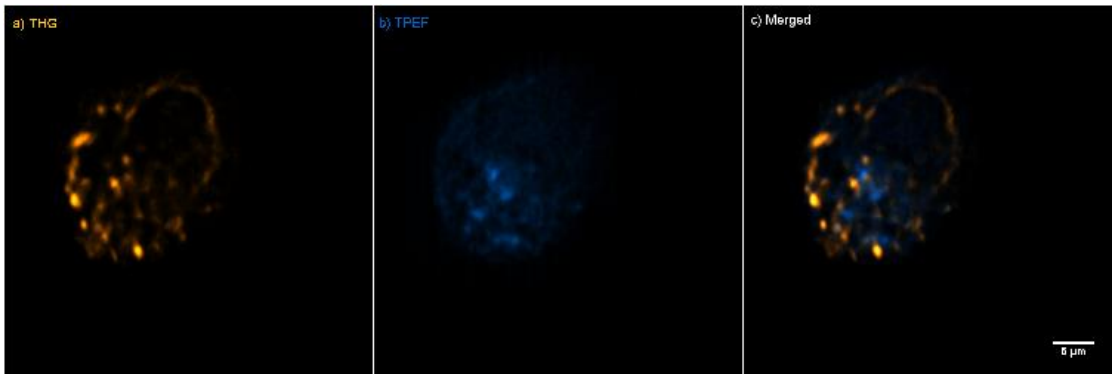

Figure 6.2.3.2: *a) 2-D THG image (500x500 pixels) of a BV-2 activated cell stained with Rab 7 b) TPEF of the same BV-2 cell c) multimodal image (THG in yellow, TPEF in blue).*

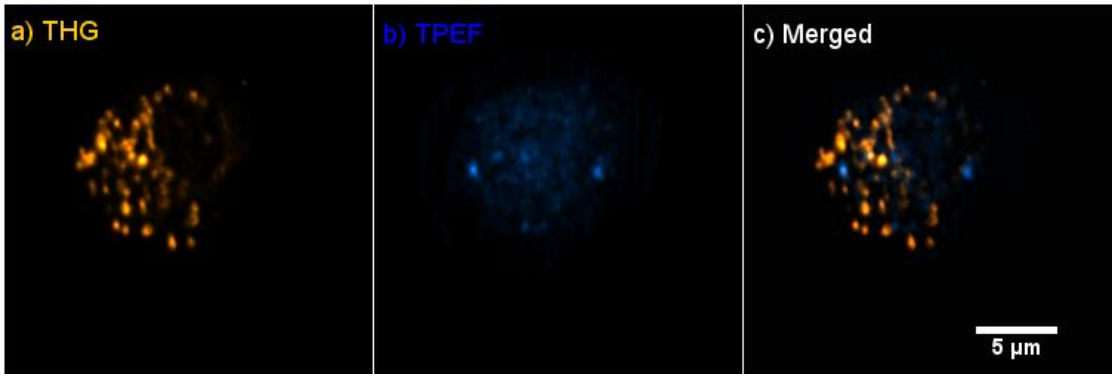

Figure *6.2.3.3:* a) 2-D THG image (500x500 pixels) of a BV-2 activated cell stained with Rab7 b) TPEF of the same BV-2 cell c) multimodal image (THG in yellow, TPEF in blue).

Figure 6.2.3.4, indicates another BV-2 activated cell, stained with Rab7. Nevertheless, the form of the structures is different. As we can observe in the middle fluorescent image, the structures are compact. This is called a multivesicular endosome (or multivesicular body MVB). Multivesicular endosomes (MVEs) are complex intracellular organelles that function in endocytosis. A major function of the endocytic pathway is to sort internalized macromolecules and membrane proteins.

MVBs referred as a form of late endosome, specifically referred to as the transport of intermediate between early and late endosomes-an intermediate also known as an endosomal carrier vesicle (ECV) [116][117]. Indeed, all endosomes along the degradation

pathway contain multi vesicular elements, including regions of early endosomes (that correspond to newly forming ECV/MVBs) and late endosomes.

In fact, multi-vesicular elements of late endosomes contain a complex system of internal membranes that are involved in both the degradation and recycling of proteins and lipids.

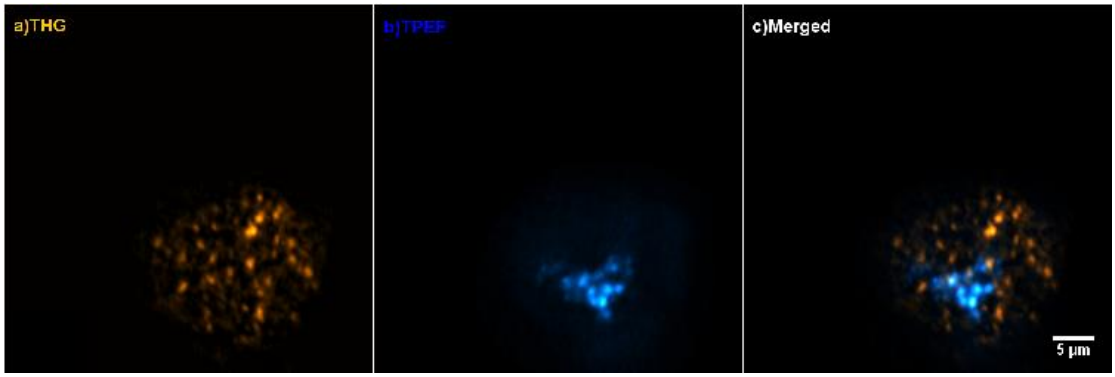

Figure *6.2.3.5:* a) 2-D THG image (500x500 pixels) of a BV-2 activated cell stained with Rab7 b) TPEF of the same BV-2 cell c) multimodal image (THG in yellow, TPEF in blue).

At the end, the cells were stained with the same antibody as before, in order to express the recycling endosomes, which had the marker Rab11. *Recycling endosomes* are concentrated at the microtubule organizing center and consist of a mainly tubular network. Unfortunately, the results have shown that that this dye was not expressed in BV-2 cells.

The co-localization of the mitochondria and of the endosomes specific dyes respectively with the THG emitting structures was poor. In contrast, the colocalization of lipid droplets specific dye with the THG emitting structures was almost absolute in case of control cells. Thus, we can claim that the main sub-cellular structures of BV2 control cells that give high THG signals may be the lipid droplets, because as mentioned above, they are one of the prominent structures of THG signal. Hence, our data established that lipid bodies could be specifically detected in unstained control cells and tissues using THG microscopy. On the other hand, the colocalization of lipid droplets in activated cells was not absolute; probably there are important structural changes of the component of lipids after the activation.

Chapter 7. Quantification of BV2 cells

Nonlinear optical microscopy can provide important information about the subcellular structures, without the use of fluorophores or other markers. The present study describes how the non-invasive THG imaging techniques may provide important information in case of BV-2 cell line. As we mentioned in chapter 5, BV-2 cells present different treatment at activation, which is closely associated with the neural activity, neurodegeneration and infection. The changes of activation of BV-2 cells are mainly associated with the increase of lipid droplets. For this reason, we employed the THG microscopy tool. Lipid metabolism is of particular interest, due to its high concentration in CNS. The importance of lipids in cell signaling and tissue physiology is demonstrated by many CNS disorders and injuries that involve deregulated metabolism. Specifically, we accomplished quantification of THG signal in both mean total area and intensity of the subcellular structures.

7.1 Process of quantification

7.1.1 Mean's Total area

THG signal quantification is different for mean total area and intensity. Following such a procedure, it became possible to quantify the THG profile of each situation of the cell (control – activated).

The signal provided by the THG imaging is based on the optical properties differences within the cellular compartments, where lipid bodies have been considered as the most prominent structures for the THG signal.

In case of mean's total area quantification, the values are in the form of 8 bit image that are translated into one of 256 shades of gray ranging black color for the weaker signal intensity to white color for stronger . This 8 bit image is put into the program Image J. Image J offers the capability to improve the image by using a couple of orders (smooth, noise, filter – unsharp mask). Next, we set a threshold (about 30 of 255), which allows almost 15% of THG signal. The threshold is selected in the way that the unwanted THG signal (noise) is going to be reduced, in order to let only the subcellular structures (probably the lipids).

Figure 7.1.1 indicates how the cell seems to be before and after applying the threshold, in case of mean total area. The first two up pictures are three-dimensional and two-dimensional respectively THG images of the same cell. The two bottom images represent the same cells after applying the threshold.

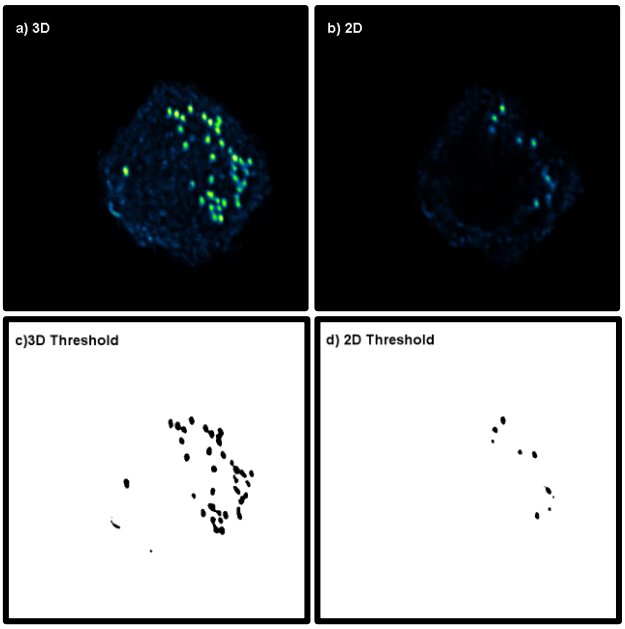

Figure 7.1.1: a) Three Dimensional (3D) BV-2 cell, b) Two Dimensional of central slice of the same BV-2 cell, c) The three dimensional cell after applied threshold 35, d) The 2D cell above intensity threshold 35.

To continue with, the Image J program can analyze the particles of the cell for each layer and give a number of pixels for each particle; these data can be saved in an Excel file. To be precise, the Image J was used for the representative area selection of the cell A_i (number of pixels) of each slice. Then, these data are inserted in a Matlab script that calculates the mean total area of each cell and moreover gives extra information about the total number of particles, the total area, and the mean area value, the standard deviation of areas, the CV, the skewness and the kyrtosis.

Then, the values of mean total area of each cell were added in SPSS program. This program is a software package used for statistical analysis. In our case, we use this program, in order to make statistically comparison of mean total area between control and activated (lps) cells. Specifically, we compare means by using an independent t samples t-test (equal variances not assumed) on the natural logarithms of pixel values.The independent-samples t-test (or independent t-test, for short) compare the means between two unrelated groups on the same continuous, dependent variable.

7.1.2 Mean THG values

However, the process of intensity's quantification is different than the one of the total area. In this case need to estimate the mean pixel value $\bar{x}_i$ and standard deviation $\bar{s}_i$. This procedure was repeated for all the k slices that constituted each cell. The weighted mean pixel value $\bar{x}$ of each cell was calculated then by the quantity:

$$\bar{x} = \frac{\sum_{i=1}^{k} A_i x_i}{\sum_{i=1}^{k} A_i} \quad (7.1.2.1)$$

and the pooled standard deviation s_p by:

$$s_p = \sqrt{\frac{\sum_{i=1}^{k} ((A_i - 1)s_i^2)}{\sum_{i=1}^{k} (A_i - 1)}} \quad (7.1.2.2)$$

The quantification of THG signal produces a numerical value of the subcellular structures content for each cell.

Thus, as described above, normalized matrices for each cell were used to generate 32-bit grayscale images, while the Image J was used for the selection of the representative cell's area, and as well as the mean pixel value and the standard deviation calculations of each slice. After that a couple of Matlab scripts used to translate the images into intensity values. In this program we set a threshold 22 that reduces the unwanted THG signal as indicated in the figures 7.1.2 -7.1.3 below.

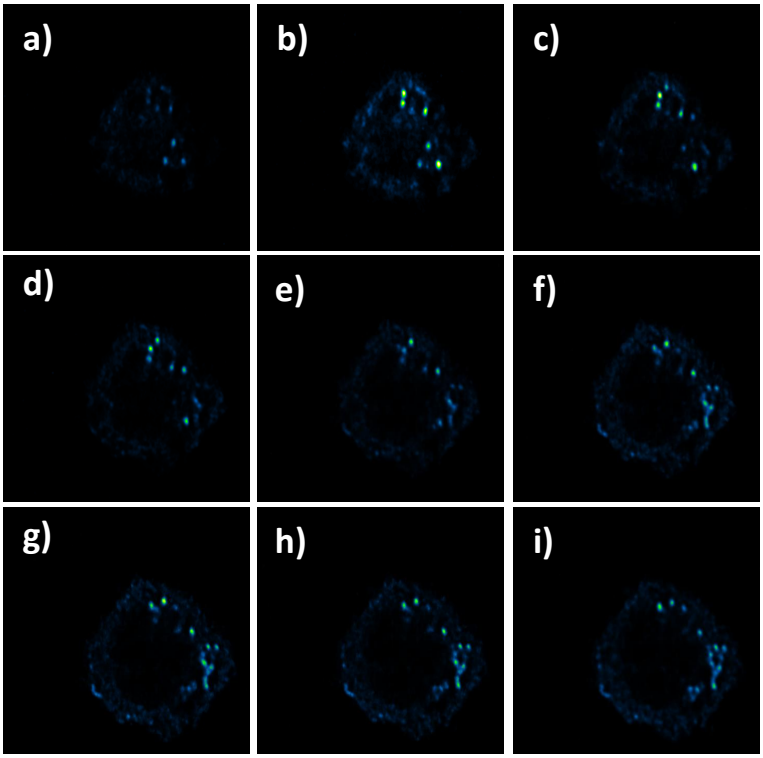

Figure7.1.2: *For the process of Intensity's quantification put in Matlab program central slices of BV-2 cell*

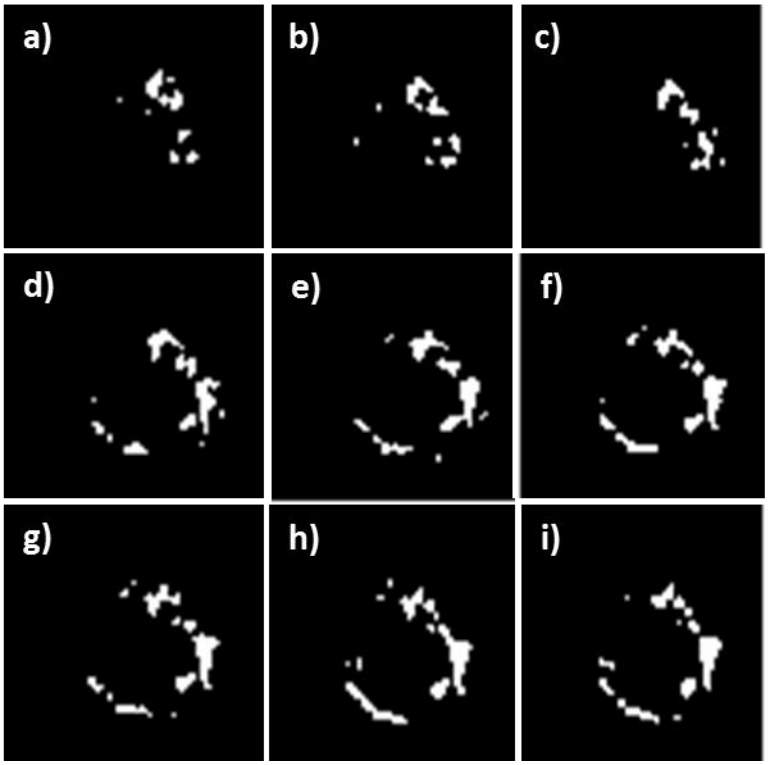

Figure 7.1.3: *The same layers with figure 2 after applying the threshold 22.*

What is more, the Matlab script presents in the end two histological graphics, which refer to the information about the frequency of having the same pixel brightness and next the same in logarithmic scale. In addition, in the bottom it presents statistics information about the intensity of the cell.

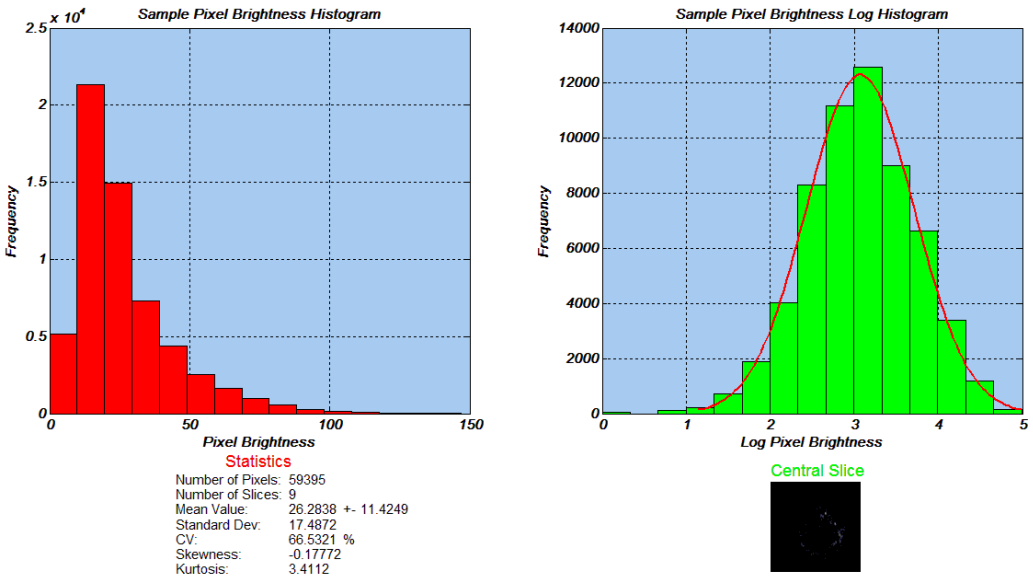

***Figure 7.1.4**: Statistics Results*

After that, the intensity's values of each cell, such as the in mean total area, are added in the SPSS program, in order to estimate the result of the statistical analysis.

7.2 Statistical results

The statistical analysis that was used for the experiments test for the total area and intensity of lipid particles is an independent sample test in the SPSS, which compares the means of the two groups' and was used to test for overall effect of treatment. The result values are given as mean ± standard deviation (SD) or standard error of the mean (SEM). However, in order to check if the difference between the means of the two groups is statistically significant, we check the output data that are processed in the SPSS. If the p (Levene's factor) is <0.05 then the difference is statistically significant.

In the case that the total area of the p was zero that means that the difference between the means of total area of control and activated cells was statistically significant. Specifically, figure 7.2.1 indicates that the mean total area of BV-2 microglia cells after activation is almost 10 times bigger than this of the control cells. 40 samples for each case (control and activated) were used.

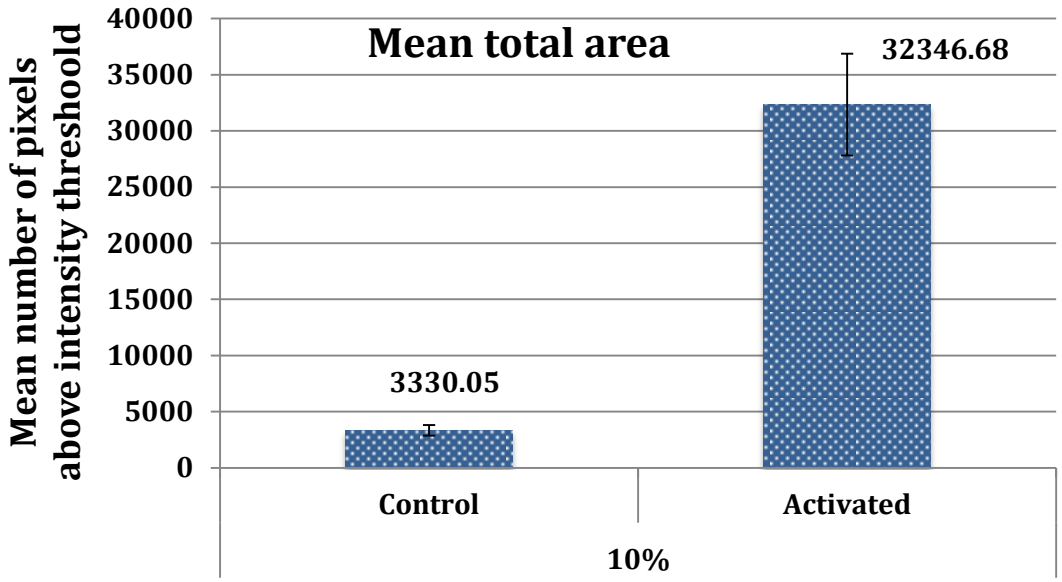

Figure 7.2.1. Distribution of the quantification of mean's total area THG signal for N=40 cells for each case and threshold 35.

For exactly the same cells we performed the quantification of Intensity THG signal and the results have shown that we are also statistically significant in intensity's THG signal between normal (control) and activated (lps) cells.

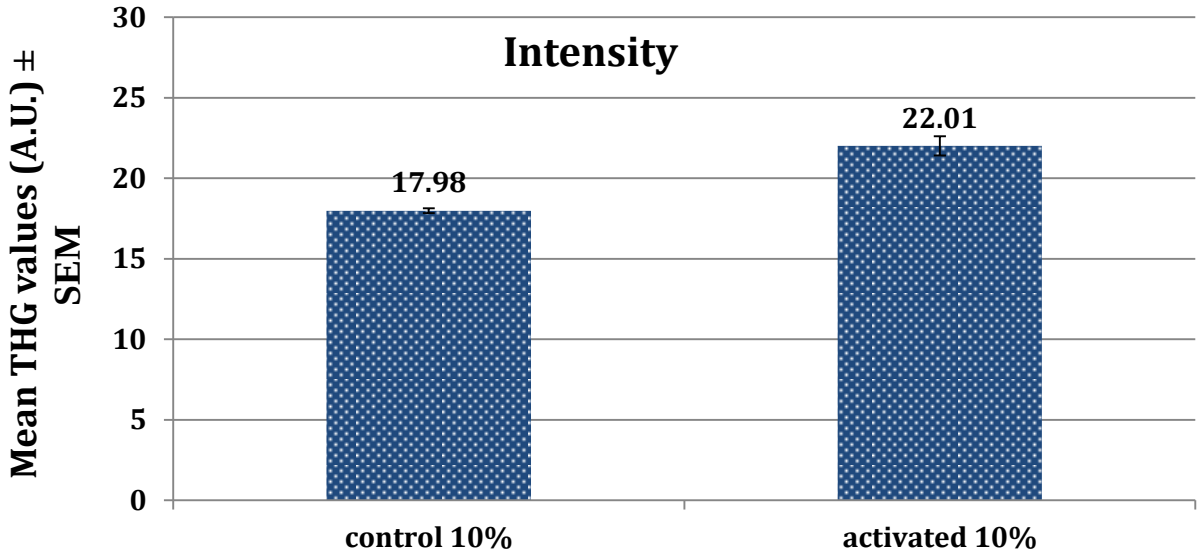

Figure 7.2.2. Distribution of the quantification of intensity's THG signal for N=40 cells and threshold 22.

The results presented that there is statistically significant difference both in case of mean number of pixels and mean THG values . This means that after the activation not only we have a bigger amount of subcellular structures – probably lipid droplets[94], but also something changes into their component . To conclude, the results obtained in this study, provide reliable biological criteria through a novel approach to study activation of BV-2 cells .The fact is that this technique does not require any staining and allows visualization of the subcellular structures of the cells.

Chapter 8. Quantification in different feed conditions

In this chapter we perform again the quantification of mean total area and intensity of THG signal, in order to check if the results of the previous chapter can be repeated in different feed conditions. The cells were prepared by using three different concentrations of serum culture medium FBS (Fetal Bovine Serum), with no feed (DMEM absence of serum 0%), normal (DMEM 10% FBS), and overfeed (DMEM 20% FBS).

Figure 8.1 below indicates three-dimensional images of control BV-2 cells with different feed conditions by the THG microscopy. As we can notice the 0% FBS cell (a) have almost no subcellular structures. However, in contrast to the 0% cell (b) with 10% FBS cell THG microscopy shows a small amount of subcellular structures. At the end the 20% FBS cell (c) has a big amount of subcellular structures, which are probably mainly lipid droplets. This result was expected as the different feed conditions connected with different amount of lipids inside the cell and THG microscopy, gives mainly signal from lipids (see chapter 5).

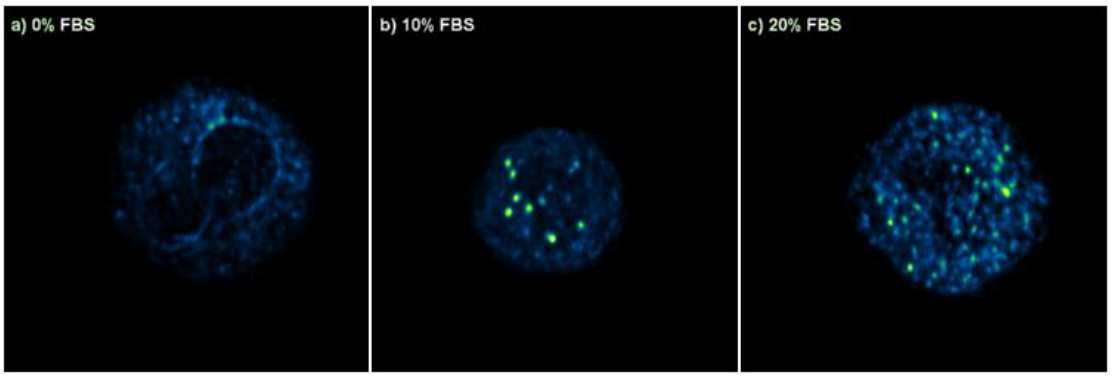

Figure 8.1: *Three Dimensional THG images of a) 0% FBS, 10% FBS , 20% FBS cells .*

The process of the quantification was exactly the same as the previous process described in chapter 7 and the threshold is still set to 35. We start with the 20% FBS cells, where the number of cells now is N=15 for each case. In case of quantification of mean total area, the results that obtained were that for N= 15 cells we still have contrast between control and activated cell, which was also statistically significant. Especially, in this case the difference of mean total area between control and activated cells is bigger, more than 10 times than this of N=40 10% cells, which was referred in the previous chapter.

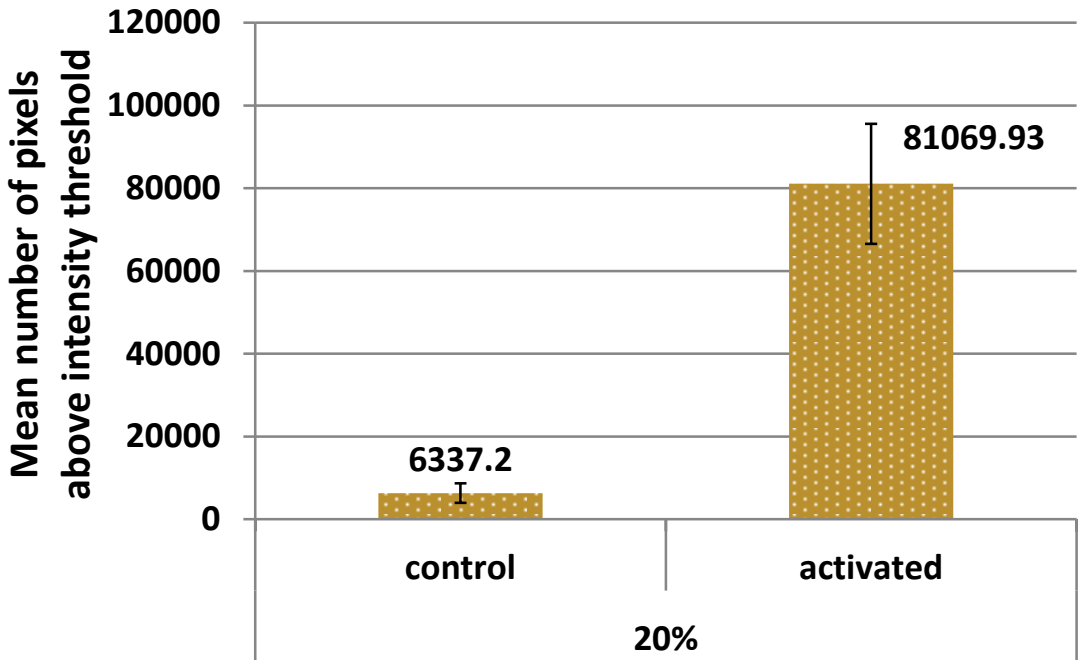

Figure 8.2: *Distribution of the quantification of mean's total area THG signal for N=15 cells 20% FBS BV-2 cells and threshold 35.*

In case of Intensity's quantification of THG signal, the process for the overfeed cell (20% FBS) was exactly the same with the one described in the previous chapter. Specifically, the threshold was set to 22. As we can observe from the graph presented below, there is also difference between control and activated cells in intensity of THG signal and in fact, the difference is statistically significant, even if we have a smaller amount of cells N=15.

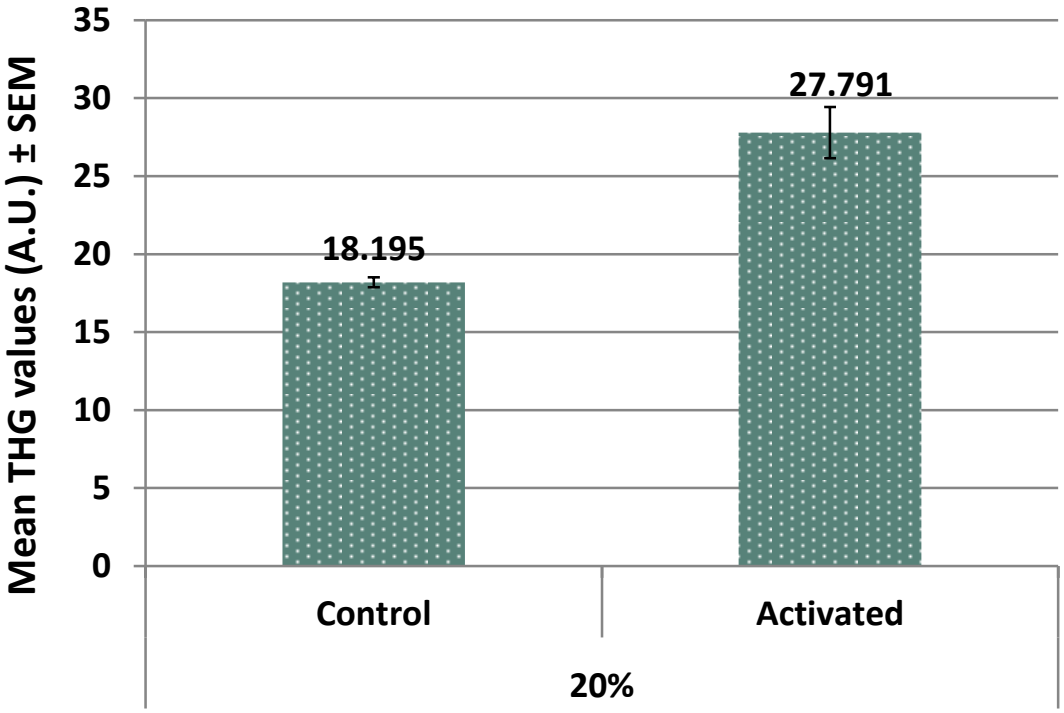

Figure 8.3 : *Distribution of the quantification of intensity's THG signal for N=15 ,20%FBS BV2 cells and threshold 22.*

To continue with, we make a comparison between the 20% and the 10% for both activated and control N=15 cell with threshold 35 in case of mean number of pixels and threshold 22 for Mean THG values.

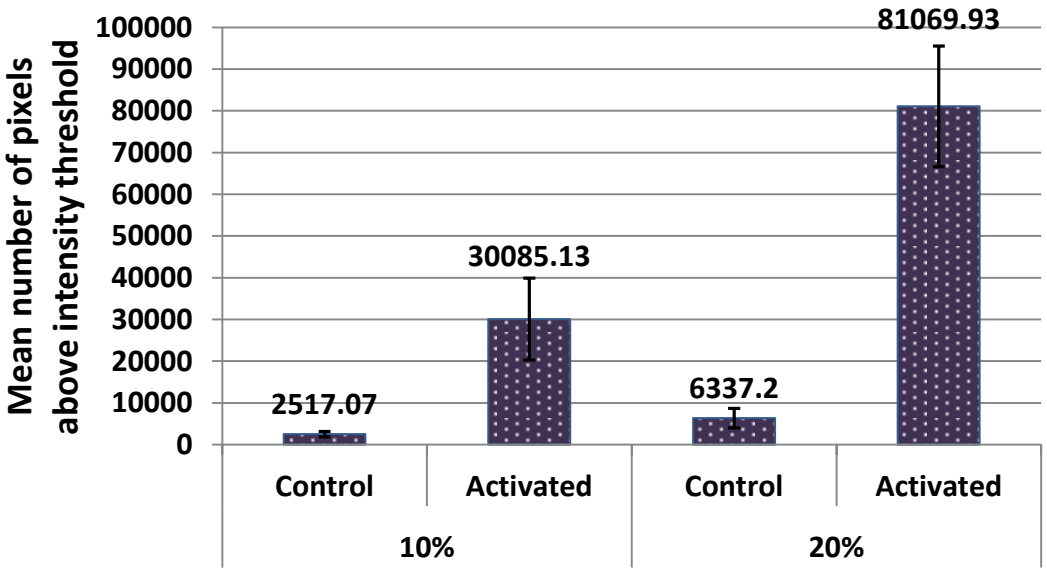

Figure 8.4: *Distribution of the quantification of mean's total area THG signal for N=15 cells 10% and 20% FBS BV-2 cells and threshold 35 respectively.*

Separately the values of mean number of pixels of control 10% and 20% cells are statistically significant. This result is expected, because as we are increasing the percentage of FBS THG intensity signal is increasing as well the amount of lipids of the cell.

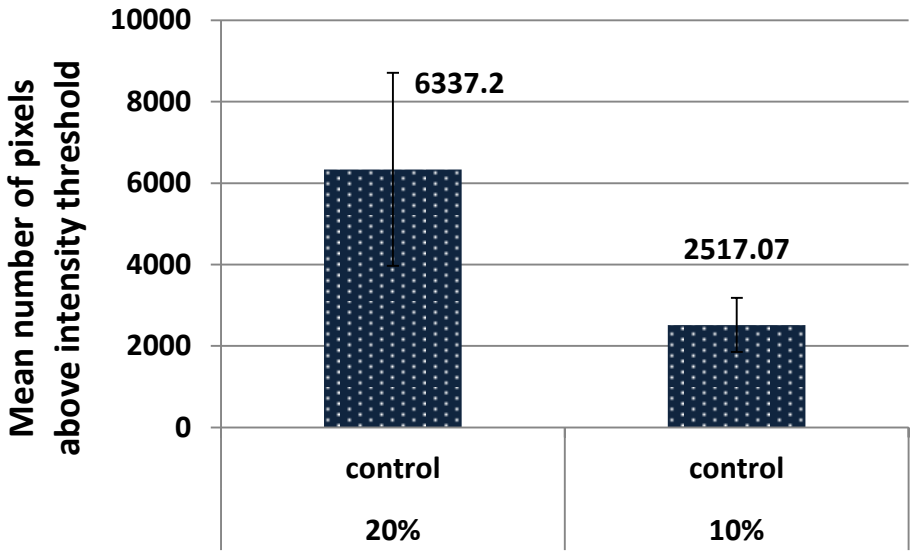

Figure 8.5 : *Comparison of the mean's total area THG signal for N=15 ,10% and 20%FBS BV2 control cells respectively and threshold 35.*

Similarly, the values of mean number of pixels of activated 10% and 20% N=15 cells are statistically significant.

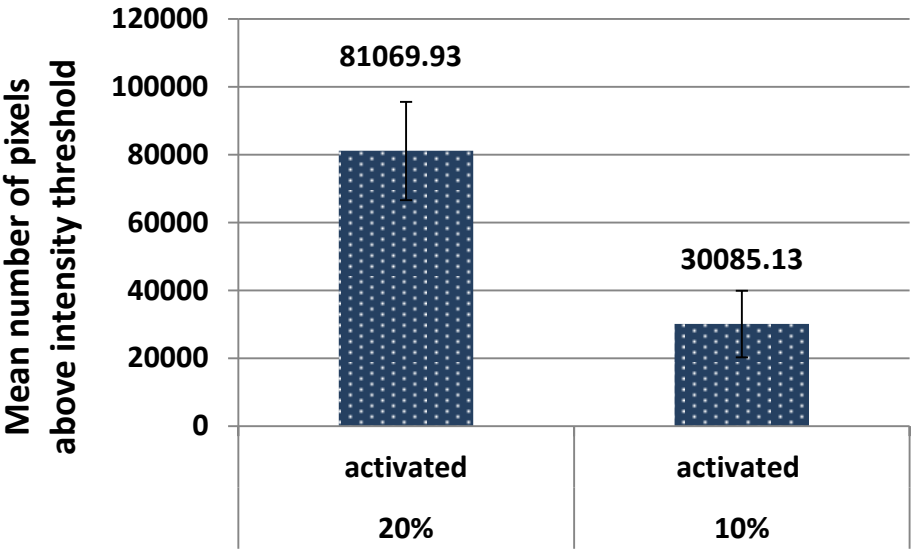

Figure 8.6 : *Comparison of the mean's total area THG signal for N=15 ,10% and 20%FBS BV2 activated cells and threshold 35.*

In case of mean THG values the results have shown that for different feed conditions with threshold 22, we had a small increase of mean THG values for both control and activated cells. However, the results are not statistically significant. This is probably caused, due to the small amount of cells (N=15)

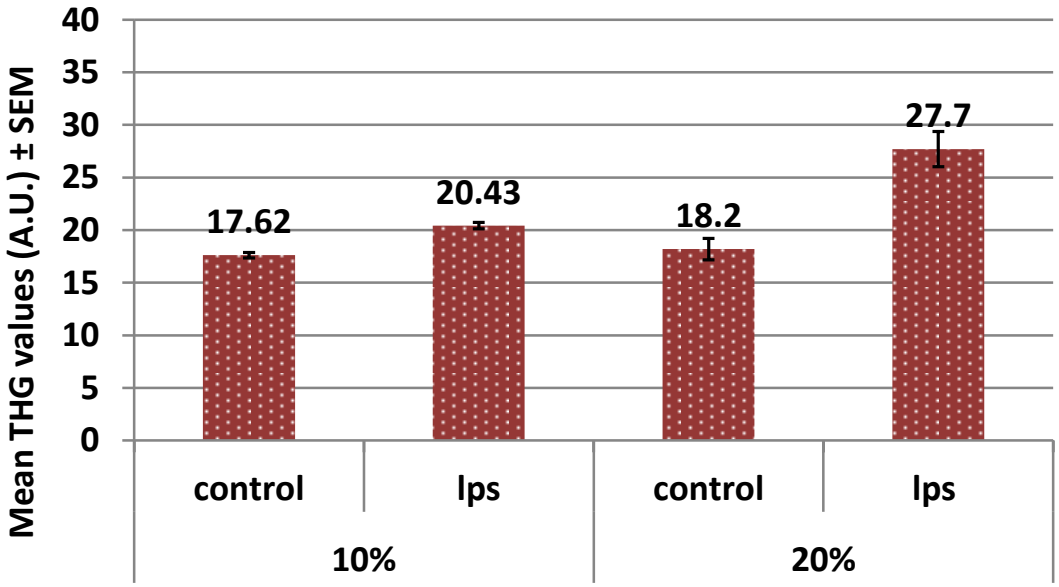

Figure 8.7 : *Distribution of the quantification of intensity's THG signal for N=15 , 10% and 20% FBS BV2 cells and threshold 22.*

By following separately the graphs for control and activated cells (graph 8.8 and 8.9 respectively) we can notice that the difference between 10% and 20% activated cells is bigger than the one of the controls.

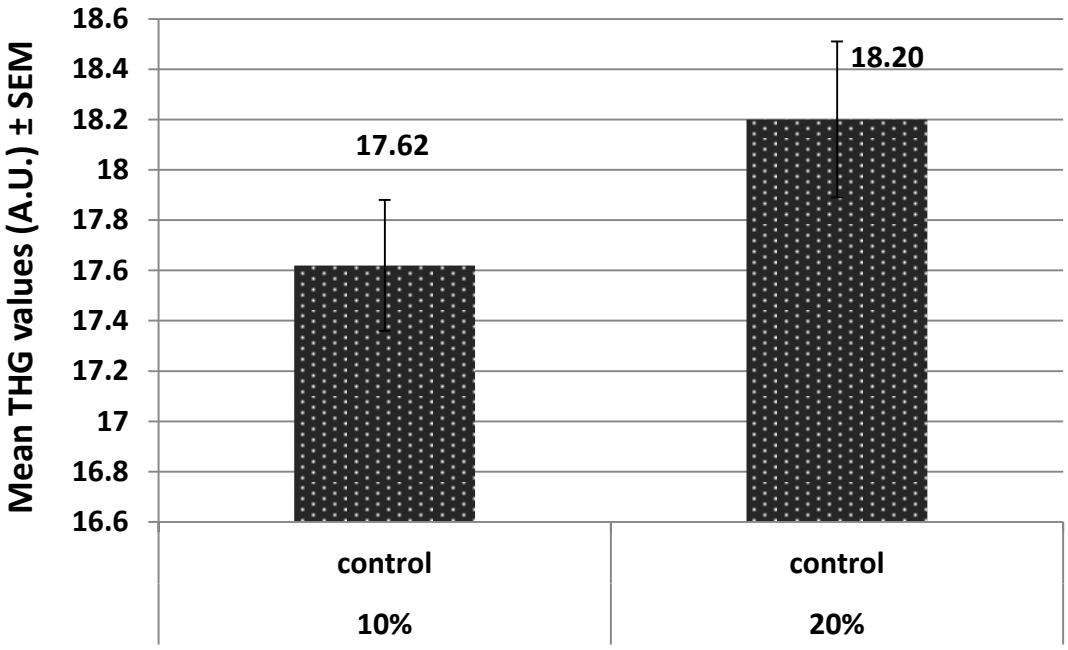

Figure 8.8 : *Comparison of the quantification of intensity's THG signal for N=15 ,10%FBS and 20% BV2 control cells and threshold 22.*

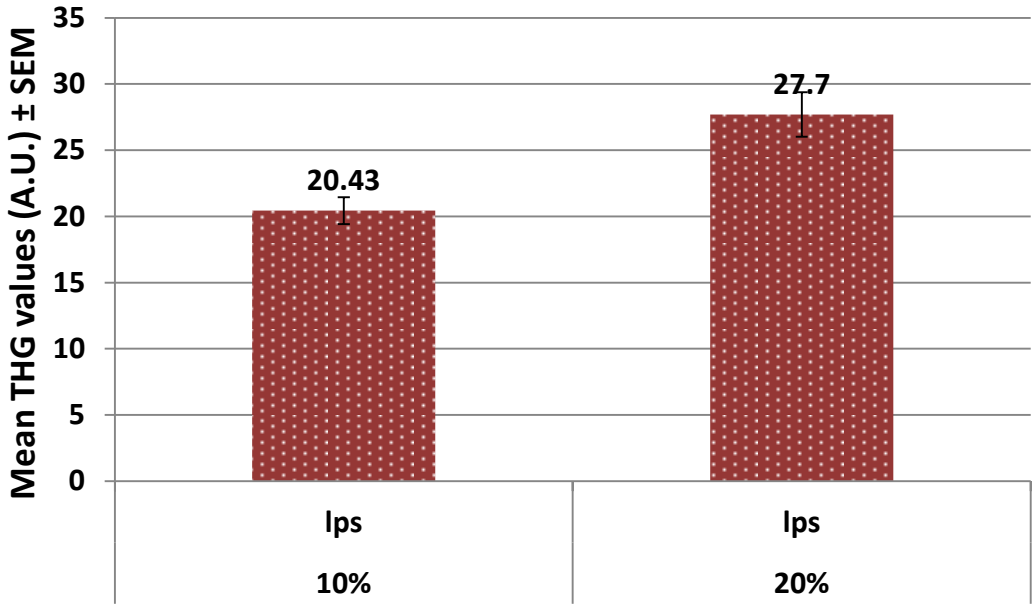

Figure 8.9 : *Comparison of the quantification of intensity's THG signal for N=15 ,10%FBS and 20% BV2 activated cells and threshold 22.*

To sum up, for the same N=15 cells we had significant difference in case of mean number of pixels above a threshold 35 between control and activated 10% and 20% FBS cells, while in mean THG values the difference between 10% and 20% control and activated cells was not significant. This is possibly happening, due to the fact that as we are increasing the percentage of FBS, the substances variations in lipid bodies are not important in order to create a difference.

Nevertheless, we could not use the same conditions of the process in case of serum free cells (0% FBS), because both the mean's total area and intensity's threshold have to be reduced to take THG signal (due to the absence of lipid bodies from the cells).

By using the new process conditions (reduced threshold), we could compare simultaneously the three different feed conditions. In case of quantification of mean total area the threshold was reduced from 35 to 25. The results are analyzed in the figure presented below.

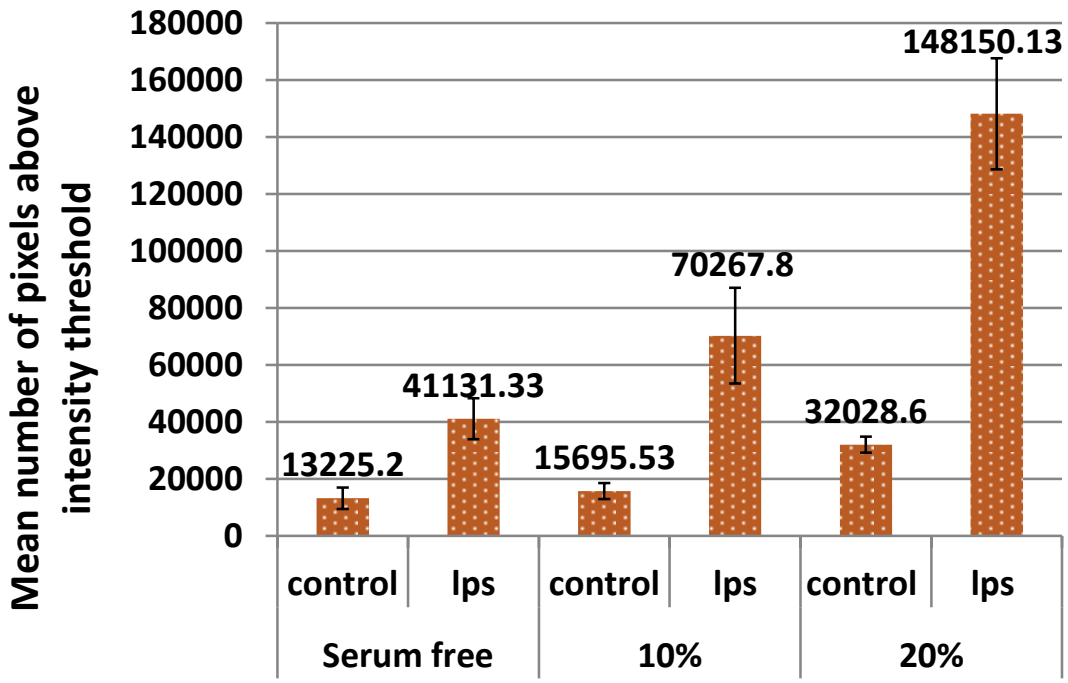

Figure 8.10:*Distribution of the quantification of mean's total area THG signal for N=15 cells (for each case control and activation) in 0% ,10% and 20% FBS BV-2 cells and threshold 25 respectively.*

As we can easily observe, we have differences in the mean total area between controls and activated of each category. In order to see the results isolated for control and activated respectively, the figures below were constructed.

Figure 8.11 indicates the results for control N=15 cells of serum free 0% control cells, normal cells 10% FBS cells and overfeed 20% FBS cells. The results have shown that there is difference between control of 0%, 10% and 20% and especially there is an increase of mean total area from 0% to 20%.

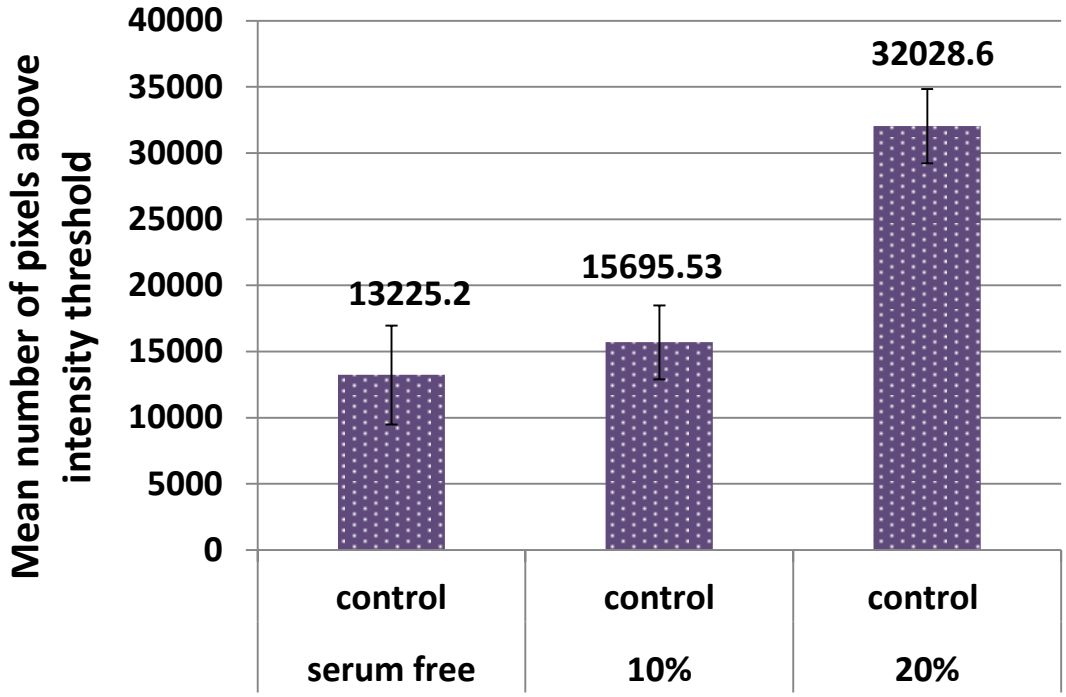

Figure 8.11: *Comparison of the quantification of mean's total area THG signal for N=15 cells in 0% ,10% and 20% FBS BV-2 control cells and threshold 25 respectively.*

Similarly, figure 8.12 indicates the results for N=15 activated cells for 0%, 10% and 20% FBS cells. As we can notice there is a big difference between each category. The 10% activated cells have almost double mean number of pixels above the intensity threshold of this of serum free. On the other hand, the 20% activated cells have double mean number of pixels than this of the 10% cells and more than three times of the one of serum free.

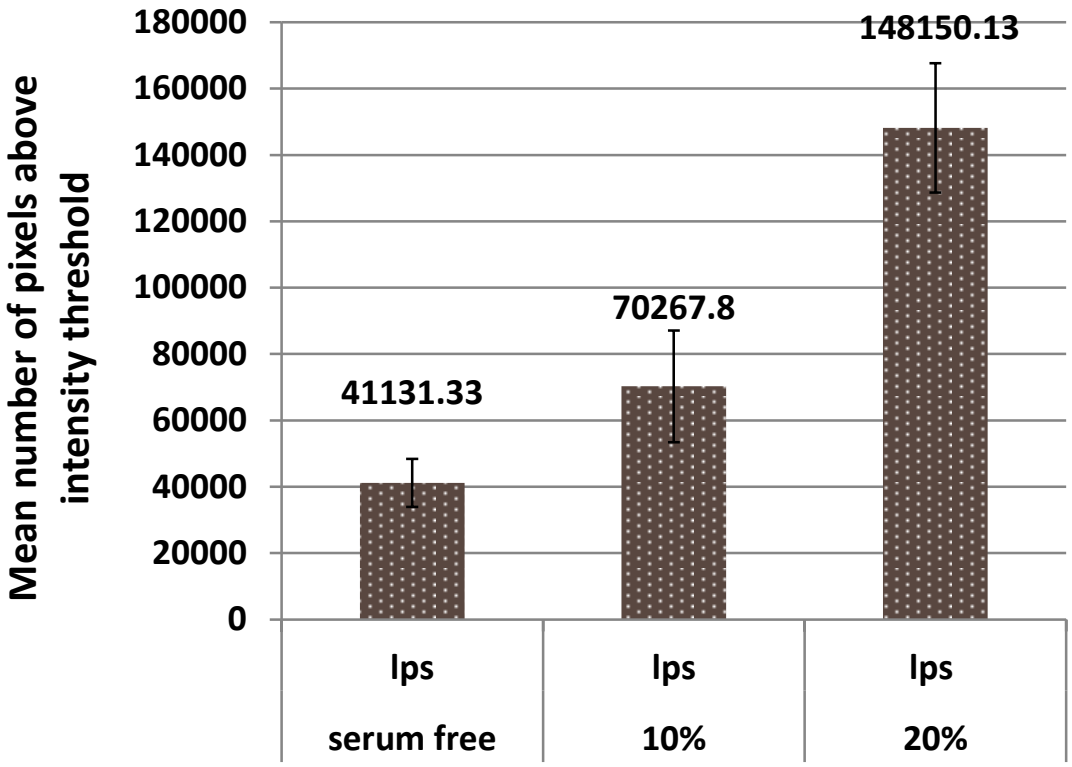

Figure 8.12: *Comparison of the quantification of mean's total area THG signal for N=15 cells in 0% ,10% and 20% FBS BV-2 activated cells and threshold 25 respectively.*

In case of Intensity's quantification of THG signal, the conditions that were used for the new process were by using low threshold 5 that leaves the whole THG signal of each cell intact. The figures presented below show 2D images of the cell before and after threshold in 9 different layers.

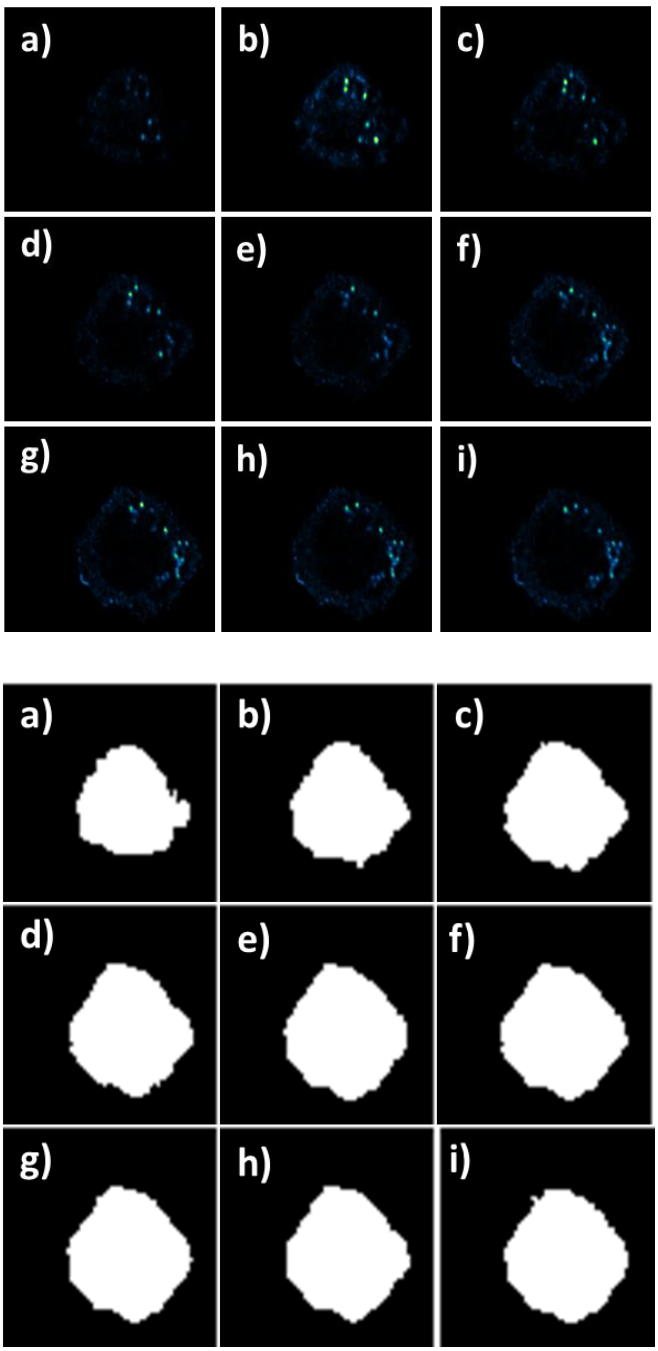

Figure 8.13: *Distribution of the process of Intensity's THG values quantification in case of threshold 5. The THG values come from all over the cell.*

The results of this process are described in the figure presented below. As it was previously performed, in mean total area, we had also compared simultaneously the different feed conditions for both control and activated N=15 cells for each case.

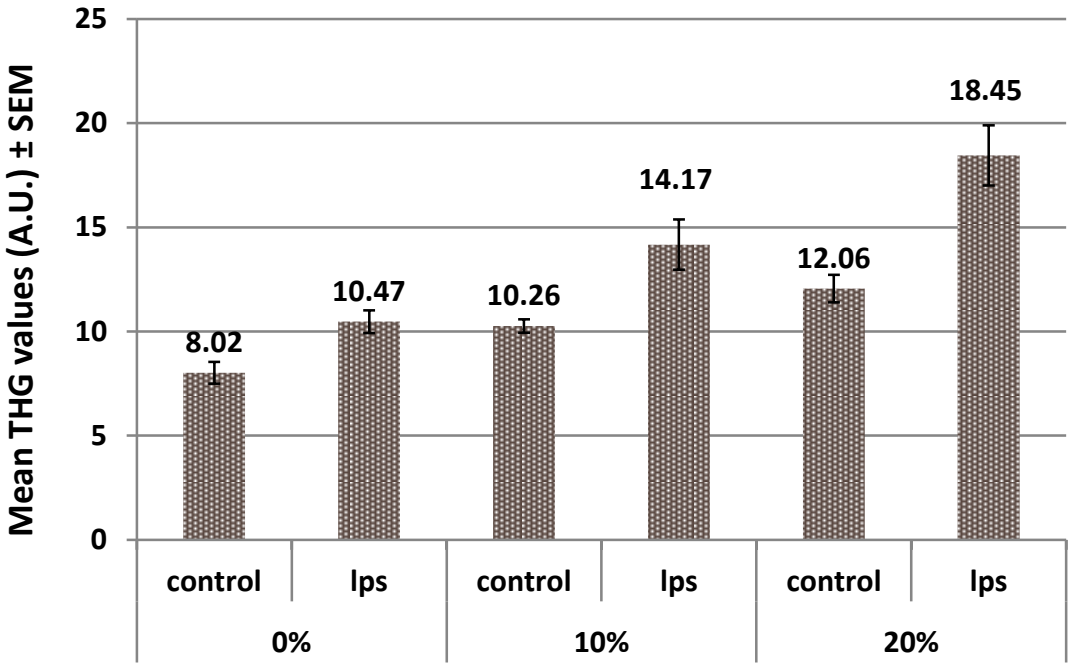

Figure 8.14 : *Distribution of the quantification of intensity's THG signal for N=15 , 0%, 10% and 20% FBS BV2 cells and threshold 5.*

In case of control cells, we can see that there is an increase of mean THG value between serum free cells (0%), normal cells (10%) and over-feed cells (20 %).

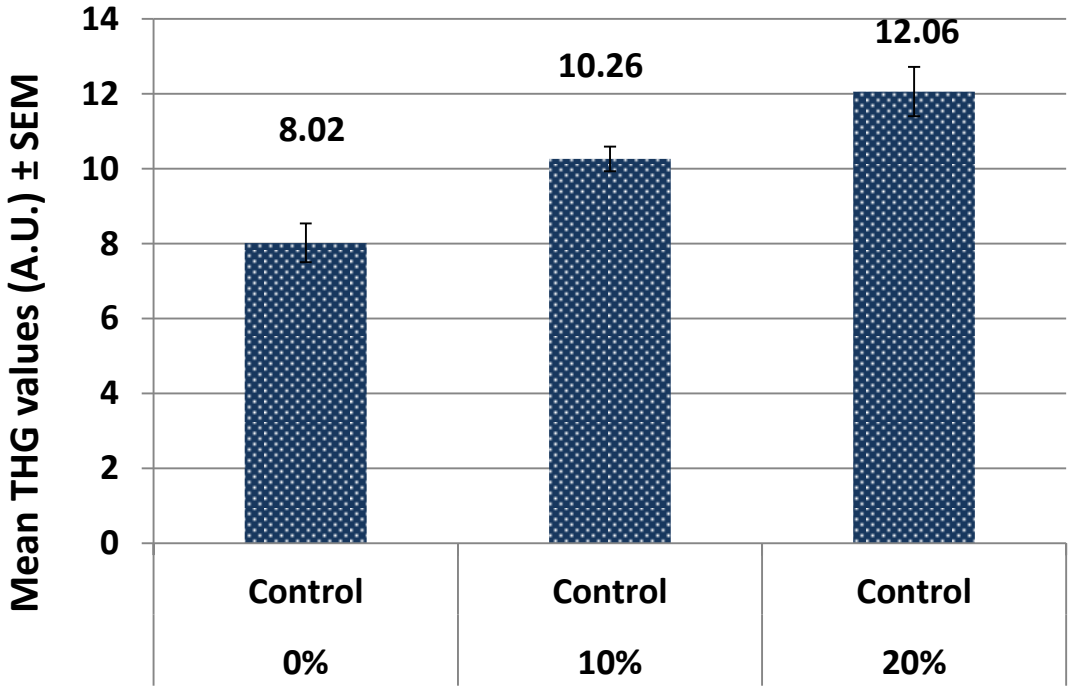

Figure 8.15: *Distribution of the quantification of intensity's THG signal for N=15 , 0%, 10% and 20% FBS BV2 control cells and threshold 5.*

Similarly, the activated cells present also an increase of mean THG values between 0%, 10% and 20% N=15 cells.

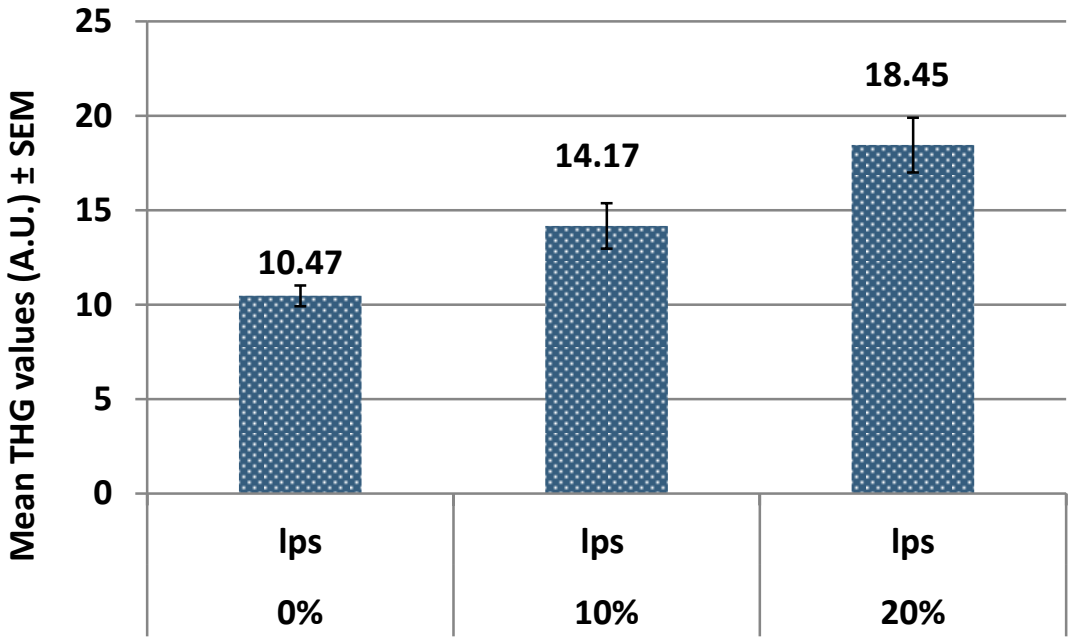

Figure 8.16 : *Distribution of the quantification of intensity's THG signal for N=15 , 0%, 10% and 20% FBS BV2 activated cells and threshold 5.*

The results of this reduced threshold, in case of Mean THG values, demonstrate that the intensity values are similar to those described in the previous chapter and that the THG signal values come from the internal region of the cell – subcellular structures. To sum up, BV2 cells present a significant difference, before and after activation, both for mean values of pixels above an intensity threshold and mean THG values for the different feed conditions.

Chapter 9. Conclusion and Future targets

9.1 Conclusion

The investigation of cancer cells is a significant issue that must be solved. For this reason, we used the BV-2 cell line as a representative biological model of cancer cells to investigate the situation before and after the cancer cells were activated. The investigation was accomplished by using the THG as diagnostic tool.

THG is beneficial for performing microscopy without the need for an external labelling procedure. Thus THG microscopy was firstly used simultaneously with other nonlinear microscopy techniques (TPEF) in a single laser beam, in order to check the source of THG signal of the intracellular structure. Specifically, we used the Nile red dye, which stained the lipid droplets of the cell, the Mitotracker FM that stained the mitochondria and the Alexa 488, which stained the endosomes. The experimental results have shown that the co-localization of the mitochondria and of the endosomes specific dyes respectively with the THG emitting structures was poor. In contrast, the colocalization of lipid droplets specific dye with the THG emitting structures was almost absolute in non-activated cells. Thus, we can claim that the main sub-cellular structures of control BV-2 cells that give high THG signals are the lipid droplets,. However, in case of activated cells that were stained with Nile red dye, the colocalization was not total; This is probably due to the activation since the components of lipid droplets changes Furthermore, THG microscopy with the help of number of programs was used to make a quantification of intracellular structures in both mean area values and mean THG intensity values. In this case the results have shown that in both cases the difference before and after the activation of the cells is statistically significant. Moreover, statistically quantification was also accomplished in both mean area and mean values of THG in different feed conditions. The values for mean total area and mean THG intensity values have been increased, as the amount of feed n both activated and non-activated cells was increased.

9.2 Future Prospects

THG has been successfully demonstrated in the three-dimensional microscopy of a variety of samples, such as non-invasive imaging of C. elegans [58], label-free imaging of lipid droplets in cells [94], in the human skin [102][109] and several others. Despite its proven potentials, THG has not yet found widespread application.

We believe the main obstacle towards development of THG as a general imaging tool, is the issue of specificity. The main contrast in THG is due to changes in nonlinear susceptibility and dispersion. Generally, little is known about the magnitude of the third-order nonlinear optical constants and the dispersion properties of the components of the system under investigation. Once that is readily available, the interpretation of THG images would be easier.

The wavelength dependence of the nonlinear optical constants could also provide information about the possible resonance enhancement, and thereby providing specificity (multi-color THG microscopy). We believe that a better understanding of the nonlinear optical constants of the biologically relevant samples at different excitation wavelengths is therefore necessary.

In case of the BV-2 cell line, it could be found a threshold of the value of THG signal intensity to separate the activated and non-activated cells. Thus, it could be a very promising method to use THG microscopy as a diagnostic tool to separate the cancer cells from the healthy ones.

Moreover, a future target comprises the quantitative analysis of χ^3 before and after activation in lipids, in order to find the provenance of the change of the THG signal intensity. We would be able to create separately lipid droplets, by changing the interior substances of the lipid and to calculate the χ^3 for each case. Specifically, we could study an empty lipid droplet or a full of proteins or other substances, in order to create literature about the change of lipids at activation. In addition, we could also perform the same processes, in other subcellular structures, such as mitochondria or endosomes.

Another difficulty that yet remains unsolved in the measurement of $\chi^{(3)}$ is the lack of information about the phase mismatch between the third-order polarization and the third-harmonic signal. Since dispersion properties of all the materials are not yet available in literature, it would be useful to device a methodology in order to obtain these values within the THG measurements. One way to proceed to it might be to use the dependence in the

shape of the THG z-response on the dispersion of the medium. An extensive study in this direction could be the subject matter of a future investigation.

References

[1] R. L. Sutherland, *Handbook of Nonlinear Optics*. CRC Press, 2003.

[2] M. Hillery, "An introduction to the quantum theory of nonlinear optics," *Acta Physica Slovaca. Reviews and Tutorials*, vol. 59, no. 1, pp. 1–80, Feb. 2009.

[3] K. F. Renk, *Basics of Laser Physics: For Students of Science and Engineering*. Springer, 2012.

[4] Y. R. Shen, "The principles of nonlinear optics," *New York, Wiley-Interscience, 1984, 575 p.*, vol. -1, 1984.

[5] "Propagation Characteristics of Laser Beams - CVI Melles Griot Technical Guide, Vol 2, Issue 2 - Propagation_Characteristics_of_Laser_Beams.pdf."

[6] J. Squier, M. Muller, G. Brakenhoff, and K. R. Wilson, "Third harmonic generation microscopy," *Opt. Express*, vol. 3, no. 9, pp. 315–324, 1998.

[7] N. Bloembergen, *Nonlinear optics*. Singapore; River Edge (N.J.); London [etc.]: World scientific, 1996.

[8] R. W. Boyd, *Nonlinear Optics*. Academic Press, 2003.

[9] M. Born and E. Wolf, *Principles of Optics: Electromagnetic Theory of Propagation, Interference and Diffraction of Light*. CUP Archive, 1999.

[10] P. N. Butcher and D. Cotter, *The Elements of Nonlinear Optics*. Cambridge University Press, 1991.

[11] Dielectric constants of various materials', 2007, Clipper Control.

[12] P. Török and F.-J. Kao, *Optical Imaging and Microscopy: Techniques and Advanced Systems*. Springer, 2003.

[13] F. Helmchen and W. Denk, "Deep tissue two-photon microscopy," *Nat Meth*, vol. 2, no. 12, pp. 932–940, 2005.

[14] S.Mulligan, and B.MacVicar, "Two-photon fluorescence microscopy: basic principles, advantages and risks," in Modern Research and Educational Topics in Microscopy , A. Méndez-Vilas, and J. Díaz, eds. (FORMATEX, Badajoz, Spain, 2007), pp. 881-889

[15] M. Oheim, D. J. Michael, M. Geisbauer, D. Madsen, and R. H. Chow, “Principles of two-photon excitation fluorescence microscopy and other nonlinear imaging approaches,” *Advanced Drug Delivery Reviews*, vol. 58, no. 7, pp. 788–808, 2006.

[16] P.T.C. So: Opt. Express 3, 312 (1998)

[17] R.D. Schaller, J.C. Johnson, K.R.Wilson, L.F. Lee, L.H. Haber, R.J. Saykally,: J. Phys. Chem. B 106, 5143 (2002)

[18] X. Zhuang, P.B. Miranda, D. Kim, Y.R. Shen: Phys. Rev. B 59, 12632 (1999)

[19] X. Wei, S.-C. Hong, X. Zhuang, T. Goto, Y.R. Shen: Phys. Rev. E 62, 5160 (2000)

[20] V. Vogel, Y.R. Shen: Annu. Rev. Mater. Sci. 21, 515 (1991)

[21] J. Ying, F. Liu, R.R. Alfano: Appl. Optics **39**, 509 (2000)

[22] M. Flörsheimer, C. Brillert, και H. Fuchs, ‘Chemical imaging of interfaces by sum-frequency generation’, Materials Science and Engineering: C, vol. 8–9, pp. 335–341, 1999.

[23] D. M. P. Hoffmann, K. Kuhnke, και K. Kern, ‘Sum-frequency generation microscope for opaque and reflecting samples’, *Review of Scientific Instruments*, vol. 73, no. 9, pp 3221–3226, 2002.

[24] N. Ji, K. Zhang, H. Yang, και Y.-R. Shen, ‘Three-Dimensional Chiral Imaging by Sum-Frequency Generation’, J. Am. Chem. Soc., vol. 128, no. 11, pp 3482–3483, 2006.

[25] D. Yelin, D. Oron, E. Korkotian, M. Segal, and Y. Silberberg, “Third-harmonic microscopy with a titanium–sapphire laser,” Appl Phys B, vol. 74, no. 1, pp. s97–s101, Jun. 2002.

[26] J.-X. Cheng, ‘Coherent Anti-Stokes Raman Scattering Microscopy’, *Appl Spectrosc*, vol. 61, no. 9, pp 197–208, September 2007.

[27] J.R. Lakowicz and I. Gryczynski, H. Malak, P. Schrader, P. Engelhardt, H. Kano,S.W. Hell: Biophys. J. **72**, 567 (1997)

[28] S.Maiti, J.B. Shear, R.M.Williams,W.R. Zipfel,W.W.Webb: Science **275**, 530 (1997)

[29] W. Denk, J. H. Strickler, and W. W. Webb, “Two-photon laser scanning fluorescence microscopy,” *Science*, vol. 248, no. 4951, pp. 73–76, Apr. 1990.

[30] M. Hashimoto, T. Araki, S. Kawata: Opt. Lett. **25**, 1768 (2000)

[31] S. W. Hell, "Far-Field Optical Nanoscopy," in *Single Molecule Spectroscopy in Chemistry, Physics and Biology*, A. Gräslund, R. Rigler, and J. Widengren, Eds. Springer Berlin Heidelberg, 2010, pp. 365–398.

[32] J. Squier and M. Muller, "High resolution nonlinear microscopy: A review of sources and methods for achieving optimal imaging," *Review of Scientific Instruments*, vol. 72, no. 7, pp. 2855–2867, 2001.

[33] P. J. Campagnola, M. Wei, A. Lewis, and L. M. Loew, "High-Resolution Nonlinear Optical Imaging of Live Cells by Second Harmonic Generation," *Biophysical Journal*, vol. 77, no. 6, pp. 3341–3349, 1999.

[34] C.-K. Sun, S.-W. Chu, S.-Y. Chen, T.-H. Tsai, T.-M. Liu, C.-Y. Lin, and H.-J. Tsai, "Higher harmonic generation microscopy for developmental biology," *Journal of Structural Biology*, vol. 147, no. 1, pp. 19–30, 2004.

[35] V. Westphal, S. O. Rizzoli, M. A. Lauterbach, D. Kamin, R. Jahn, and S. W. Hell, "Video-Rate Far-Field Optical Nanoscopy Dissects Synaptic Vesicle Movement," *Science*, vol. 320, no. 5873, pp. 246–249, Apr. 2008.

[36] Z. Gitai, "New fluorescence microscopy methods for microbiology: sharper, faster, and quantitative," *Current Opinion in Microbiology*, vol. 12, no. 3, pp. 341–346, 2009.

[37] R. C. Piper and D. J. Katzmann, "Biogenesis and Function of Multivesicular Bodies," *Annu Rev Cell Dev Biol*, vol. 23, pp. 519–547, 2007.

[38] P. Friedl, K. Wolf, G. Harms, and U. H. von Andrian, "Biological Second and Third Harmonic Generation Microscopy," in *Current Protocols in Cell Biology*, John Wiley & Sons, Inc., 2001.

[39] K. Svoboda και R. Yasuda, 'Principles of Two-Photon Excitation Microscopy and Its Applications to Neuroscience', *Neuron*, vol. 50, no. 6, pp 823–839, 2006.

[40] J. Mertz, 'Nonlinear microscopy: new techniques and applications', *Current Opinion in Neurobiology*, vol. 14, no. 5, pp 610–616, 2004.

[41] S.Mulligan, and B.MacVicar, “Two-photon fluorescence microscopy: basic principles, advantages and risks,” in Modern Research and Educational Topics in Microscopy , A. Méndez-Vilas, and J. Díaz, eds , pp. 881-889

[42] B. Valeur and M. N. Berberan-Santos, *Molecular Fluorescence: Principles and Applications*. John Wiley & Sons, 2013.

[43] C. Xu, W. Zipfel, J. B. Shear, R. M. Williams, και W. W. Webb, ‘Multiphoton fluorescence excitation: new spectral windows for biological nonlinear microscopy’, *PNAS*, τ. 93, vol. 20, pp 10763–10768, January 1996.

[44] R. M. Williams, W. R. Zipfel, and W. W. Webb, “Multiphoton microscopy in biological research,” *Current Opinion in Chemical Biology*, vol. 5, no. 5, pp. 603–608, 2001.

[45] K. König, “Multiphoton microscopy in life sciences,” *Journal of Microscopy*, vol. 200, no. 2, pp. 83–104, 2000.

[46] D. W. Piston, “Imaging living cells and tissues by two-photon excitation microscopy,” Trends in Cell Biology, vol. 9, no. 2, pp. 66–69, 1999.

[47] F. Helmchen and W. Denk, “Deep tissue two-photon microscopy,” *Nat Meth*, vol. 2, no. 12, pp. 932–940, 2005.

[48] G. J. Tserevelakis, G. Filippidis, E. V. Megalou, C. Fotakis, and N. Tavernarakis, “Cell tracking in live Caenorhabditis elegans embryos via third harmonic generation imaging microscopy measurements,” *J. Biomed. Opt*, vol. 16, no. 4, pp. 046019–046019–6, 2011.

[49] R. M. Williams, W. R. Zipfel, and W. W. Webb, “Multiphoton microscopy in biological research,” *Current Opinion in Chemical Biology*, vol. 5, no. 5, pp. 603–608, 2001.

[50] W. R. Zipfel, R. M. Williams, and W. W. Webb, “Nonlinear magic: multiphoton microscopy in the biosciences,” *Nat Biotech*, vol. 21, no. 11, pp. 1369–1377, 2003.

[51] P. Török and F.-J. Kao, *Optical Imaging and Microscopy: Techniques and Advanced Systems*. Springer, 2003.

[52] P. T. C. So, C. Y. Dong, B. R. Masters, and K. M. Berland, “Two-Photon Excitation Fluorescence Microscopy,” *Annual Review of Biomedical Engineering*, vol. 2, no. 1, pp. 399–429, 2000.

[53] A. Diaspro and M. Robello, “Two-photon excitation of fluorescence for three-dimensional optical imaging of biological structures,” *Journal of Photochemistry and Photobiology B: Biology*, vol. 55, no. 1, pp. 1–8, 2000.

[54] A. Diaspro, G. Chirico, and M. Collini, “Two-photon fluorescence excitation and related techniques in biological microscopy,” *Quarterly Reviews of Biophysics*, vol. 38, no. 02, pp. 97–166, 2005.

[55] L. A. Bagatolli and E. Gratton, “Two-Photon Fluorescence Microscopy Observation of Shape Changes at the Phase Transition in Phospholipid Giant Unilamellar Vesicles,” *Biophysical Journal*, vol. 77, no. 4, pp. 2090–2101, 1999.

[56] W. Denk, D. W. Piston, και W. W. Webb, ‘Two-Photon Molecular Excitation in Laser-Scanning Microscopy’, στο *Handbook of Biological Confocal Microscopy*, J. B. Pawley, Springer US, 1995, pp 445–458.

[57] M. Rubart, “Two-Photon Microscopy of Cells and Tissue,” *Circulation Research*, vol. 95, no. 12, pp. 1154–1166, Dec. 2004.

[58] G. J. Tserevelakis, E. V. Megalou, G. Filippidis, B. Petanidou, C. Fotakis, and N. Tavernarakis, “Label-Free Imaging of Lipid Depositions in C. elegans Using Third-Harmonic Generation Microscopy,” *PLoS ONE*, vol. 9, no. 1, p. e84431, 2014.

[59] G. A. Tanner, R. M. Sandoval, και K. W. Dunn, ‘Two-photon in vivo microscopy of sulfonefluorescein secretion in normal and cystic rat kidneys’, American Journal of Physiology - Renal Physiology, vol. 286, no. 1, pp F152–F160, January 2004.

[60] A. Zoumi, A. Yeh, και B. J. Tromberg, ‘Imaging cells and extracellular matrix in vivo by using second-harmonic generation and two-photon excited fluorescence’, PNAS, vol. 99, no. 17, pp 11014–11019, August 2002.

[61] E. Beaurepaire, M. Oheim, και J. Mertz, ‘Ultra-deep two-photon fluorescence excitation in turbid media’, *Optics Communications*, vol. 188, no. 1–4, pp 25–29, 2001.

[62] T. G. Oertner, ‘Functional imaging of single synapses in brain slices’, Exp Physiol, vol. 87, no. 6, pp 733–736, January 2002.

[63] B. L. Sabatini και K. Svoboda, ‘Analysis of calcium channels in single spines using optical fluctuation analysis’, Nature, vol. 408, no. 6812, pp 589–593, 2000.

[64] C.-K. Sun, S.-W. Chu, S.-Y. Chen, T.-H. Tsai, T.-M. Liu, C.-Y. Lin, and H.-J. Tsai, “Higher harmonic generation microscopy for developmental biology,” *Journal of Structural Biology*, vol. 147, no. 1, pp. 19–30, 2004.

[65] E. Brown, T. McKee, E. diTomaso, A. Pluen, B. Seed, Y. Boucher, και R. K. Jain, ‘Dynamic imaging of collagen and its modulation in tumors in vivo using second-harmonic generation’, *Nat Med*, vol. 9, no. 6, pp 796–800, 2003.

[66] S.-W. Chu, I.-H. Chen, T.-M. Liu, P. C. Chen, C.-K. Sun, και B.-L. Lin, ‘Multimodal nonlinear spectral microscopy based on a femtosecond Cr:forsterite laser’, *Opt. Lett.*, vol. 26, no. 23, pp 1909–1911, 2001.

[67] Y. Guo, P. P. Ho, A. Tirksliunas, F. Liu, και R. R. Alfano, ‘Optical harmonic generation from animal tissues by the use of picosecond and femtosecond laser pulses’, *Appl. Opt.*, vol. 35, no. 34, pp 6810–6813, 1996.

[68] G. Peleg, A. Lewis, M. Linial, και L. M. Loew, ‘Nonlinear optical measurement of membrane potential around single molecules at selected cellular sites’, *PNAS*, vol. 96, no. 12, pp 6700–6704, August 1999.

[69] J. N. Gannaway και C. J. R. Sheppard, ‘Second-harmonic imaging in the scanning optical microscope’, *Opt Quant Electron*, vol. 10, no. 5, pp 435–439, September 1978.

[70] Y. R. Shen, ‘Surface properties probed by second-harmonic and sum-frequency generation’, *Nature*, vol. 337, no. 6207, pp 519–525, February 1989.

[71] S.-W. C. Chi-Kuang Sun, ‘Scanning second-harmonic/third-harmonic generation microscopy of gallium nitride’, *Applied Physics Letters*, vol. 77, no. 15, pp 2331–2333, 2000.

[72] W.-L. Chen, T.-H. Li, P.-J. Su, C.-K. Chou, P. T. Fwu, S.-J. Lin, D. Kim, P. T. C. So, και C.-Y. Dong, ‘Second-order susceptibility imaging with polarization-resolved second harmonic generation microscopy’, 2010, vol. 7569, no 75691P–75691P–7.

[73] S. V. Plotnikov, A. C. Millard, P. J. Campagnola, και W. A. Mohler, ‘Characterization of the Myosin-Based Source for Second-Harmonic Generation from Muscle Sarcomeres’, *Biophysical Journal*, vol. 90, no. 2, pp 693–703, 2006.

[74] S.-W. Teng, H.-Y. Tan, J.-L. Peng, H.-H. Lin, K. H. Kim, W. Lo, Y. Sun, W.-C. Lin, S.-J. Lin, S.-H. Jee, P. T. C. So, και C.-Y. Dong, ‘Multiphoton Autofluorescence and Second-Harmonic

Generation Imaging of the Ex Vivo Porcine Eye', *IOVS*, vol. 47, no. 3, pp 1216–1224, January 2006.

[75] P. J. Campagnola, A. C. Millard, M. Terasaki, P. E. Hoppe, C. J. Malone, και W. A. Mohler, 'Three-Dimensional High-Resolution Second-Harmonic Generation Imaging of Endogenous Structural Proteins in Biological Tissues', *Biophysical Journal*, vol. 82, no. 1, pp 493–508, 2002.

[76] Y. Liu, H.-C. Chen, T.-L. Sun, L.-L. Chiou, C.-Y. Dong, H.-S. Lee, G. T. Huang, W. Lo, και S.-M. Yang, 'Visualization of hepatobiliary excretory function by intravital multiphoton microscopy', *J. Biomed. Opt*, vol. 12, no. 1, pp 014014–014014–5, 2007.

[77] E. B. Brown, R. B. Campbell, Y. Tsuzuki, L. Xu, P. Carmeliet, D. Fukumura, και R. K. Jain, 'In vivo measurement of gene expression, angiogenesis and physiological function in tumors using multiphoton laser scanning microscopy', *Nat Med*, vol. 7, no. 7, pp 864–868, 2001.

[78] H.-Y. Tan, Y. Sun, W. Lo, S.-J. Lin, C.-H. Hsiao, Y.-F. Chen, S. C.-M. Huang, W.-C. Lin, S.-H. Jee, H.-S. Yu, και C.-Y. Dong, 'Multiphoton Fluorescence and Second Harmonic Generation Imaging of the Structural Alterations in Keratoconus Ex Vivo', *IOVS*, vol. 47, no. 12, pp 5251–5259, January 2006.

[79] S.-J. Lin, S.-H. Jee, C.-J. Kuo, R.-J. Wu, W.-C. Lin, J.-S. Chen, Y.-H. Liao, C.-J. Hsu, T.-F. Tsai, Y.-F. Chen, και C.-Y. Dong, 'Discrimination of basal cell carcinoma from normal dermal stroma by quantitative multiphoton imaging', *Opt. Lett.*, vol. 31, no. 18, pp 2756–2758, 2006.

[80] M.-G. Lin, S.-H. Jee, Y.-F. Chen, S.-J. Lin, C.-Y. Dong, T.-L. Yang, C.-T. Chiang, H.-C. Kao, J.-N. Lee, και W. Lo, 'Evaluation of dermal thermal damage by multiphoton autofluorescence and second-harmonic-generation microscopy', *J. Biomed. Opt*, vol. 11, no. 6, pp 064006–064006–6, 2006.

[81] H.-S. Lee, S.-W. Teng, H.-C. Chen, W. Lo, Y. Sun, T.-Y. Lin, L.-L. Chiou, C.-C. Jiang, και C.-Y. Dong, 'Imaging Human Bone Marrow Stem Cell Morphogenesis in Polyglycolic Acid Scaffold by Multiphoton Microscopy', *Tissue Engineering*, vol. 12, no. 10, pp 2835–2841, October 2006.

[82] S.-W. Chu, S.-Y. Chen, G.-W. Chern, T.-H. Tsai, Y.-C. Chen, B.-L. Lin, και C.-K. Sun, 'Studies of χ(2)/χ(3) Tensors in Submicron-Scaled Bio-Tissues by Polarization Harmonics Optical Microscopy', *Biophysical Journal*, vol. 86, no. 6, pp 3914–3922, 2004.

[83] P. Stoller, B.-M. Kim, A. M. Rubenchik, K. M. Reiser, και L. B. Da Silva, 'Polarization-dependent optical second-harmonic imaging of a rat-tail tendon', *J. Biomed. Opt*, vol. 7, no. 2, pp 205–214, 2002.

[84] G. C. Cox, P. Xu, C. J. R. Sheppard, και J. A. Ramshaw, 'Characterization of the second harmonic signal from collagen', 2003, vol. 4963, pp 32–40.

[85] S.-W. Chu, S.-P. Tai, C.-K. Sun, και C.-H. Lin, 'Selective imaging in second-harmonic-generation microscopy by polarization manipulation', *Applied Physics Letters*, vol. 91, no. 10, σ 103903, September 2007.

[86] Y. Barad, H. Eisenberg, M. Horowitz, and Y. Silberberg, "Nonlinear scanning laser microscopy by third harmonic generation," *Applied Physics Letters*, vol. 70, no. 8, pp. 922–924, 1997.

[87] T. Y. F. Tsang, 'Optical third-harmonic generation at interfaces', *Phys. Rev. A*, vol 52, no 5, pp 4116–4125, 1995.

[88] C.-K. Chen και T.-M. Liu, 'Imaging morphodynamics of human blood cells in vivo with video-rate third harmonic generation microscopy', *Biomed Opt Express*, vol 3, no 11, pp 2860–2865, October 2012.

[89] W. Supatto, D. Débarre, B. Moulia, E. Brouzés, J.-L. Martin, E. Farge, και E. Beaurepaire, 'In vivo modulation of morphogenetic movements in Drosophila embryos with femtosecond laser pulses', *PNAS*, vol 102, no 4, pp 1047–1052, January 2005.

[90] G. J. Tserevelakis, S. Psycharakis, B. Resan, F. Brunner, E. Gavgiotaki, K. Weingarten, και G. Filippidis, 'Femtosecond laser nanosurgery of sub-cellular structures in HeLa cells by employing Third Harmonic Generation imaging modality as diagnostic tool', *J Biophotonics*, vol. 5. no. 2, pp 200–207, February 2012.

[91] S.-W. Chu, S.-Y. Chen, T.-H. Tsai, T.-M. Liu, C.-Y. Lin, H.-J. Tsai, και C.-K. Sun, 'In vivo developmental biology study using noninvasive multi-harmonic generation microscopy', *Opt. Express*, vol 11, no 23, pp 3093–3099, 2003.

[92] C.-K. Sun, C.-C. Chen, S.-W. Chu, T.-H. Tsai, Y.-C. Chen, και B.-L. Lin, 'Multiharmonic-generation biopsy of skin', *Opt. Lett.*, vol 28, no 24, pp 2488–2490, 2003.

[93] "D. Yelin, "Laser scanning third-harmonic-generation microscopy in biology". Optics express (1094-4087), 5 (8), p. 169.

[94] D. Débarre, W. Supatto, A.-M. Pena, A. Fabre, T. Tordjmann, L. Combettes, M.-C. Schanne-Klein, and E. Beaurepaire, “Imaging lipid bodies in cells and tissues using third-harmonic generation microscopy,” *Nat Meth*, vol. 3, no. 1, pp. 47–53, 2006.

[95] G.J.Tserevelakis, G. Filippidis “Nonlinear imaging at microscopic level for biological applications”

[96] Y. H. Choi and H. Y. Park, “Anti-inflammatory effects of spermidine in lipopolysaccharide-stimulated BV2 microglial cells,” Journal of Biomedical Science, vol. 19, no. 1, p. 31, Mar. 2012.

[97] “BV-2 Microglia lab - PsychLabs,” Available: https://sites.google.com/a/northgeorgia.edu/psychlabs/home/neuroscience/bv-2-microglia-lab.

[98] F. Aloisi, ‘Immune function of microglia’, *Glia*, vol. 36, no. 2, pp. 165–179, 2001.

[99] D. Débarre, N. Olivier, and E. Beaurepaire, “Signal epidetection in third-harmonic generation microscopy of turbid media,” Optics Express, vol. 15, no. 14, p. 8913, 2007.

[100] R. M. Adibhatla, J. F. Hatcher, and R. J. Dempsey, “Lipids and lipidomics in brain injury and diseases,” *AAPS J*, vol. 8, no. 2, pp. E314–E321, Jun. 2006.

[101] R. M. Adibhatla and J. F. Hatcher, “Altered Lipid Metabolism in Brain Injury and Disorders,” in *Lipids in Health and Disease*, P. J. Quinn and X. Wang, Eds. Springer Netherlands, 2008, pp. 241–268.

[102] P. D. Stahl and M. A. Barbieri, “Multivesicular Bodies and Multivesicular Endosomes: The ‘Ins and Outs’ of Endosomal Traffic,” *Sci. STKE*, vol. 2002, no. 141, p. pe32, 2002.

[103] D. Débarre, W. Supatto, and E. Beaurepaire, “Structure sensitivity in third-harmonic generation microscopy,” *Opt. Lett.*, vol. 30, no. 16, pp. 2134–2136, 2005.

[104] Muller, Squier, Wilson, and Brakenhoff, “3D microscopy of transparent objects using third-harmonic generation,” *Journal of Microscopy*, vol. 191, no. 3, pp. 266–274, Sep. 1998.

[105] J.-X. Cheng and X. S. Xie, “Green’s function formulation for third-harmonic generation microscopy,” *J. Opt. Soc. Am. B*, vol. 19, no. 7, pp. 1604–1610, 2002.

[106] R. Sreedharanpillai, “Third-harmonic generation from isotropic and anisotropic media using focused laser beams,” 2007

[107] K. M. Hanson and C. J. Bardeen, “Application of Nonlinear Optical Microscopy for Imaging Skin†,” *Photochemistry and Photobiology*, vol. 85, no. 1, pp. 33–44, 2009.

[108] T. Watanabe, A. Thayil, A. Jesacher, K. Grieve, D. Debarre, T. Wilson, M. Booth, and S. Srinivas, “Characterisation of the dynamic behaviour of lipid droplets in the early mouse embryo using adaptive harmonic generation microscopy,” *BMC Cell Biology*, vol. 11, no. 1, p. 38, Jun. 2010.

[109] S.-Y. Chen, H.-Y. Wu, and C.-K. Sun, “In vivo harmonic generation biopsy of human skin,” *J. Biomed. Opt*, vol. 14, no. 6, pp. 060505–060505–3, 2009.

[110] N.Prent, “Investigating Mitochondrial activity during muscle contractions with harmonic generation microscopy”

[111] V. Barzda, C. Greenhalgh, J. Aus der Au, S. Elmore, J. H. van Beek, and J. Squier, “Visualization of mitochondria in cardiomyocytes by simultaneous harmonic generation and fluorescence microscopy,” *Optics Express*, vol. 13, no. 20, p. 8263, 2005.

[112] D. Oron, E. Tal, and Y. Silberberg, “Depth-resolved multiphoton polarization microscopy by third-harmonic generation,” *Opt. Lett.*, vol. 28, no. 23, pp. 2315–2317, 2003.

[113] G. Bottger, B. Nagelkerken, and P. van der Sluijs, “Rab4 and Rab7 Define Distinct Nonoverlapping Endosomal Compartments,” *J. Biol. Chem.*, vol. 271, no. 46, pp. 29191–29197, Nov. 1996.

[114] C. Bucci, P. Thomsen, P. Nicoziani, J. McCarthy, and B. van Deurs, “Rab7: a key to lysosome biogenesis,” *Mol. Biol. Cell*, vol. 11, no. 2, pp. 467–480, Feb. 2000.

[115] J. Gruenberg, “The endocytic pathway: a mosaic of domains,” *Nat Rev Mol Cell Biol*, vol. 2, no. 10, pp. 721–730, 2001.

[116] R. C. Piper and D. J. Katzmann, “Biogenesis and Function of Multivesicular Bodies,” *Annu Rev Cell Dev Biol*, vol. 23, pp. 519–547, 2007.

[117] J. Gruenberg and H. Stenmark, “Opinion: The biogenesis of multivesicular endosomes,” *Nature Reviews Molecular Cell Biology*, vol. 5, no. 4, pp. 317–323, Apr. 2004.

[118] ‘Fluorescence SpectraViewer’.